Rheological Studies on Liquid Crystals with Structural and Induced Topological Defects

A Thesis submitted for the award of the
degree of

Doctor of Philosophy in Physics

by

Rasmita Sahoo

12PHPH19

Supervisor: Prof. Surajit Dhara

School of Physics
University of Hyderabad
Hyderabad, India
April 2017

TO

My Family

Declaration

I, **Rasmita Sahoo**, hereby declare that this thesis entitled **"Rheological Studies on Liquid Crystals with Structural and Induced Topological Defects"** submitted by me under the supervision of **Prof. Surajit Dhara**, School of Physics, University of Hyderabad, Hyderabad, India is a bonafide research work and also free from plagiarism. I hereby declare that it has not been submitted previously in part or in full to this University or any other University or Institution for the award of any degree or diploma.

Rasmita Sahoo
Reg. No: 12PHPH19

Date:
Place: Hyderabad

Certificate

This is to certify that the thesis entitled **"Rheological Studies on Liquid Crystals with Structural and Induced Topological Defects"** bearing Reg. No. 12PHPH19 in fulfilment of the requirements for the award of Doctor of Philosophy in Physics is a bonafide work carried out by her under my supervision and guidance.

This thesis is free from plagiarism and has not been submitted previously in part or in full to this University or any other University or Institution for the award of any degree or diploma. Further, the student has the following publications before the submission of the thesis for adjudication.

1. Rasmita Sahoo, J. Ananthaiah, R. Dabrowski, and Surajit Dhara, *Physical Review E* **90**, 012506 (2014). Chapter-3.
2. Rasmita Sahoo, M. V. Rasna, D. Lisjak, A. Mertelj and Surajit Dhara, *Applied Physics Letters* **106**, 161905 (2015). Chapter-4.
3. Rasmita Sahoo, O. Chojnowska, R. Dabrowski and Surajit Dhara, *Soft Matter* **12**, 1324 (2016). Chapter-5.
4. Rasmita Sahoo and Surajit Dhara, *Liquid Crystals*, DOI:10.1080/02678292.2017.1309469. Chapter-6

Further, the student has passed the following course towards the fulfilment of coursework required for Ph.D.

SN	**Course Code**	**Name**	**Credits**	**Pass/Fail**
1)	PY801	Advanced Quantum Mechanics	4	Pass
2)	PY803	Advanced Statistical Mechanics	4	Pass
3)	PY804	Advanced Electromagnetic Theory	4	Pass
4)	PY821	Research Methodology	4	Pass

Prof. Surajit Dhara
Thesis Supervisor
School Of Physics
University of Hyderabad

Dean
School Of Physics
University of Hyderabad

Acknowledgement

It's my pleasure to express my sincere gratitude to the people who supported me during the course of my doctoral thesis.

Firstly, my deep gratitude goes to my thesis advisor, Prof. Surajit Dhara, for his enduring guidance. His insistence on excellency, discipline and sincerity always influenced me towards new research ideas. His care, motivation and kindness will be remembered forever.

I would like to thank my Doctoral committee members: Prof. V. S. S. Sastry, Prof. S. Srinath and Dr. G. Venkataiah for their illuminating discussions and suggestions throughout my research work. I am also thankful to the collaborators Prof. A. Mertelj and Prof. R. Dabrowski for providing the samples from time to time.

Further, I am grateful to the former Deans, Prof. S. Tiwari, Prof. S. Chaturvedi, Prof. R. Singh and present Dean Prof. Bindu A. Bambah for providing me all the school level facilities and also all the other faculty members of School of Physics for their valuable suggestions at appropriate times. I am thankful to T. Abraham, Shailaja, Sridhar, Prasad, Dipika and all other non-teaching staffs for their help and support in the department. In addition I thank UOH administrative sections especially Mr. Sudhir and Mr. Kashyap for their kind cooperation in dealing with official works, whenever the need arose. I thank to University of Hyderabad and UGC-BSR for their financial assistance during my Ph.D. course. Overall I express my heartiest thanks to School of Physics, University of Hyderabad for giving me the opportunity to accomplish my Ph.D. successfully.

I am very much thankful to my senior Dr. J. Ananthaiah in helping me to learn all the rheometry techniques. My earnest gratitude to all other seniors Dr. T. Arun Kumar, Dr. P. Sathyanarayan, Dr. D. Venkata Sai, and Ramesh Manda for their help and support during my research work. My earnest thanks to Mr. K.P Zuhail, for his fruitful discussions and suggestions. I wish all the best to the juniors Junaid Ahmad, Muhammed Rasi, Subhransu, Praveen and Dinesh. I really enjoyed their company. It was very nice to work with them. My sincere thanks to a special lady Rasna, a real friend. Being a lab-mate and room-mate, she has guided me in each and every step of my stay with her. I could not have imagined to stay in the hostel for such a long time without her company. I would like to extend my warm thanks to my all other friends and classmates.

My heartiest thanks to Priyabrat, Ritika, Ritu, Dr. Ajeet Kumar and many others who have helped during my hard times in the University.

Undoubtedly, I am indebted to my family for their unconditional love and support without whom reaching to this height would not have been possible. I am very much grateful to my parents for giving freedom and helping me to fulfil my all desires in each and every step of my life. I feel blessed to have my brothers Deepak and Alok, who have always believed in me and encouraged to go on any adventure. I express my heartfelt thanks to my husband, Dr. Bibhuprasad, who has been my inspiration through out my Ph.D. I am very much thankful to my in-laws, for their continuous love and care. A sincere thanks to my brother-in-law, Debaprasad for his all-time support. I am thankful to my all other relatives and family members for their love.

Beyond everything, I am highly grateful to God, the omnipresent, for blessing me in all the way through out my life.

Preface

Liquid crystals (LCs) are the materials whose physical properties are intermediate between those of ordered solids like crystals and the isotropic liquids. The molecules in the liquid crystalline state exhibit long-range orientational order and a few of them also show positional order. Thus the LC phase exhibits the symmetries in-between the liquids and the crystals. They exhibit liquid-like properties such as fluidity, viscosity and surface tension. At the same time they also exhibit solid-like properties namely, optical birefringence, anisotropies of refractive indices, dielectric and diamagnetic susceptibilities. Liquid crystals are mainly divided into two categories namely, thermotropic and lyotropic. In thermotropic LCs, the mesophases arise due to temperature whereas in the lyotropic LCs, mesophases arise due to the concentration of the solute as well as the temperature.

Rheology is a multidisciplinary branch of science which deals with the study of deformation and flow of matters. There are many ideal viscous liquids and ideal elastic solids whose flow behavior can be explained by the classical extremes of Hooke's law and Newton's law respectively. They are called as Hookean elastic solids and Newtonian viscous liquids. Apart from this ideal elastic behavior, there are many complex fluids especially soft materials, which exhibit both the properties. Rheological properties of those soft materials like bio-fluids, foods, polymer-melts, cosmetics, paints, liquid crystals etc, are interesting both from the fundamental and application point of view.

In general, liquid crystals show long-range orientational order, but there are few LCs, where chiral interactions dominate over the elastic forces to produce different complex structures. When the chiral strength is increased, some compounds show complex structures where topological defects stabilize the system. These are also called the frustrated structures of liquid crystals. In this thesis, we study the rheological properties and the microstructures of some complex phases of liquid crystals like Twist grain boundary-A (TGB_A) and Blue phases (BP). The TGB_A is the intermediate phase between the cholesteric and the smectic-A phase, where the twist penetrates into a smectic-A structure via a lattice of screw dislocations and the linear array of parallel screw dislocations form grain boundaries. So the defects are in-built to the structure. Similarly in the blue phase, due to the increase in chirality in the system, the orientation of the local director twists around two perpendicular axes and the corresponding structures give rise to different phases like BP-I, BP-II and BP-III, where BP-III is an amorphous one. So in both TGB_A and blue phases, the defects are inherent to the structures and those defects can be named as intrinsic or structural defects. These topological defects can also be created by dispersing foreign particles into the liquid crystals and called as extrinsic or induced defects. The present thesis aims at understanding the rheological properties of the LCs with both structural and induced topological defects. This thesis is organized into six chapters which are described as following.

The **first chapter** is an introductory chapter which gives a brief discussion about different phases and physical properties of liquid crystals, LC-colloids and different rheological properties which are relevant to our studies.

The **second chapter** consists of all the experimental techniques used in this thesis. For rheological studies, we used normal rheology, electro-rheology, rheo-microscopy, rheo-sals (small angle light scattering) and magneto-rheology techniques. All the rheological measurements are done using a stress controlled rheometer (Anton Paar MCR 501) with cone plate or parallel plate measuring systems. To understand the rheological results we measured some physical properties of liquid crystals like dielectric anisotropy ($\Delta\epsilon$), splay (K_{11}), bend (K_{33}) elastic constants and rotational viscosity (γ_1). In this case we set up an electro-optic technique.

In **third chapter** we study the rheological properties of Twist Grain Boundary-A (TGB_A) phase which consists of a twisted arrangement of blocks of layered type SmA liquid crystals, separated by twist grain boundaries, which are made of an array of screw dislocations. The interacting dislocations form the grain boundary and the interaction among the grain boundaries stabilizes the TGB_A structure. So in this phase defects are intrinsic to the structure and our main goal is to understand the mechanical properties of this phase. Usually the temperature range of TGB_A phase is short ($1-2$°C) in pure compounds. To get a broader temperature range of TGB_A

phase, we have chosen a binary mixture of two compounds namely, 4-(2'-methyl butyl phenyl 4'-n-octylbiphenyl-4-carboxylate (CE8) and 2-cyano-4-heptyl-phenyl-4'-pentyl-4-biphenyl carboxylate [7(CN)5]. CE8 is a chiral and 7(CN)5 is a nonchiral compound . This binary mixture was prepared by taking 63.6 wt% of CE8 and 36.4 wt% of 7(CN)5 and a larger temperature range (18^oC) of the TGB_A phase is obtained. This mixture exhibits three different phases i.e cholesteric (N^*), TGB_A, and SmC^*. We have analysed the elasticity of the TGB_A phase, based on the theory in lamellar systems that accounts for the contribution of defects. The power-law dependence of the complex shear modulus and the analysis of the experimental results suggest that the elasticity of the TGB_A phase is due to the screw dislocations and the grain boundaries.

In **fourth chapter** we study on another interesting complex phase i.e Blue phase. In highly chiral systems, close to the isotopic transition, the orientation of the local director can twist around two perpendicular axes and the corresponding deformed structure is termed as 'double twist cylinder'. Blue phases are the special cases in which double twist cylinders fill up the volume by stabilizing a lattice of defect-disclinations. Depending on the arrangement of the defect lines they are classified into three types namely, BP-I (body-centered cubic structure), BP-II (simple cubic) and BP-III (amorphous). The symmetry of BP-III is same as that of the isotropic phase and shows amorphous structure. In BP-II case the disclination lines intersect to form a simple cubic structure and form a characteristic network. In the BP-I case, the disclination lines are separated and don't intersect, hence form a body centred cubic symmetry. Blue phases are stable only over a short temperature range ($\sim 1K$). Hence to get a large temperature range, we have chosen a multicomponent mixture in our experiment. The mixture consists of four fluorinated compounds and a highly chiral dopant which shows phase transitions of BP-II, BP-I and cholesteric phase respectively. Recently some theoretical predictions have been made on the rheological properties and the dynamics of the disclination networks of BP-I and BP-II, however experimentally very little is explored. We performed rheomicroscopy and small angle light scattering experiments to understand the microstructures and the dynamics of defects under shear. Some features of our experimental results are discussed based on the recent theoretical predictions.

In the **fifth chapter** we study the magnetoviscosity and magnetodielectric properties of ferromagnetic nematic LC. We prepared the ferronematic sample by dispersing ferromagnetic nanoparticles i.e scandium-doped barium hexaferrite single-crystal ($BaFe_{11.5}Sc_{0.5}O_{19}$) in a thermotropic liquid crystal 4-cyano-4'-octylbiphenyl (8CB). We measured splay and bend elastic constant (K_{11} and K_{33}) and rotational viscosity (γ_1). Both the splay elastic constant (K_{11}) and rotational viscosity (γ_1) were substantially lower than that of the pure LC. There was no distinguishable change observed in the case of bend elastic constant (K_{33}). In the ferromagnetic LC, the viscosity exhibits three distinct regimes. In the very low field region (up to ≃15 mT), η_{eff} ($\simeq \eta_2$) is almost constant and increases rapidly in the intermediate field range (15 mT to 22 mT). At relatively higher field, η_{eff} saturates and exhibits hysteresis while the field is reduced to zero. This is due to the orientational coupling between the director field and the magnetization. The small amount of magnetic nanoparticles (e.g. 0.3 wt.%) do not change the Miesowicz viscosities but facilitate the measurements at a significantly low magnetic field. thus this method may be used to measure the two Miesowicz viscosities at very small magnetic field.

In the **sixth chapter** we study the rheological properties of nematic and smectic-A liquid crystal colloids, where our main goal is to investigate the rheological properties of LC colloids along with rheo-microscopy to understand the effect of defects. The nematic and SmA colloids were prepared by dispersing 5μm spherical microspheres in 8CB liquid crystals. The microparticles induce quadrupolar defects in the nematic phase and create colloidal chains and the chains form network structures. We found the apparent yield stress in the nematic phase increases with increasing volume fraction of particles (ϕ) due to the network structure of the colloidal chains. The rheomicroscopy studies reveal the shear-rate dependent distinct dynamics of those colloidal chains. We observed a shear thickening behaviour of the effective shear viscosity in the nematic phase. The critical strain amplitude (γ_c i.e., crossover of (G' and G'') in SmA-colloids decreases significantly with increasing ϕ. The variation of storage modulus with ϕ indicates that the SmA-colloids response is dominated by defects.

Contents

List of Abbreviations and Symbols

MCR : Modular compact rheometer

CP : Cone and plate

PP : Parallel-plate

CC : Co-axial cylinder

SALS : Small angle light scattering

MRD : Magneto-rheological device

σ : Shear stress

σ_y : Apparent yield stress

γ : Shear strain

$\dot{\gamma}$: Shear rate

G : Shear modulus

$G_\circ$: Plateau modulus

η : Shear viscosity

σ_{eff} : Effective shear viscosity

G^* : Complex modulus

G' : Storage modulus

G'' : Loss modulus

ω : Angular frequency

D_e : Deborah number

E_r : Ericksen number

q : Scattering vector

λ : Wavelength

θ : Scattering angle

I : Intensity

N : Nematic Phase

SmA : Smectic-A phase

SmC : Smectic-C phase

N^* : Cholesteric phase

TGB : Twist grain boundary phase

$UTGB_{C^*}$: Undulated twist grain boundary in smectic-C^* phase
BP : Blue phase
$\hat{n}$: Liquid Crystal Director
ψ : Smectic order parameter
B : Layer compression modulus
$T_{N^*-TGB_A}$: Cholesteric - TGB_A phase transition temperature
ITO : Indium tin oxide
OPM : Optical polarising microscope
$\vec{D}$: Electric displacement vector
$\epsilon_{||}$: Dielectric constant parallel to $\hat{n}$
$\epsilon_{\perp}$: Dielectric constant perpendicular to $\hat{n}$
$\Delta\epsilon=\epsilon_{||} - \epsilon_{\perp}$: Dielectric anisotropy
V_{th} : Freedericksz threshold voltage
V_b : Bias voltage
K_{11}, K_{22}, K_{33} : Splay, twist and bend elastic constant
γ_1 : Rotational viscosity
$\tau_{\circ}$: Relaxation time
η_1, η_2, η_3 : Miesowicz viscosity coefficients
$\alpha_1......\alpha_6$: Leslie coefficients
x : Effective noise temperature
$\vec{b}$: Burger's vector
r_c : Defect core radius

1

Introduction

1.1 Rheology

Rheology is an interdisciplinary branch of natural sciences which deals with the study of deformation and flow of matter under applied forces, mainly in liquids but also in soft solids or solids under suitable conditions. It is a multidisciplinary science which deals with many scientific branches like polymer, biology, pharmaceutical and food industries etc. Rheometry is the group of experimental techniques to explore about the rheological properties of materials. The rheological properties are probed by measuring the rheological parameters like viscosity and elasticity depending upon the external applied conditions, such as shear rate, stress, strain, time-scale and temperature. Apart from the external factors, the internal sample variations like concentration and stability are also the key features that control the rheological properties.

There are many complex materials which do not follow Newton-Stokes and Hooke laws, but are very interesting from the theory and application points of view. In case of these fluids the shear stress does not vary in the same proportion with shear rate, so the viscosity of such fluids changes with respect to shear rate, called "*apparent viscosity*". However, there are some fluids which show decreasing viscosity with increasing shear rate and the behavior is called as "*shear thinning*". The examples of such kind of fluids are paints, emulsions and dispersions. There are also some kind of complex fluids which show increasing viscosity with increasing shear rate, called dilatant fluids and the behavior is called as "*shear thickening*". There are also certain complex fluids which show a change in viscosity with time at a constant shear rate, called as "*thixotropy*". Most of these complex materials can be characterised by the dimensionless numbers, such as Deborah number (D_e), Weissenberg number (W_i), Peclet number (P_e) and Ericksen number (E_r) [1, 2]. We discuss Deborah and Ericksen number as they are relevant to the present thesis. Deborah number is defined as

$$D_e = \tau/T \quad or \quad D_e = \omega\tau \tag{1.1}$$

where τ is the characteristic relaxation time of the material and T is a characteristic time of the deformation process being observed. In an oscillatory shear flow, if $D_e \equiv \omega\tau \gg 1$, the material behaves as solid-like and when $D_e \ll 1$, shows a liquid-like terminal behavior. Hence The characteristic time τ is infinite for Hookean elastic solids and it is zero for a Newtonian viscous liquids. The Ericksen number for liquid crystals is defined as

$$E_r \equiv \frac{\eta\,\dot{\gamma}_{eff}}{K/h^2} \tag{1.2}$$

where η is the typical Leslie viscosity, K is a Frank constant, $\dot{\gamma}_{eff}$ is the average shear rate and h is the length scale of the flow geometry. So it is the ratio of flow-induced viscous stress to the Frank elastic stress. In liquid crystals the Ericksen number varies over a large range (1-10^6). For liquid crystals with small-molecule such as PAA or MBBA, the Ericksen number is in the range of 10^6. E_r also depends on the particular flow geometry as η and K vary with respect to it.

1.2 Rheology of liquid crystals

Liquid crystals are typical representative of soft materials and very responsive to relatively weak perturbation. As the name suggests LCs have some of the ordering properties like solids and also can flow like liquids. They exhibit unusual rheological properties due to the competition between elastic forces provided by the LC molecules and the tangential shear produced on them to align in the flow direction. In liquid crystals topological defects are generated during the symmetry breaking phase transition from the isotropic to the liquid crystalline phases. Those defects have significant effect on the rheological properties of the LC materials. Hence apart from the flow properties it is very important to understand the dynamics of those defects under shear. In this thesis we study rheological properties of some exotic chiral phases of liquid crystals where the defects are intrinsic (structural) and also the systems where the defects are created by introducing foreign particles. These defects can be called as extrinsic (induced) topological defects.

1.3 Liquid crystals

Liquid crystals (LCs) are the states of matter, which exists between the three dimensionally ordered solid crystals and the isotropic liquids. These partially ordered, anisotropic fluids were first discovered by an Austrian botanist Friedricz Reinitzer in 1888. The molecules in this state exhibit long range orientational order, in addition with one or two dimensional positional order. Liquid crystals exhibit both liquid-like as well as solid-like properties. They have liquid-like properties like viscosity, surface tension etc. At the same time they also exhibit solid-like properties, like anisotropy in optical (birefringence), electrical (dielectric), and magnetic properties (diamagnetic susceptibility) etc [3,4]. They show elastic properties and can transmit torques. Most of their physical properties are highly anisotropic and due to these special characteristics, they are very useful in making low power consuming displays and tunable optical devices. Liquid crystals can be widely categorized into two groups namely thermotropic and lyotropic. Thermotropic liquid crystals are basically temperature dependent whereas lyotropic liquid crystals are both temperature and concentration dependent. There are some compounds which exhibit both lyotropic and thermotropic phases, these are called as amphotropic [5].

Thermotropic liquid crystals are further classified into three categories depending upon the shape of the constituent molecules. They are known as (i) calamatic (consists of rod-like molecules), (ii) discotic (consists of disc-like molecules and) and (iii) bent-core (consists of bent-shaped molecules). The calamatic liquid crystals exhibit various phases. Some of the phases are discussed here which are relevant to the present thesis.

1.3.1 Nematic phase

Nematic (N) phase is the simplest phase which has least order and the highest symmetry. It shows only orientational order of the long molecular axes. The average alignment direction of the long molecular axes is called the director ($\hat{n}$). The center of mass of the molecules are randomly distributed in three dimensions. The director $\hat{n}$ is apolar in nature, i.e., $\hat{n}$ and -$\hat{n}$ are physically identical. In the nematic phase usually the rotational symmetry exists along the director, hence they are uniaxial in nature. A schematic diagram of the nematic phase is shown in Fig. 1.1.

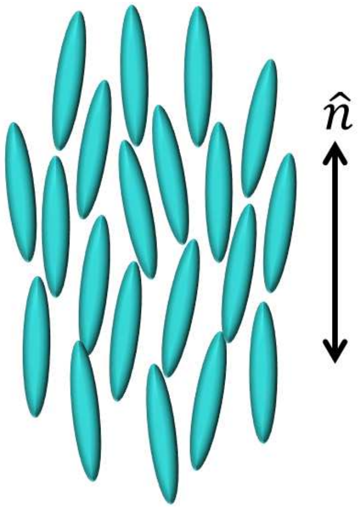

Figure 1.1: Schematic representation of nematic phase, $\hat{n}$ signifies the director of the rod-shaped molecules.

1.3.2 Cholesteric phase

The chiral nematic phase is known as cholesteric (N^*) phase. If the chiral dopants are added to the nematic phase, or the molecules are inherently chiral, it causes a twist or a helix in the nematic structure. Locally the cholecteric phase is very close to the nematic phase, but due to the chirality of molecules, the director $\hat{n}$ rotates in a helical manner. So it gives rise to a chiral pitch p, where the liquid crystal molecules rotate through an angle of 360^o. The director rotates 0^o-180^o as $\hat{n}$ and then 180^o-360^o as $-\hat{n}$, which are equivalent. So the pitch p repeats through a distance $p/2$. The pitch

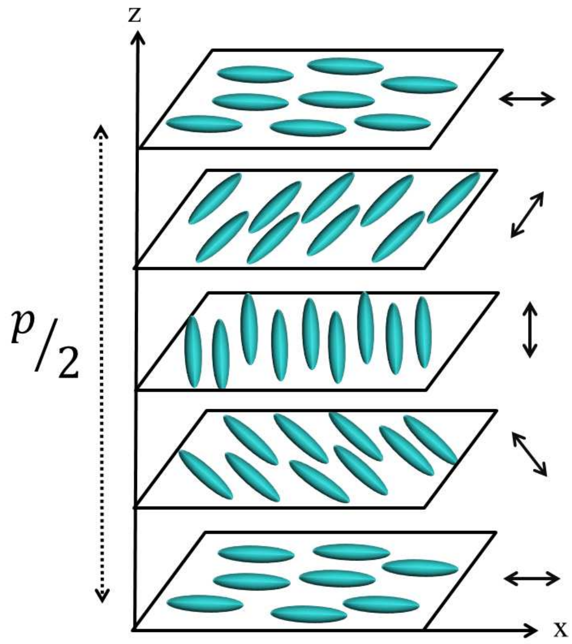

Figure 1.2: Schematic representation of the molecular arrangement in the cholesteric phase. $p/2$ indicates the half pitch.

changes when the temperature is altered or if the other molecules are added into it. The schematic diagram of the N^* phase is presented in the Fig. 1.2.

1.3.3 Smectic phases

In the smectic phases apart from orientational order, the molecules also have an additional positional order. This positional order may be one dimensional, directing to the layered type structures namely SmA and SmC phases. Though the molecules are arranged in the layers, their centres of mass are randomly distributed like liquids.

1.3.3.1 Smectic-A

In the smectic-A (SmA) phase the molecules are arranged in the layers, where the director $\hat{n}$ is aligned parallel to the smectic layer normal $\hat{z}$ as shown in the Fig. 1.3.

The layer spacing in the smectic-A phase is usually comparable with the molecular length. The molecules can rotate freely in the layers. There is no long range correlation of the center of mass of the molecules in the smectic layers. Hence the layers can slide over each other and also the diffusion of molecules from one layer to other is possible. The SmA phase is usually uniaxial and positive.

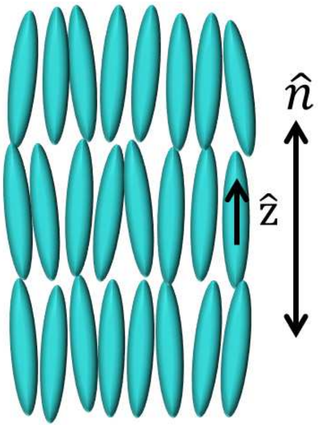

Figure 1.3: Schematic representation of a SmA phase. The director $\hat{n}$ is oriented parallel to the smectic layer layer normal $\hat{z}$.

1.3.3.2 Smectic-C

The smectic-C (SmC) phase looks almost similar to the smectic-A phase due to its one dimensional positional order. The only difference is that the director is tilted by

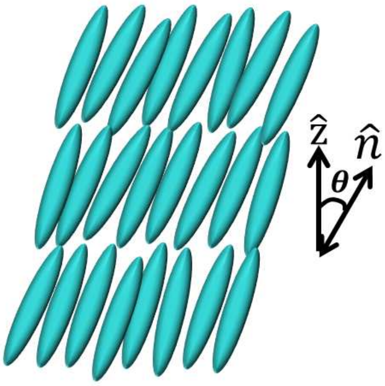

Figure 1.4: Schematic representation of a SmC phase. The director $\hat{n}$ is tilted with respect to the smectic layer normal $\hat{z}$ by an angle θ.

an angle with respect to the smectic layer normal ($\hat{z}$), as shown in the Fig. 1.4. The tilt of the director can be defined as an angle θ and the layer thickness is dependant on θ. The centres of mass of the molecules are randomly oriented in the SmC layers.

1.3.3.3 Smectic-C*

In the smectic-C phase, if the molecules are chiral, then the chiral interactions develop a spontaneous helical structure, called as smectic-C^* (SmC^*) phase. A schematic diagram of this phase is shown in the Fig. 1.5. In this phase the helical axis is parallel to the layer normal. The arbitrary local director $\hat{n}$ can be defined as:

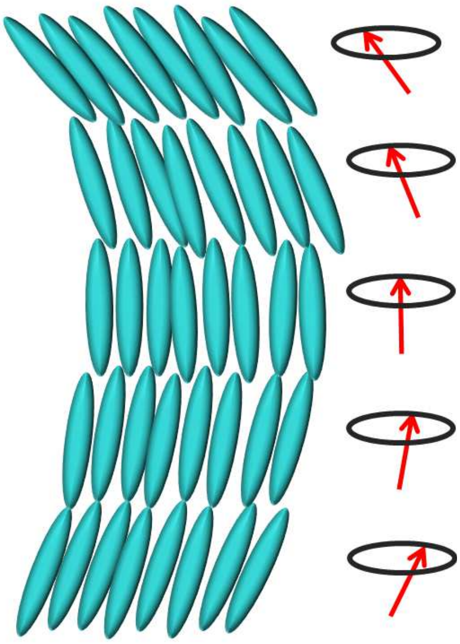

Figure 1.5: Schematic representation of a SmC^* phase where the tilt direction rotates on passing from one layer to another in a helical manner.

$$\hat{n} \equiv (sin\theta cos\phi,\ sin\theta sin\phi,\ cos\theta) \tag{1.3}$$

where θ is the tilt angle and ϕ is the azimuthal angle. The tilt angle θ remains same, but ϕ varies, from one layer to another along the z direction.

1.4 Defect induced phases in liquid crystals

1.4.1 Twist Grain Boundary phases

Twist grain boundary (TGB) phases are the frustrated phases of liquid crystals located in between cholesteric and smectic phases. In some smectics, when the molecular chirality increases, then the competition between twist formation and smectic layer formation leads to a defect stabilized structure, named as TGB phase. This thermodynamically stable phase was first experimentally observed by Goodby *et al.* [6] and the detailed structure was predicted by Renn and Lubensky [7]. This phase is analogous to the Abrikosov phase of type-II superconductors in an external magnetic field [3, 7]. In this analogy the twist of a cholesteric phase penetrating the SmA structure through a lattice of screw dislocations which is similar to the magnetic flux lines penetrating a type-II superconductor via lattice of vortices. A schematic diagram showing the analogy between TGB_A and the Abrikosov phase is shown in Fig. 1.6. Here the cholesteric phase corresponds to the normal metal in a magnetic field. SmA phase corresponds to Meissner phase. Chirality field corresponds to magnetic field. The screw dislocations and TGB phase correspond to magnetic vortex and Abrikosov phase respectively. A schematic representation of the arrangement of smectic-A blocks of TGB_A phase is shown in Fig. 1.7. A typical distance between two dislocations (l_d) in a grain boundary and the inter grain boundary distance (l_b) is in the range of $l_d \sim l_b \sim 20$ to 30 nm [8]. The smectic-A blocks with these dislocations form a helical structure. In

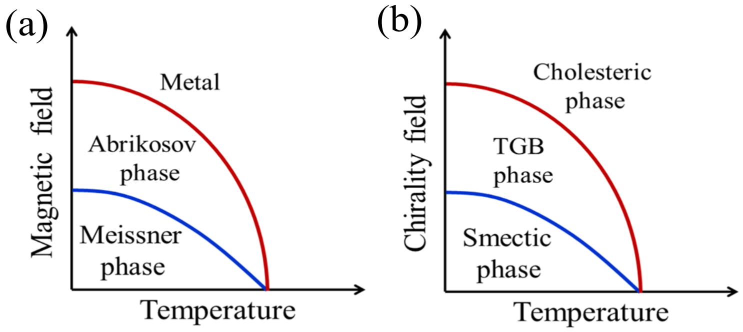

Figure 1.6: Schematic representation showing the analogy between TGB_A and Abrikosov phase.

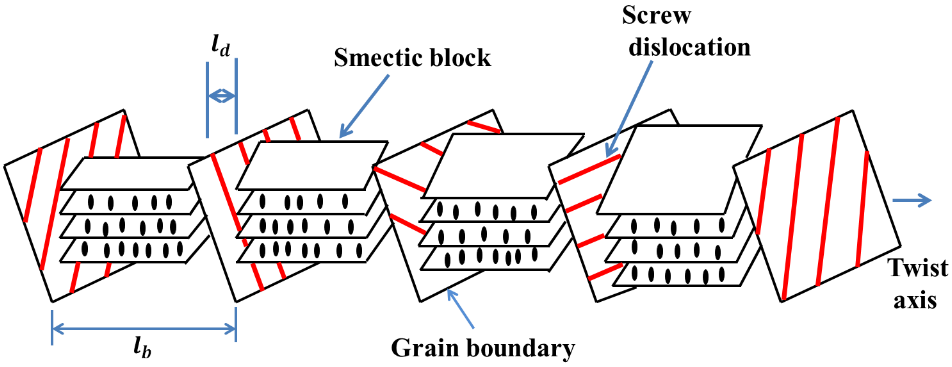

Figure 1.7: Schematic diagram showing the structure of the TGB_A phase. The distance between two dislocations and two grain boundaries are l_d and l_b respectively.

this phase, well-defined SmA blocks are separated by regularly spaced planar arrays of parallel screw dislocations (Fig. 1.7). These parallel screw dislocations arise due to the rotation of successive smectic slabs relative to each other. This results a twist deformation in the Frank-director.

1.4.2 Undulated Twist Grain Boundary-C* phase

Undulated twist grain boundary-C* ($UTGB_{C^*}$) phase is a three dimensionally modulated chiral SmC phase [9,10], which has a two-dimensional (2D) undulation of SmC^*

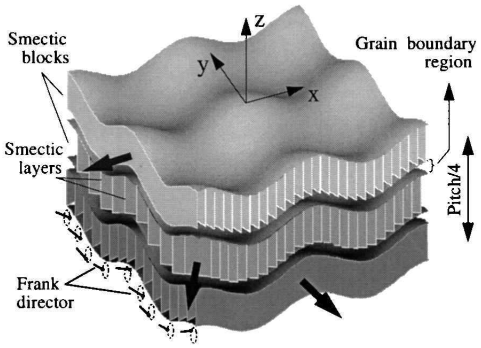

Figure 1.8: The schematic representation of $UTGB_{C^*}$. Adapted from ref. [10].

blocks in the form of a square lattice. A schematic diagram of this phase is shown in the Fig. 1.8. In this phase the grain boundaries have two-dimensional undulation along the directions which are perpendicular to the *TGB* twist axis. Apart from these configuration, within the smectic layers, the director has a helical arrangement. In this phase the two dimensional undulation of *SmC* blocks, leads to a square grid pattern.

1.4.3 Blue phases

Blue phases (*BP*) are the frustrated phases observed in highly chiral systems. It appears close to the isotropic-cholesteric or isotropic-smectic phase transition, where the orientation of the local director can twist around two perpendicular axes and the corresponding deformed structure is termed as a "double-twist cylinder" [3]. A schematic diagram of BP-II and BP-I are shown in Fig. 1.9. Blue phases are special cases in which double twist cylinders fill up the volume by stabilizing a lattice of defect-disclinations [11, 12]. Depending on the arrangement of the defect lines they are classified into three types namely, BP-I (body-centered cubic structure), BP-II (simple cubic) and BP-III (amorphous). The BP-III phase is amorphous, and its symmetry is almost similar to the isotropic phase, so it is quite difficult to detect under polarized microscope. The stability of BP-I increases with increasing chirality

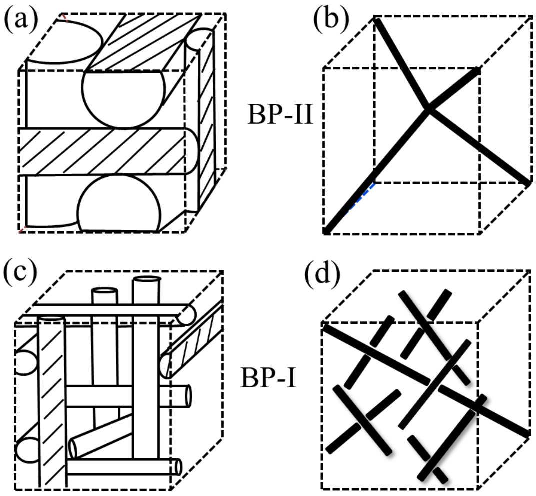

Figure 1.9: Schematic diagrams of the BP-II and BP-I. (a) and (c) Spatial arrangements of double twisted cylinders in unit cells. (b) Simple cubic unit cell of the disinclination lattice in BP-II. (d) Body centered cubic unit cell of the disinclination lattice in BP-I. The black lines in (b) and (d) are the defect-disinclinations.

while BP-II exists upto a certain range of the temperature-chirality variation. In the BP-II case, the disclination lines intersect to each other whereas in the BP-I case, they don't intersect to each other. In pure compounds these phases are observed within a very short range of temperature ($\sim$ 1K).

1.5 Physical properties of liquid crystals

In this section we discuss some physical properties of the liquid crystals which are relevant to our studies.

1.5.1 Dielectric constant

The dielectric properties of the liquid crystals are related to the response of the LC molecules to an applied electric field. The dielectric constant depends on the molecular charge distribution and the intermolecular interactions. In liquid crystals, consisting of non-polar molecules, the dielectric constant arises due to the induced polarisation and it has two parts i.e electronic polarization and ionic polarization. In liquid crystals, consisting of polar molecules, the dielectric constant arises not only due to the induced dipole moments, but also due to the permanent dipole moments, which has the tendency to orient themselves parallel to the external applied field. The dielectric constant of the material depends on the temperature and also the frequency of the applied electric field. In liquid crystals, two components of the dielectric constant ($\epsilon_{\perp}$ and $\epsilon_{||}$) can be measured depending on the direction of applied electric field with respect to the LC director. The applied electric field, perpendicular to the LC director, gives $\epsilon_{\perp}$ and parallel to the director gives $\epsilon_{||}$. The dielectric anisotropy is defined as:

$$\Delta\epsilon = \epsilon_{||} - \epsilon_{\perp} \tag{1.4}$$

1.5.2 Curvature elastic constants

Nematic liquid crystals are orientationally ordered fluids and can be deformed easily with the application of external force. When a director distortion is induced, the derivatives of $\vec{n}$(r) arises, which leads to an elastic restoring torque tending to restore $\vec{n}$(r) to the undisturbed state. The elastic deformation can be expressed as the combination of three basic curvature deformations, known as splay, twist and bend. A schematic diagram of these elastic distortions are presented in the Fig. 1.10. The deformation free energy density is defined as [3, 4, 13]:

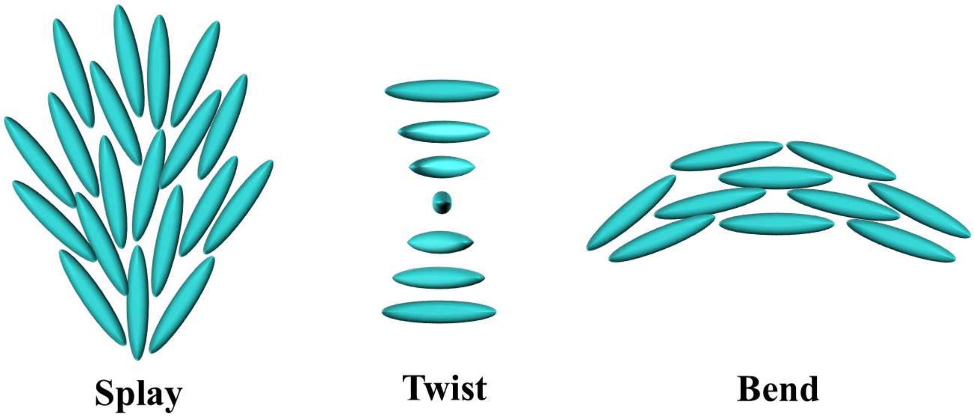

Figure 1.10: Schematic representation of splay, twist and bend distortion of LC director.

$$F_N = \frac{1}{2}[K_{11}(\nabla.\hat{n})^2 + K_{22}(\hat{n}.\nabla\times\hat{n})^2 + K_{33}(\hat{n}\times\nabla\times\hat{n})^2] \tag{1.5}$$

where K_{11}, K_{22} and K_{33} are splay, twist and bend elastic constants, respectively. Usually in rod-like molecules, $K_{33} > K_{11} > K_{22}$ and these elastic constants are positive. The typical magnitude of those constants are $\simeq 10^{-12}$N.

1.5.3 Rotational viscosity

Rotational viscosity (γ_1) is one of the most important physical properties of liquid crystals. This parameter determines the elecro-optical switching speed. When an external field is applied to the liquid crystals, the molecules can rotate around an axes perpendicular to the director, resulting the rotational viscosity (γ_1). The magnitude of γ_1 depends on the structure of the molecules, inter-molecular interactions, and temperature. For nematics, γ_1 is defined as [14, 15]:

$$\gamma_1 = \frac{\tau_o K_{11} \pi^2}{d^2} \tag{1.6}$$

where K_{11} is the splay elastic constant, d is the thickness of the NLCs in planar cells and τ_o is the relaxation time.

1.5.4 Alignment of liquid crystals

The director ($\hat{n}$) of liquid crystals normally vary in space in an unaligned LC sample. Thus it is very important to make the LC director aligned, for measuring the physical properties of liquid crystals such as dielectric properties, curvature elastic constants, rotational viscosity etc. Moreover uniform alignment is needed for display applications. The director alignment can be obtained by an appropriate surface boundary conditions (confined between two chemically treated glass substrates). There are basically two different types of alignments used for the physical measurements, namely homogeneous (planar) and homeotropic (perpendicular) [16, 17]. The schematic diagrams of these two different types of alignments are shown in the Fig. 1.11.

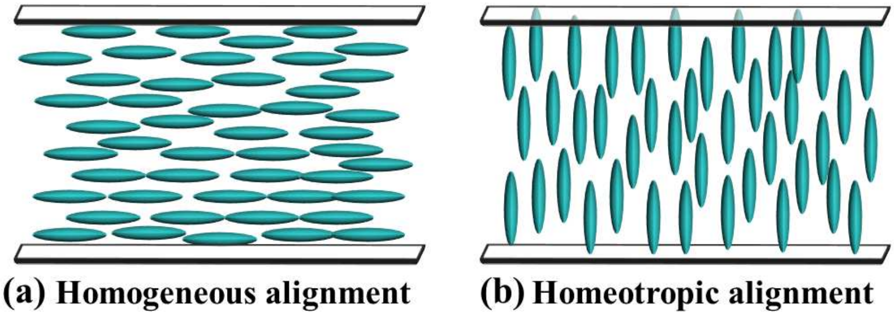

Figure 1.11: Schematic diagrams of the homogeneous and homeotropic alignments.

1.5.4.1 Homogeneous alignment

The homogeneous or planar alignment of the director can be obtained by coating the glass substrates with an appropriate polyimide. The rubbing of the coated glass surface creates micro-grooves along which the LC director can align in parallel to the substrate. For an uniaxial nematic liquid crystal, the optic axis will be along the rubbing direction. The Schematic representation of homogeneous alignment is shown in the Fig 1.11(a).

1.5.4.2 Homeotropic alignment

The homeotropic alignment of the director can be obtained by coating the glass substrates with a suitable polyimide which gives a perpendicular anchoring to the LC molecules. In this case, the molecules have amphiphilic polar groups and aliphatic alkyl chains, where the polar groups stick to the surface and the alkyl chains stand perpendicular to the surface. The interaction between alkyl chains and LC molecules make them align perpendicular to the glass substrate. The schematic diagram of homeotropic alignment is depicted in the Fig 1.11(b).

1.5.5 Freedericksz transition

The transition from an uniformly aligned state of LC to a deformed state by the application of electric or magnetic field is called as Freedericksz transition. The dielectric displacement in a nematic liquid crystal is expressed as [18, 19],

$$\vec{D} = \epsilon_o \epsilon_\perp \vec{E} + \epsilon_o \Delta\epsilon (\hat{n} \cdot \vec{E}) \hat{n} \tag{1.7}$$

and the dielectric energy density of a nematic is defined as,

$$W_{diel} = -\int_0^E \vec{D} \cdot d\vec{E} = -\frac{1}{2}\epsilon_o \epsilon_\perp \vec{E}^2 - \frac{1}{2}\epsilon_o \Delta\epsilon (\hat{n} \cdot \vec{E}^2) \tag{1.8}$$

In the above Eq. 1.8, the dielectric energy can be minimised, when the director ($\hat{n}$) is parallel to the electric field ($\vec{E}$), which depends on the sign of the $\Delta\epsilon$. In a homogeneously aligned nematic LCs, if electric field is applied perpendicular to the director, after a certain field the director reorients along the field direction [20], called as Freedericksz transition. The corresponding voltage is called as Freedericksz threshold voltage and it is given by,

$$V_{th} = \pi \sqrt{\frac{K_{11}}{\epsilon_o \Delta\epsilon}} \tag{1.9}$$

where K_{11} is the splay elastic constant, $\Delta\epsilon$ is the dielectric anisotropy and d is the thickness of the LC cell.

1.6 Rheological properties

In genearl rheological properties reveal the hardness or softness of a material indicating its fluid-like or solid-like behavior. The rheological properties of complex fluids are mesaured through rheometer as a function of rate or frequency of deformation. The storage and loss moduli and the shear viscosity are the important properties to characterise the visco-elastic properties of soft materials. Basically two types of measurements are made to study those properties, namely the oscillatory test and the rotational test.

1.6.1 Storage and loss moduli

The rate of structural rearrangement within a complex fluid can be understood by applying a small-amplitude oscillatory shearing on the material. This kind of deformation can be performed by the oscillatory test in rheometer. The underlying principle of an oscillatory test is to induce a sinusoidal shear deformation in the sample, called as strain and to measure the corresponding storage ($G^{'}$) and loss modulus ($G^{''}$). The time scale is probed by the frequency of oscillation, called as angular frequency (ω) of the shear deformation. In our experiment we use the measuring system, where bottom plate is stationary and the top plate is movable. The top plate provides a time dependent strain (sinusoidal strain) to the complex fluid and it can be defined as:

$$\gamma(t) = \gamma_o\, sin(\omega t) \tag{1.10}$$

where γ_o is the strain amplitude. Hence the time dependent shear stress ($\sigma(t)$) can be determined simultaniously from the measured torque that the sample imposes on the top plate. This time dependent stress response at a constant angular frequency, provides the elastic properties of the materials. If the material is an ideal elastic solid, then the shear stress is proportional to the strain deformation and the proportionality constant is defined as the shear modulus of the material.

$$\sigma(t) = G^{*} \cdot \gamma(t) \tag{1.11}$$

where G^{*} is the complex shear modulus. So for an ideal elastic material the shear stress is always in phase with respect to the applied shear strain. In contrast, if a material is pure viscous fluid, the shear stress is proportional to the shear deformation and the proportionality constant is called as viscosity where the applied shear strain and measured stress are out of phase with a phase angle $\delta = \pi/2$. For a visco-elastic material the shear deformation and stress show both in-phase and out-phase components. So the shear stress is defined as [21]:

$$\sigma(t) = \sigma_o \, sin(\omega t + \delta) \tag{1.12}$$

where σ_o is the shear stress amplitude and δ is the phase lag.

The visco-elastic behavior of the system can be characterised by storage modulus ($G^{'}$) and the loss modulus ($G^{''}$) which signifies solid-like and fluid-like behavior to the measured stress. For a sinusoidal shear deformation, the shear stress response of a visco-elastic material can be defined as:

$$\sigma(t) = G^{'}(\omega) \, \gamma_o \, sin(\omega t) + G^{''}(\omega) \, \gamma_o \, cos(\omega t) \tag{1.13}$$

Here the 1st term consisting of G' is in-phase with the applied strain and represents the storage of elastic energy. The term containing $G^{''}$ is based on out-of phase with the strain and represents viscous dissipation energy.

In general two important measurements are performed under oscillatory test i.e, amplitude sweep and frequency sweep. In the amplitude sweep measurement, the strain dependent $G^{'}$ and $G^{''}$ are measured at a constant angular frequency ω. The region upto which both $G^{'}$ and $G^{''}$ remain constant with applied shear strain, is called as “linear visco-elastic” (LVE) range. Beyond this range both the shear moduli start decreasing and usually shows a crossover, which is called as strain induced yielding or the critical strain (γ_c), above which the fluidization occurs. The storage ($G^{'}$) and loss ($G^{''}$) moduli can be defined as:

$$G^{'} = \frac{\sigma_o}{\gamma_o} \, cos\delta, \quad G^{''} = \frac{\sigma_o}{\gamma_o} \, sin\delta \tag{1.14}$$

The ratio of G''/G' gives $tan\delta$ and is called as the loss tangent. The fluid characteristics can be determined from this $tan\delta$ value. In the oscillatory measurements if $G^{'} > G^{''}$, and $tan\delta$ <<1, then the elastic behavior dominates over the viscous behavior signifying a solid-like response. If $G^{''} > G^{'}$ and $tan\delta$ >>1, then the viscous behavior dominates over the elastic behavior indicating a liquid-like response. The complex modulus G^* can be expressed as:

$$G^* = G^{'} + iG^{''} \tag{1.15}$$

Here G^* signifies the overall shear modulus which resist to the deformation of the complex fluid under applied shear strain.

In the frequency sweep measurement, the angular frequency dependent $G^{'}$ and $G^{''}$ are measured at a constant shear strain. This experiment is performed to study the dynamic behavior of the materials. If $G^{'} \propto \omega^2$ and $G^{''} \propto \omega$, then it shows a Maxwell-fluid like behavior. If $G^{'}$, $G^{''} \propto \omega$, then it shows a soft-glass behavior [22]. At low frequency if $G^{'} > G^{''}$, the material shows a gel-like behavior.

1.6.2 Shear viscosity

Shear viscosity (η) is basically defined as the ratio of shear stress to the shear rate. It is defined as:

$$\eta = \frac{\sigma}{\dot{\gamma}} \tag{1.16}$$

Mainly there are three types of steady state flow behavior observed with respect to shear rate. These are called Newtonian, shear thinning and shear thickening behavior. If the viscosity remains constant with respect to the shear rate, it is called Newtonian flow behavior. If the viscosity decreases with increasing shear rate, then it is called as shear-thinning flow behavior and if the viscosity increases with increasing shear rate, called as shear-thickening flow behavior [2, 21]. Figure 1.12 shows these three different types of flow behavior of fluids. There are different "power-law" models to characterise the flow behaviors of the complex fluids. In the Sisko model the viscosity η is defined as [1]

$$\eta = \eta_\infty + K\dot{\gamma}^{n-1} \tag{1.17}$$

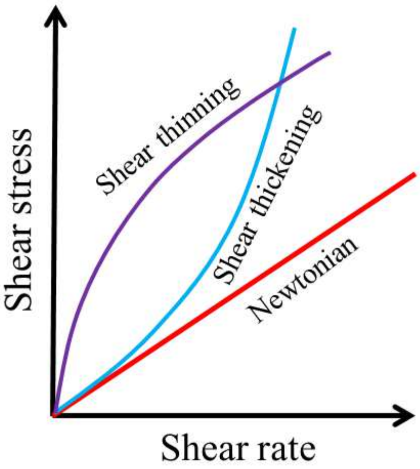

Figure 1.12: The comparison of three different types of flow behavior i.e shear thinning, shear thickening and Newtonian.

where n is called the power-law index, K is called the "consistency", with a unit of Pa. s. According to the Bingham model:

$$\sigma = \sigma_y + \eta_p \dot{\gamma} \tag{1.18}$$

where σ_y is the yield stress and η_p indicates the plastic viscosity. The Bingham equation signifies the yield stress of materials at low shear rate region, whereas Sisko model explains about the viscosity response in the mid to high shear rate range of a flow curve.

1.7 Leslie-Ericksen theory

The viscosity of nematic LC can be explained based on the three fundamental orientations of the director ($\hat{n}$) under shear flow. A schematic diagram of these possible orientations is shown in Fig. 1.13. These three fundamental flow directions of nematic director was first time defined by Miesowicz [23]. These are:

(I) η_1: when $\hat{n}$ is parallel to $\nabla \mathbf{V}$ (velocity gradient direction) (Fig. 1.13),

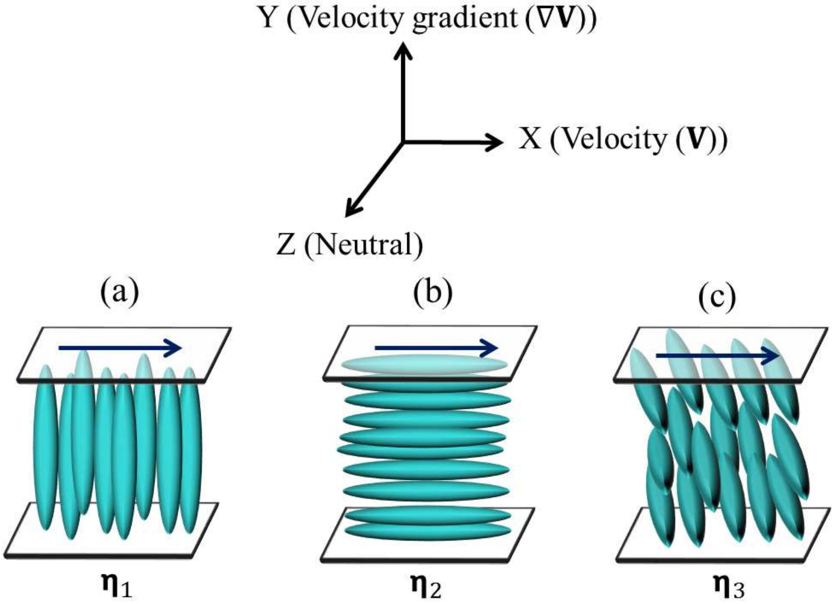

Figure 1.13: Schematic representation of the three basic nematic director orientations with respect to shear flow. The blue arrow shows the shear direction.

(II) η_2: when $\hat{n}$ is parallel to $\mathbf{V}$ (shear direction),

(III) η_3: when $\hat{n}$ is perpendicular to both $\mathbf{V}$ and $\nabla\mathbf{V}$.

In unaligned sample usually the director $\hat{n}$ can be defined as

$$\hat{n} = (cos\theta\, cos\phi, cos\theta\, sin\phi,\, sin\theta) \tag{1.19}$$

where θ and ϕ are the angles of the nematic director with respect to $\mathbf{V}$ and $\nabla\mathbf{V}$. The Leslie-Ericksen constitutive equations for the viscous stress is defined as [2, 24],

$$\begin{aligned}\tilde{\sigma}_{i,j} = {} & \alpha_1 n_k A_{kp} n_p n_i n_j + \alpha_2 N_i n_j + \alpha_3 n_i N_j + \alpha_4 A_{ij} \\ & + \alpha_5 n_j A_{ik} n_k + \alpha_6 n_i A_{jk} n_k\end{aligned} \tag{1.20}$$

where α_1, α_2.....,α_6 are the Leslie coefficients, $\mathbf{A}$ is the velocity gradient tensor and $\mathbf{N}$ is the rotation of the director relative to the background fluid.

It can be shown that the apparent viscosity η (θ, ϕ) can be expressed as [2]:

$$\eta(\theta,\phi) = \eta_1\, cos^2\theta\, cos^2\phi + \eta_2\, sin^2\theta + \eta_3\, sin^2\phi\, cos^2\theta + \frac{1}{4}\,\eta_{12}\, sin^2(2\theta)\, cos^2\phi \tag{1.21}$$

where η_1, η_2, η_3 and η_{12} are Miesowicz viscosities. Here η_{12} denotes the strength of the deformation and can be neglected. The Miesowicz viscosities η_1, η_2 and η_3 can be expressed in terms of Leslie coefficients [2]:

$\eta_1 = \frac{\alpha_3+\alpha_4+\alpha_6}{2}$, when θ=0, ϕ=0,

$\eta_2 = \frac{-\alpha_2+\alpha_4+\alpha_5}{2}$, when $\theta=\pi/2$, ϕ=0,

$\eta_3 = \frac{\alpha_4}{2}$, when θ=0, $\phi=\pi/2$.

1.8 Topological defects in nematic and smectic liquid crystals

1.8.1 Defects in nematic liquid crystals

In liquid crystals defects are generated in the symmetry breaking phase transitions. In nematic liquid crystals, due to long range orientational order, they exhibit a number of topological defects called disclinations. Those defects are observed under optical polarising microscope. The core of defects can be seen as a black spot or a line because it scatters light due to the random orientation of molecules at the core. These defects are characterised by strength or winding number 's' which is denoted with an integer or half-integer number. The strength 's' indicates the number of times the director rotates by 2π around the singularity when one surrounds the defect core [4]. So mathematically 's' can be defined as the number of rotations of the director around the singularity divided by 2π. If the nematic director is confined to a parallel set of planes, then

$$\oint \frac{d\varphi}{dl} dl = 2\pi s \tag{1.22}$$

where φ denotes the orientation of the director field in a plane. The integral is taken in a counter-clock-wise direction. The Frank elastic energy with one elastic constant approximation can be expressed as

$$f_{el} = \frac{1}{2} K (\nabla\varphi)^2 \tag{1.23}$$

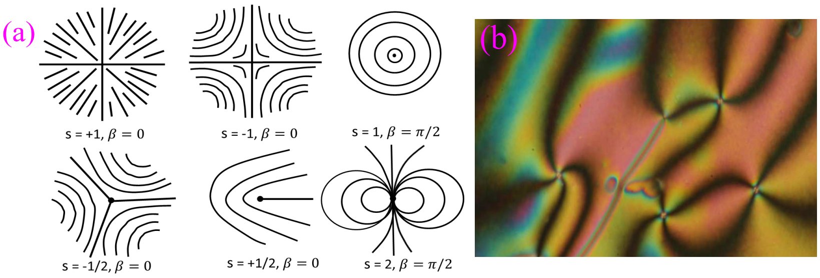

Figure 1.14: (a) Schematic representation of few defects with different strength. (b) The planar schlieren texture of a nematic liquid crystal under crossed polarisers.

The Euler-Lagrange minimisation condition corresponding to Eq. 1.23 is:

$$\nabla^2\varphi = 0 \tag{1.24}$$

The orientation of the director field φ can be defined as:

$$\varphi = s\,tan^{-1}(\frac{y}{x}) + \beta = s\alpha + \beta \tag{1.25}$$

where β is a constant. The defect strength s depends on the symmetry of the medium. In the case of nematic phase s can be any multiple of $\pm\,\frac{1}{2}$, as the director has $\hat{n} \equiv$ - $\hat{n}$ symmetry. Hence the rotational direction of the nematic director field can be expressed by positive or negative sign of the strength value. Figure 1.14(a) shows the schematic representation of defects with different strength. An example of a schlieren texture of nematic liquid crystal under crossed polarisers is also shown in the Fig. 1.14(b). In the cholesteric phase due to the molecular chirality, the spontaneous twist

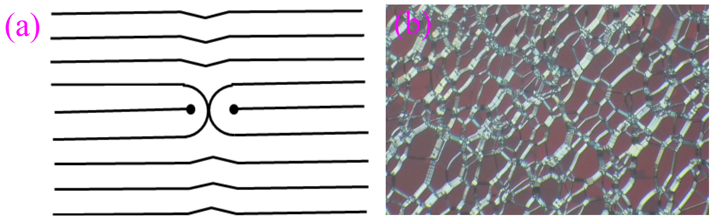

Figure 1.15: (a) The schematic representation of the cross section view of cholesteric layer arrangement in a symmetric oily-streak defect. The layers undergo a rotation of π between two constituent disclinations (shown as half circles) in the center of the streak [25]. (b) The oily-streak network of defects in planar chiral nematic cell.

is induced. It creates a complicated but stable networks of disclination lines in a planar cell, called as oily-streak defcts. In the cholesteric phase, the layers undergo a rotation of π between two disclination lines in the center of the streak (Fig. 1.15(a)) [25]. A typical texture of the cholesteric phase showing oily-streak defect network is shown in the Fig. 1.15(b).

1.8.2 Defects in smectic liquid crystals

Smectic liquid crystals exhibit dislocations due to their layered structure. Considering smectic layers whose layer normal is along the Z-axis. In the presence of distortion, there is a change in the smectic layer displacement field u which causes dislocations and it is defined as [26],

$$\oint du = (kd)\hat{z} = \vec{b} \tag{1.26}$$

where $\hat{z}$ denotes the direction of the lattice distortion, d is the layer spacing and $\vec{b}$ is called the '$Burger's\, vector$'. So the physical nature of the defect depends on the relative orientations of $\vec{b}$ and the dislocation line. A schematic representation of the screw dislocations is shown in the Fig. 1.16(a). If $\vec{b}$ is parallel to the dislocation line, it is called the "screw dislocations". Here the smectic layers change in a screw-like manner in climbing up or down by an integral number of d on going round the

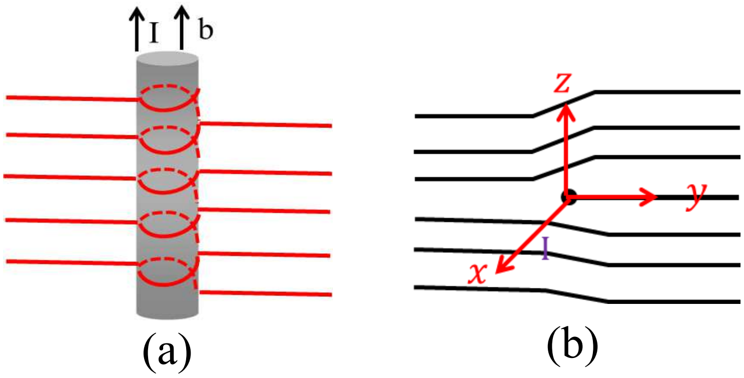

Figure 1.16: (a) Schematic representation of screw dislocations in the smectic-A phase. The cross-section shown here signifies that each layer changes height by half a layer in half a circuit of the defect core. The dislocation line is denoted by I, is parallel to $\vec{b}$ and $b = +d$. (b) An edge dislocation with $b = d$.

dislocation line once.

If $\vec{b}$ is perpendicular to the dislocation line, it is called an “edge dislocations”, as shown in the Fig. (1.16(b)). In this case a few number of layers are either added or removed from one side of the dislocation line.

1.9 Induced topological defects in nematic LCs

The colloidal dispersion in isotropic medium like water and oil has been studied since decades due to its wide range of applications. The rich variety of interaction forces are the main cause of many exciting properties in classical colloidal systems. Apart from those simple liquids, there are many complex fluids which can be used as a host medium to expand and modify the behavior of colloids. The dispersion of nano and micro particles in anisotropic liquids like thermotropic and lyotropic liquid crystals are the best example of those complex fluids and the system is called as LC-colloids. In this case the medium has a broken symmetry and an associated elastic energy of deformations. The dispersion of colloidal particles produce topological defects in the nematic liquid crystal (NLCs) and cause significant distortions of the director. Usually the nanoparticles do not create any long-range elastic distortion in the NLCs but the physical properties of the composites become significantly different from that of the pure LCs and such materials are potential for several applications [27–29]. When microparticles are dispersed in nematic LCs, they create elastic distortions and induce topological defects. This results long-range forces among the particles in the medium. These forces have no analogue in common colloidal systems where particles are dispersed in the isotropic liquids. The elastic energy stored due to the distortion in the LC medium leads to significant changes in the morphology and the mechanical properties of the system. In liquid-crystal-colloids the induced defects depend on different parameters like surface anchoring coefficient (W), radius of colloids (R) and the average Frank elastic constant K. The director field distortion around the particles is controlled by the competition between the surface anchoring energy ($\sim WR^2$) and the Frank elastic energy ($\sim KR$). Experimentally W varies from 10^{-6} to 10^{-3}. The ratio of the average elastic constant to the anchoring coefficient can be defined as $\lambda =$

K/W, where λ has dimension of length and is called as de Gennes-Kleman length. For a typical thermotropic liquid crystal $K = 10$ pN, hence depending on the anchoring coefficient, λ can vary from 0.1 to 10 μm. Depending on the value of λ, liquid-crystal-colloids can be categorised into two classes namely type-I ($R<<\lambda$) and type-II ($R>>\lambda$).

If the particle radius $R>>\lambda$, the director field around the particles becomes inconsistent with its uniform distribution in the bulk, that leads to a topological defect close to the particle. These elastic distortions are responsible for long-range anisotropic interactions of colloids in LCs. The geometry of distortions in the director field depends on the shape of the particle and the orientation of the easy axis. Depending on the anchoring strength and the confinement, usually three different types of topological defects are induced by spherical microparticles in NLCs namely hyperbolic hedgehog (dipolar or point defect), saturn ring (quadrupolar) and boojum [30,31]. If the particle of radius $R<<\lambda$ is placed in a uniform nematic LC, it does not perturb the director field much but the addition of small particles influence the elastic, viscous, dielectric and optical anisotropy properties [3].

1.9.1 Elastic dipole and quadrupole defects

In the LC-colloid system, in order to understand the effective interaction between the particles in the LC medium, it is important to realize the liquid crystal ordering near the particles. An isolated colloidal particle provides either perpendicular or parallel boundary conditions to the nematic director creating elastic distortion. The elastic distortion in the LC medium causes defect formation and the nature of defects can be controlled by the surface anchoring on the colloid and the surface confinement of the liquid crystal cell.

If the colloids with homeotropic anchoring are dispersed in a homogeneously aligned nematic LC (Fig. 1.17), the locally surrounded nematic molecules are forced to orient perpendicular to the surface without disturbing the far field director. It leads to a director frustration and consequently topological defects appear to compensate this elastic distortion (Fig. 1.17(a,b)). Here the defects appear either in the form of a black spot (Fig. 1.17(c,d)) called elastic dipole configuration or in the form of a closed loop around the particle, called as elastic quadrupole configuration (Fig. 1.17(e,f)). In dipolar case the particle exhibits radial hedgehog of topological charge +1 and

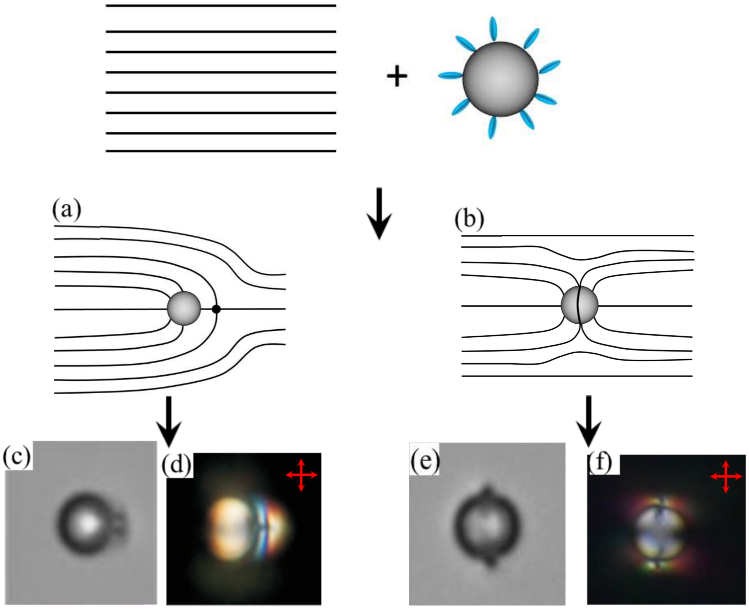

Figure 1.17: A spherical microparticle with a strong homeotropic surface anchoring dispersed into a uniformly aligned nematic liquid crystal exhibits two possible director configurations: the dipolar, where the particle has a hyperbolic hedgehog of strength -1 and a quadrupolar defect where the particle is encircled by a -1/2 disclination ring. (a),(b) The schematic representation of the nematic director field showing dipolar and quadropolar defects (c) the black spot corresponds to a point defect (e) two black spots on the top and bottom side of the particle appears due to the encircled ring. (d) and (f) appearance of the same under the crossed polarisers.

the hyperbolic defect has topological charge of -1 [31–33]. The particle-defect pair is called as elastic dipoles, since the director fields are reminiscent of the field lines of the electric dipole. Usually the dipolar colloids appear if the thickness of the nematic layer is much larger than the particle size ($d>>2R$), where the surface confinement is weaker [31]. These dipoles spontaneously assemble to form chains, called as dipolar chains (Fig. 1.18(a)). The effective interaction potential between two dipoles is about $\sim$ 12000 K_BT, when microparticle diameter is 5.2μm.

If the nematic layer thickness is smaller, the surface confinement around the particle

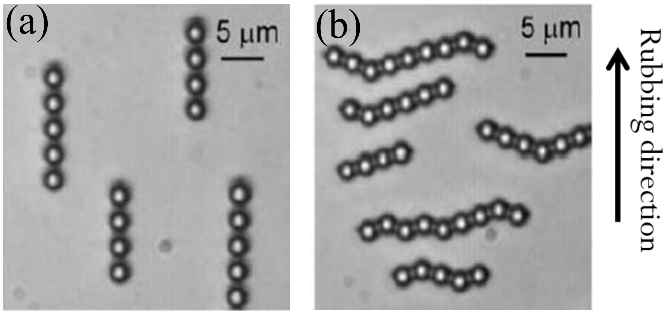

Figure 1.18: (a) Elastic dipoles spontaneously form dipolar chains along the rubbing direction (b) Elastic quadrupoles spontaneously form kinked chains perpendicular to the direction of rubbing. Adapted from ref. [31]

will be stronger and this leads to a quadrupolar defect configuration. In this case a singular Saturn ring defect of -1/2 strength disclination ring encircles the particle [30,31,33], as shown in Fig. 1.17(e,f). The Saturn ring defect appears when the dipolar field around the colloid is strongly influenced by the surface confinement. Due to the confining surfaces the opening of a point hyperbolic defect leads to a distribution of charge over a circle and it is seen as a ring around the particle. Figure 1.17(e) shows two black spots on the top and bottom of the particle, indicating a disclination ring encircling it. Figure 1.17(f) shows the elastic distortion around the particle as four bright lobes under crossed polarisers. Like dipolar colloids, quadrupolar colloids also spontaneously assemble and due to the sharing of charge between two particles, they form kinked chains, perpendicular to the nematic director (Fig. 1.18(b)). The strength of interaction potential between the quadrupoles is usually lower than the dipole-dipole interaction and it is about $\sim 3000\ K_BT$, when microparticle diameter is 5.2μm.

1.9.2 Boojum defect

The spherical colloidal particles with sufficiently strong planar anchoring of LC molecules (Fig. 1.19) develope a pair of antipodal surface topological defects in a uniformly aligned LC, known as boojums. The particle-defect pairs are called as boojum colloids (Fig. 1.19(a)) [33–35]. Figure 1.19(b) shows schematic representation of the director

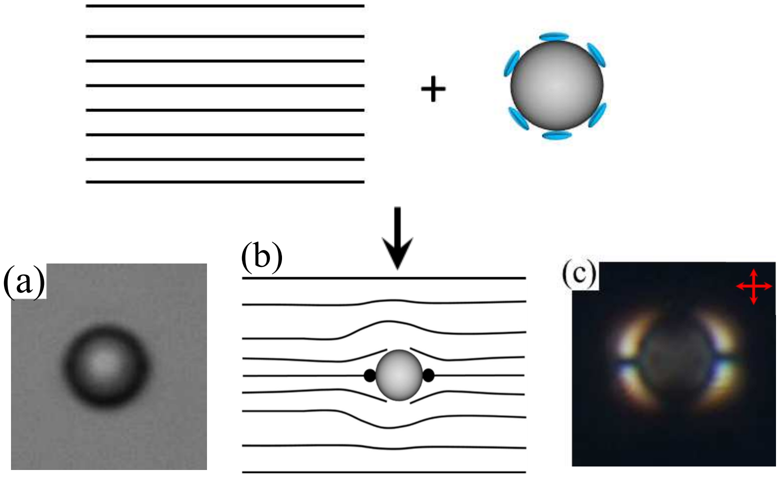

Figure 1.19: A spherical particle with planar anchoring placed into an uniformly aligned nematic LC. (a) A boojum defect of strength -1/2 as seen in CCD camera. (b) Schematic representation of nematic director field around the microsphere. (c) The elastic distortion around the microsphere observed under crossed polariser.

field distortion around the microparticles. There are two black spots clearly observed in both left and right side of the microsphere under crosed polarisers (Fig. 1.19(c)). They also have a long-range interaction and tend to self-assemble. The effective interaction potential between two boojums is about $\sim 1800\ K_BT$, for the microparticle of diameter 5.2μm.

References

[1] H. A. Barnes, J. F. Hutton, and K. Walters. *An introduction to rheology.* 1^{st}*Ed.*, Elsevier, 1989.

[2] R. G. Larson. *The structure and rheology of complex fluids.* Oxford University Press, New York, 1999.

[3] P. G. de Gennes and J. Prost. *The physics of liquid crystals.* International series of monographs on physics, Clarendon Press, 1993.

[4] S. Chandrasekhar. *Liquid Crystals.* Cambridge University Press, 1992.

[5] W. H. de Jeu. *Physical properties of liquid crystalline materials.* Liquid Crystal Monographs, Gordon and Breach, 1980.

[6] J. W. Goodby, M. A. Waugh, S. M. Stein, E. Chin, R. Pindak, and J. S. Patel. *Characterization of a new helical smectic liquid crystal.* Nature, vol. 337, pp. 449 - 452, 1989.

[7] S.R. Renn and T.C. Lubensky. *Abrikosov dislocation lattice in a model of the cholesteric-to-smectic-A transition.* Phys. Rev. A, vol. 38, no. 4, pp. 2132-2147, 1988.

[8] L. Navailles, B. Pansu, L. Gorre-Talini, and H. T. Nguyen. *Structural study of a commensurate* TGB_A *phase and of a presumed chiral line liquid phase.* Phys. Rev. Lett., vol. 81, no. 19, pp. 4168-4171, 1998.

[9] P. A. Pramod, R. Pratibha, and N. V. Madhusudana. *A three-dimensionally modulated structure in a chiral smectic-C liquid crystal.* Current Science, vol. 73, no. 9, pp. 761-765, 1997.

[10] P. A. Pramod, Y. Hatwalne, and N. V. Madhusudana. *A phenomenological model for the undulating twist grain boundary-C* phase.* Liq. cryst., vol. 28, no. 4, pp. 525-533, 2001.

[11] H. Grebel, R. M. Hornreich and S. Shtrikman. *Landau theory of cholesteric blue phases: The role of higher harmonics.* Phys. Rev. A, vol. 30, no. 6, pp. 3264-3278, 1984.

[12] D. C. Wright and N.D.Mermin. *Crystalline liquids: the blue phases.* Reviews of Modern Physics, vol. 61, no. 2, pp. 385-432, 1989.

[13] F. C. Frank. *I. liquid crystals. on the theory of liquid crystals.* Discussions of the Faraday Society, vol. 25, pp. 19–28, 1958.

[14] S. T. Wu and C. S. Wu. *Experimental confirmation of the osipov-terentjev theory on the viscosity of nematic liquid crystals.* Phys. Rev. A, vol. 42, no. 4, p. 2219, 1990.

[15] M. Dark, M. Moore, D. Shenoy, and R. Shashidhar. *Rotational viscosity and molecular structure of nematic liquid crystals.* Liq. cryst., vol. 33, no. 1, pp. 67–73, 2006.

[16] A. A. Sonin. *The surface physics of liquid crystals.* Taylor and Francis, 1995.

[17] K. Takatoh, M. Sakamoto, R. Hasegawa, M. Koden, N. Itoh, and M. Hasegawa. *Alignment technology and applications of liquid crystal devices.* CRC Press, 2005.

[18] H. J. Deuling. *Deformation of nematic liquid crystals in an electric field.* Mol. Cryst. Liq. Cryst., vol. 19, no. 2, pp. 123-131, 1972.

[19] H. Gruler and G. Meier. *Electric field-induced deformations in oriented liquid crystals of the nematic type.* Mol. Cryst. Liq. Cryst., vol. 16, no. 4, pp. 299-310, 1972.

[20] L. M. Blinov and V.G. Chigrino. *Electrooptic effects in liquid crystals.* Springer-verlag, New York, 1996.

[21] T. Mezger. *The rheology handbook.* 4th edition,2002.

[22] P. Sollich, F. Lequeux, P. Hebraud, and M. E. Cates. *Rheology of Soft Glassy Materials.* Phys. Rev. Lett., vol. 78, p. 2020, 1997.

[23] M. Miesowicz. *The three coefficients of viscosity of anisotropic liquids.* Nature, vol. 158, p. 27, 1946.

[24] I. W. Stewart, *The Static and Dynamic Continuum Theory of Liquid Crystals: A Mathematical Introduction.* Liquid Crystals Book Series, Taylor and Francis, 2004.

[25] M. Zapotocky, L. Ramos, P. Poulin, T. C. Lubensky, and D. A. Weitz. *Particle-stabilized defect gel in cholesteric liquid crystals.* Science, vol. 283, no. 5399, pp. 209-212, 1999.

[26] P. M. Chaikin, T. C. Lubensky. *Principle of condensed matter physics.* Cambridge University Press, 1998.

[27] Y. Garbovskiy. *Electrical properties of liquid crystal nano-colloids analysed from perspectives of the ionic purity of nano-dopants.* Liq. Cryst., vol. 43, no. 5, pp. 648-653, 2016.

[28] R. Basu, A. Garvey. *Effects of ferroelectric nanoparticles on ion transport in a liquid crystal.* Appl. Phys. Lett., vol. 105, p. 151905, 2014.

[29] R. Sahoo, M. V. Rasna, D. Lisjak, A. Mertelj, and S. Dhara. *Magnetodielectric and magnetoviscosity response of a ferromagnetic liquid crystal at low magnetic fields.* Appl. Phys. Lett., vol. 106, p. 161905, 2015.

[30] P. Poulin, H. Stark, T. C. Lubensky, and D. A. Weitz. *Novel Colloidal Interactions in Anisotropic Fluids.* Science, vol. 275, no. 5307, p. 1770, 1997.

[31] I. Musevic, M. Skarabot, U. Tkalec, M. Ravnik, and S. Zumer. *Two-dimensional nematic colloidal crystals self-assembled by topological defects.* Science, vol. 313, no. 5789, pp. 954-958, 2006.

[32] M. Tasinkevych, D. Andrienko. *Colloidal particles in liquid crystal films and at interfaces.* Condens. Matter Phys., vol. 13, no. 3, pp. 33603: 1-20, 2010.

[33] H. Stark. *Physics of colloidal dispersions in nematic liquid crystals.* Phys. Rep., vol. 351, no. 6, pp. 387-474, 2001.

[34] M. R. Mozaffari, M. Babadi, J. Fukuda, and M. R. Ejtehadi. *Interaction of spherical colloidal particles in nematic media with degenerate planar anchoring.* Soft Matter, vol. 7, no. 3, pp. 1107-1113, 2011.

[35] K. P. Zuhail and S. Dhara. *Temperature dependence of equilibrium separation and lattice parameters of nematic boojum-colloids.* Appl. Phy, vol. 106, p. 211901, 2015.

2

Experimental Setup

2.1 Introduction

In this chapter we briefly discuss about different experimental techniques used in our experiments. We used a standard stress controlled rheometer MCR-501 (Anton Paar), with different measuring systems. Here we discuss the working of a modular compact rheometer with various measuring systems and different techniques such as rheo-microscopy, rheo-SALS (small angle light scattering), magneto-rheology (MR) etc. We also measured several physical properties of the liquid crystals for understanding the rheological properties. Hence apart from rheometry, we discuss about some electro-optic techniques which have been used to measure some physical properties of liquid crystals like dielectric anisotropy $\Delta\epsilon$, splay (K_{11}), bend (K_{33}) elastic constants and rotational viscosity (γ_1).

2.2 Rheometer

Anton Paar MCR-501 is the modular compact rheometer. It has an air bearing supported EC (Electrically Commutated) synchronised motor. The MCR consists of a high-resolution optical encoder, based on data oversampling technology [1]. It controls the angular deflection and can measure accurately the very small angular displacements down to 0.1 μrad. It has low fluctuation and high performance due to the digital signal processing (DSP) technology. MCR has an accuracy in the torque measurements and normal force resolution. There are two air bearings to support the synchronous

EC motor named as radial and axial. The radial bearing normally stabilize the centre rod in the motor part, whereas the axial bearing carry the whole weight of the rotating parts. MCR is capable of measuring the low-torque down to a minimum of 0.5 nNm due to the support of those air bearings. It has an important component i.e normal force sensor, which is connected with the air bearings. Basically the normal force sensor can detect the movement of the bearings. It measures the normal force both in upward (positive) and downward (negative) directions depending upon the sample behavior during the steady and dynamic state. The Rheoplus software of the rheometer is used to control and analyse the rheological measurements. The TruGap technology is used to regulate the minimum and exact gap size between the two plates of measuring geometry. The bottom plate of the rheometer is an immovable one and the upper plate is movable. The photomicrograph of MCR-501 rheometer is shown in the Fig. 2.1. The rheometer is equipped with a Peltier temperature controller system with a peltier hood to maintain the required temperature, within an accuracy of 0.02°C. The rheometer is connected with an oil-free compressor for the functioning of air bearings, which provides 5-8 bars pressure to the rheometer. There is also a chiller attached with it to circulate the water throughout the system to sustain the

Figure 2.1: Photograph of the rheometer (MCR-501).

room temperature (25°C). All the rheological measurements are carried out through the Rheoplus software [1]. According to the response of the sample, a broad range of measuring systems are used to measure the rheological properties.

2.3 Measuring systems

The measuring geometries, responsible for imposing a shear flow are divided into three basic categories i.e., (1) cone and plate (CP) measuring system (2) parallel-plate (PP) measuring system and (3) Cylindrical measuring systems (Co-axial cylinder (CC) and double-gap (DG) cylinder measuring systems). In our experiments we used two measuring geometries i.e., cone and plate and parallel-plate. Here we briefly discuss about these measuring systems.

2.3.1 Cone and plate measuring system

The cone and plate (CP) measuring system has two important components. A bob with a conical surface (upper plate) and a fixed plate with a flat surface (lower plate). The accuracy in the measurements is basically determined by the cone radius 'R' and the cone angle 'α' of the conical surface of the measuring system. There are two different diameters of upper plate i.e 25 mm and 50 mm. The 50 mm geometry gives more accuracy than 25 mm in case of low viscous fluids. It is because a larger radius increases the sensitivity to low torque or shear stress values due to a large shear area. But the sample with higher viscosity case, the smaller diameter measuring system (25 mm) is used. A schematic diagram of a cone plate measuring system is shown in the Fig. 2.2.

In the case of CP measuring systems the shear rate value is independent of the radius. Hence the shear rate is uniform throughout the entire gap of the measuring system. So this is the most favourable measuring system than parallel-plate and cylindrical measuring system. To obtain more accuracy in the measurements, the truncated cone tip of the upper plate should touch the lower plate at one point. In

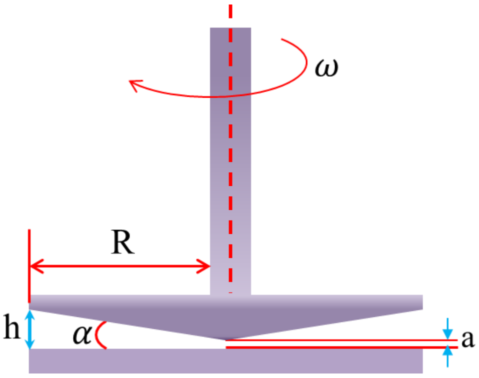

Figure 2.2: Schematic diagram of cone and plate measuring system. The symbols represent the following parameters: R - cone radius, h - gap between the two plates at edge, α - cone angle, ω - angular frequency and a - truncated gap between the plates.

CP measuring systems the measuring position (gap between the truncated cone tip and the lower plate) is always fixed after mounting the sample on the lower plate. The fixed measuring gap lengths are given below.

i. CP 25 - 1° / TG → $d = 50\mu$m

ii. CP 25 - 2° / TG → $d = 50\mu$m

iii. CP 50 - 0.50° / TG → $d = 49\mu$m

iv. CP 50 - 1° / TG → $d = 48\mu$m

Here TG determines the true gap or measuring gap between the two plates. CP 25 indicates the cone-and-plate measuring system of diameter 25 mm. The gap must be completely filled with respect to the plate diameter. Relatively less volume of the sample is required due to the conical surface of the upper plate. A peltier hood is placed to reduce the temperature gradients in the sample. The maintenance of this geometry is quite easy comparing to other geometries.

2.3.2 Parallel-plate measuring system

The parallel-plate (PP) measuring system consists of two plates, where both the upper and lower plates are flat. The upper plate is movable one where the lower plate is fixed. The geometry of the plate is determined by the plate radius R. The schematic diagram of the parallel-plate measuring system is represented in the Fig. 2.3.

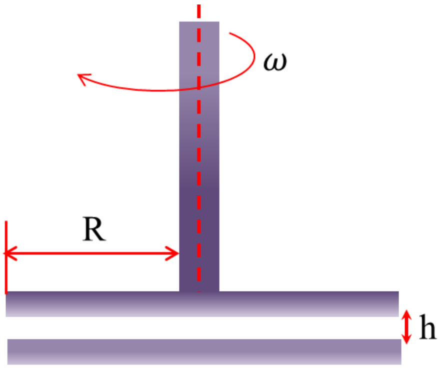

Figure 2.3: Schematic diagram of parallel-plate measuring system. The symbols represent the following parameters: R - plate radius, h - gap between the two plates, ω - angular frequency.

In the case of parallel plate measuring system, the gap between two parallel plates "h" must be less than the plate radius R i.e $h << R$. The shear rate depends on the radius of the upper plate, hence it is inhomogeneous throughout the sample. There is no fixed gap maintained in between two parallel plates. So it is suitable to use for the dispersed fluids containing larger particles. The larger diameter of 50 mm geometry is required to measure the rheological properties of low viscous fluids and large particle size samples. The gap maintained between the two plates should be at least 5 times larger than the particle size. A large volume of sample is required due to the flexibility in gap adjustment in between two parallel plates. Like CP measuring system, the peltier hood is used to maintain an uniform temperature through out the sample. We have two different parallel plate measuring systems having different diameter of plates. These are:

(i) PP - 25/ TG

(i) PP - 50/ TG

2.4 Rheo-Microscopy

In general rheological measurements provide the information about the macroscopic mechanical properties. However, the mechanical properties can be easily understood by inspecting the microstructures and the microstructures can be seen by using a rheo-microscopy technique. The simultaneous study of microstructures and mechanical properties always provide better understanding about the sample [2]. Rheo-microscopy technique is also very much useful to study all kinds of complex fluids like surfactant solutions, colloidal suspensions, polymer solutions and polymer blends etc. We used a rheo-microscopy setup, developed by Anton-Paar which can be directly attached with the rheometer.

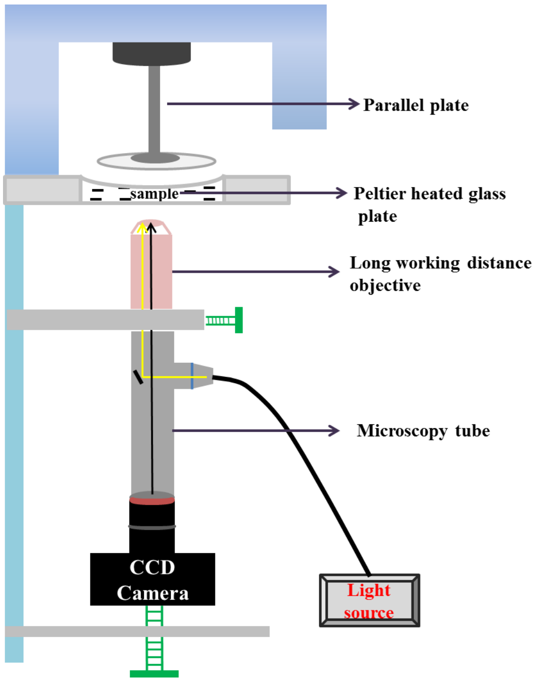

Figure 2.4: Schematic diagram of the rheo-microscopy setup. The setup is attached under the bottom plate. The images are taken in the reflection mode.

The rheo-microscopy setup consists of a CCD camera, a microscopy tube and a long working distance objective [1]. A schematic diagram of the setup is shown in Fig.

2.4. In our experiments we used a Nikon-20X objective with numerical aperture (NA) 0.4. Apart from these, it is also equipped with a parallel-plate geometry of diameter 43 mm, which is made of glass and can prevent unwanted reflections. A thickness of 6 mm glass is used as bottom plate to provide a good mechanical stability and a temperature control. The sample is illuminated by using a polarized light through the objective from the bottom. An analyzer is placed in the microscope tube before the CCD camera. The microscope tube is adjustable in the y and z directions for focusing. An additional peltier hood is used to maintain an uniform temperature throughout the sample. The maximum temperature can be maintained in this setup is about 80°C.

2.5 Rheo-Small Angle Light Scattering (Rheo-SALS)

It's very often required to study the microscopic structures of the sample for better understanding of their rheological properties. The small angle light scattering (SALS) technique is used for investigating the detailed structure-property relationships of complex fluids [3]. A schematic diagram of the SALS setup is shown in Fig. 2.5.

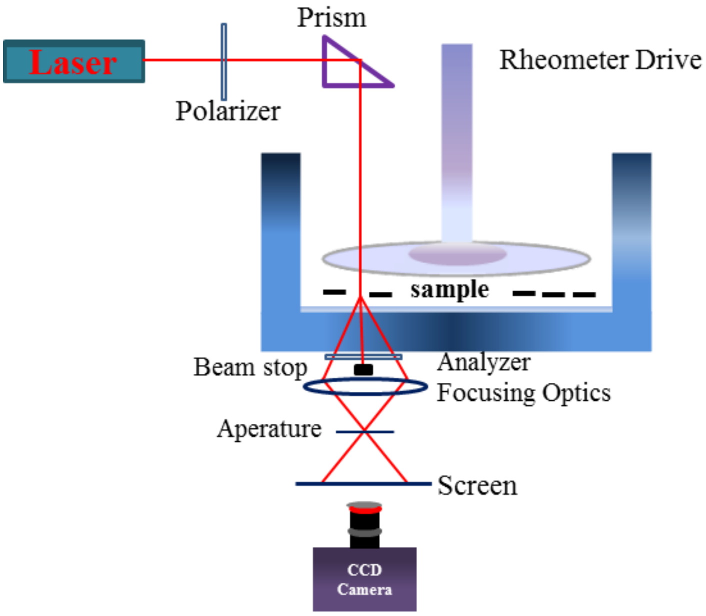

Figure 2.5: Schematic diagram of the small angle light scattering setup.

The setup consists of a prism, polarizer-analyzer, focusing optics, CCD camera and a screen [1]. We used the parallel-plate measuring system, made of glass with diameter 43 mm. A diode laser with a wavelength of 658 nm is connected with the setup. A beam of laser light is deflected into the upper plate through the prism and incident on sample at lower plate. According to the fluctuations (orientation or concentration) in the sample, the incoming light is scattered and passes through the analyzer. After passing from the analyzer, the scattered light is collected by a focusing optics and directed into the screen. Then the CCD camera records the scattering patterns from the screen. The camera can be synchronized directly from the rheometer software.

The Rheo-SALS setup helps in providing the structural information simultaneous to the rheological properties [4]. The principle of SALS is based on the angular distribution of the scattered light induced by the incoming laser beam. Hence the structural informations can be obtained and analysed from the scattered light distribution with respect to the angle and intensity. The elastically scattered light intensity is basically dependent on the concentration and orientation fluctuations of the micro-domains. Depending on the requirement, the polarizer (P) and the analyzer (A) can be used either perpendicular or parallel to each other. If P and A are crossed, then it is called depolarized scattering. It is sensitive on orientation fluctuations. On the other hand if P and A are parallel to each other, then it is called polarized scattering. It is sensitive on concentration as well as orientation fluctuations. In our experiments we kept P and A are crossed with each other to study about the orientation fluctuations of the director. The absolute value of the scattering vector is given by [5]

$$q = \frac{4\pi}{\lambda} sin(\theta/2) \tag{2.1}$$

where q is the scattering vector, λ is the wavelength of the light and θ is the scattering angle. The accessible scattering angle ranges from 2° to 12°, which gives a scattering vector q from 0.3 μm^{-1} to 2 μm^{-1}. The maximum temperature of 70°C can be achieved in this setup. We analyzed the SALS patterns with the help of NewSals software.

2.6 Magneto-Rheology

The magneto-rheological device (MRD) is an important accessory of MCR rheometer which facilitates all rheological tests simultaneously under the application of magnetic field. The measuring geometry is provided with parallel-plate arrangement, having 20mm plate diameter (PP20/MRD/TI). A schematic diagram of the magnetorheology setup is shown in the Fig. 2.6. There is a magnetic coil attached below the lower plate of the rheometer. The magnetic field is produced by applying an electric current to this coil. The maximum field upto 1T can be provided to the bottom plate. A magnetic cover with two leads serves as to prevent the temperature gradient and the magnetic

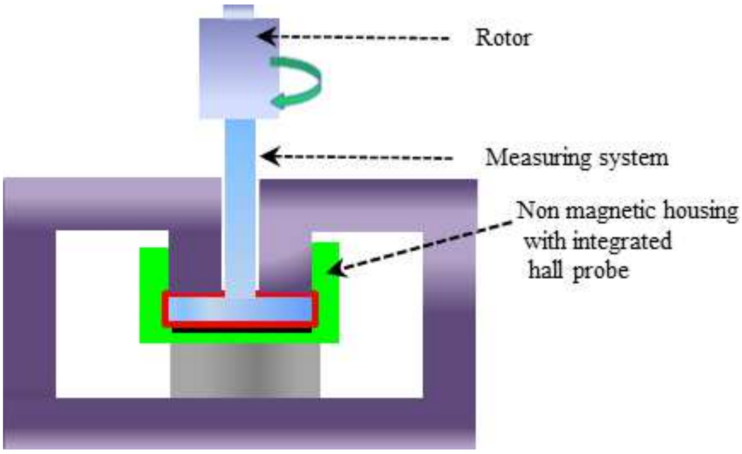

Figure 2.6: Schematic diagram of the magneto-rheological device.

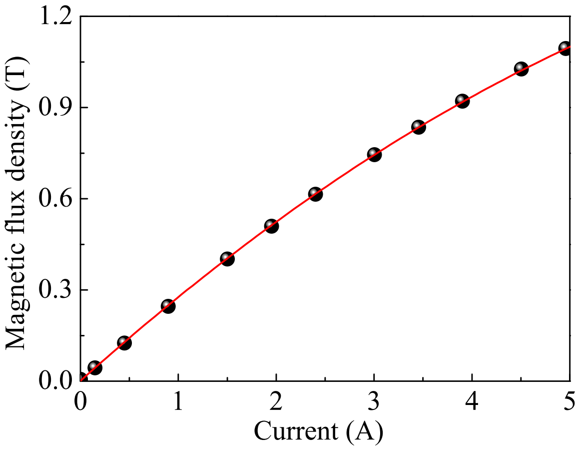

Figure 2.7: The calibration of magnetic flux density with current.

field fluctuations in the sample. The magnetic field is controlled by controlling the current produced by the power source. The magnetic current is calibrated with the magnetic field by an external teslameter. The calibrated graph is shown in the Fig. 2.7. We maintained a plate-gap of 0.2 mm for our measurements. The sample is placed uniformly on the bottom plate to avail a magnetic flux density. The temperature of the MRD can be controlled by using a fluid circulator. We used chiller filled with water for providing the required temperature to the sample. The maximum temperature upto 70°C can be obtained in this setup.

2.7 Preparation of liquid crystal cell

To understand the rheological properties, we needed to measure some physical properties of the liquid crystals. We adapted some standard electro-optical techniques to measure them. Here we briefly discuss the relevant setup.

We prepared liquid crystal cells for measuring some physical properties (non-rheological). The cells are prepared by using two indium-tin-oxide (ITO) coated glass plates, where the ITO layer thickness is about 1500 Å and the resistivity is 15-20 Ω/cm^2. The ITO coated glass plates are cleaned thoroughly by sonication using distilled water, acetone and hexane. After drying them completely we spin coat with different polyimides for different surface anchoring (planar and homeotropic). The glass plates are treated with polyimide AL-1254 and cured at 180°C (for 1 hour) for planar or homogeneous alignment. The homeotropic alignment of the LC molecules are obtained by treating the glass plates with JALS-204 and cured at 200°C (for 1 hour 15 mins). The planar treated glass plates are rubbed unidirectionally through a rubbing machine to align the LC molecules in a certain direction. The two rubbed glass plates are placed one above other in an antiparallel direction so that the active electrode regions are overlapped with each other. Then they are attached by a mixture of UV curable adhesive mixed with silica beads of required diameter. The cell thickness is measured with an Ocean optics spectrometer (HR 4000CG-UV-NIR) by using interferometric technique [6]. The corresponding spectrum is analysed through Spectra-suite software. The spectrum consists of alternative maxima and minima and the thickness (d) of the cell is calculated by using the formula, $d = \frac{\lambda_m \lambda_n}{\lambda_n - \lambda_m} \times \frac{n-m}{2}$, where λ_m and λ_n are wavelengths of m^{th} and n^{th} maxima or minima. The electrical connections to the cells are given by soldering with copper wires. The schematic representation of top view of a liquid crystal sample cell is shown in the Fig. 2.8.

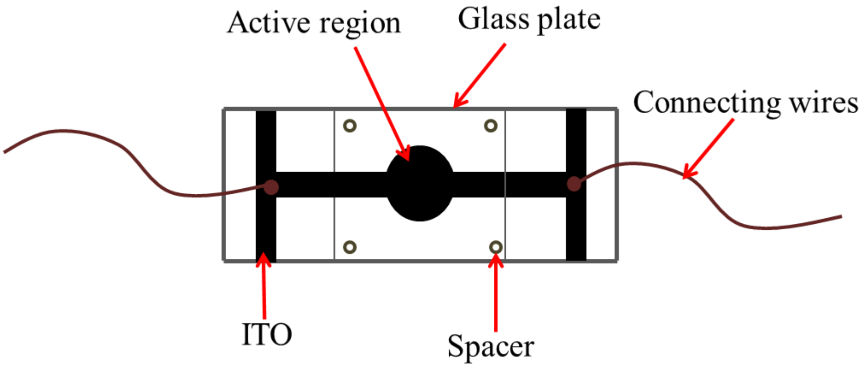

Figure 2.8: Schematic diagram of the liquid crystal sample cell made of ITO coated glass plates. The circular region shows the overlapped electrode region.

2.8 Electro-optic techniques for measuring physical properties

2.8.1 Measurement of dielectric constant

The ITO cell with an effective area A and thickness d acts as a capacitor. First we measured the empty capacitance ($C_\circ$) by an impedance analyser (Novo control, Alpha-A). Then the cells were filled with the sample either in the isotropic or in the nematic phase. We measured temperature dependant capacitance by the impedance analyser with a constant frequency 1 kHz. The ratio of capacitance with and without (empty capacitance) sample gives the dielectric constant (ϵ). The dielectric constant measured in planar and homeotropic cells provide $\epsilon_\perp$ and $\epsilon_{||}$ respectively. The dielectric anisotropy of the sample is given by $\Delta\epsilon = \epsilon_{||}$ - $\epsilon_\perp$.

2.8.2 Measurement of splay elastic constant (K_{11})

The splay elastic constants is measured by using an electro-optic technique. The voltage dependent optical retardation of a planar aligned sample is measured to estimate the splay elastic constant K_{11}. The technique is known as phase modulation technique [7, 8]. We used photoelastic modulator (PEM-100, Hinds Instruments), a Helium-Neon laser (Thor Labs), and a lock-in amplifier (Ametek, SR-7265) to make this setup. The schematic diagram of an experimental setup is shown in the Fig 2.9. The experiments are done by applying an electric field perpendicular to the nematic director in a well aligned cell. Then the optical phase difference is measured as a function of applied voltage using phase modulation technique. Above a certain applied voltage, the nematic director starts orienting with respect to the field, called Freedericksz transition and the corresponding voltage is called threshold voltage. The details about the Freedericksz transition are discussed in chapter-1. K_{11} can be calculated directly from the Freedericksz threshold voltage (V_{th}) by:

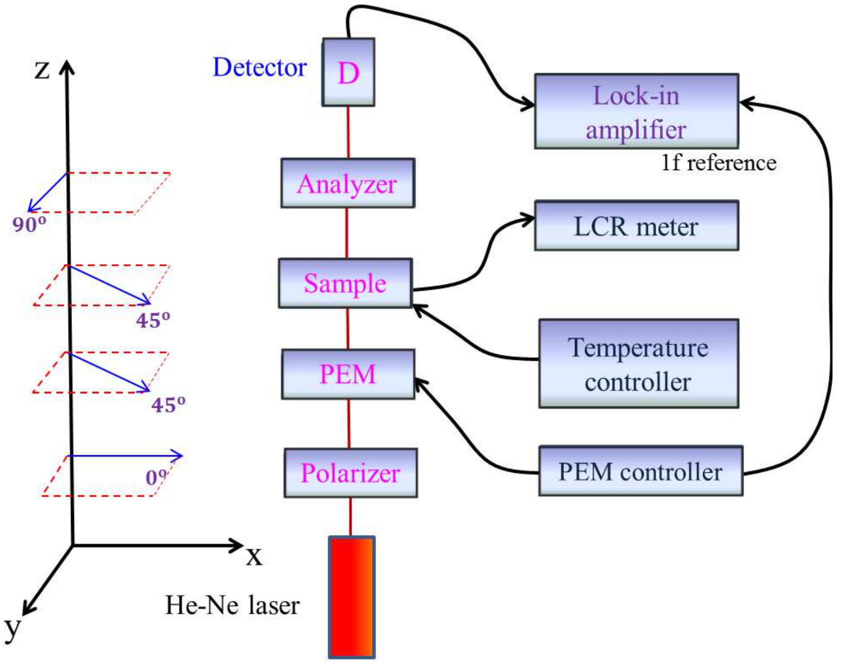

Figure 2.9: Experimental setup to measure elastic constants using PEM.

$$K_{11} = \epsilon_o \Delta\epsilon \, (V_{th}/\pi)^2 \tag{2.2}$$

where $\Delta\epsilon = \epsilon_{||} - \epsilon_{\perp}$, is the dielectric anisotropy.

2.8.3 Measurement of rotational viscosity (γ_1)

Rotational viscosity (γ_1) is measured using the phase-decay-time measurement technique. To measure the rotational viscosity (γ_1) we adopted relaxation method [9]. In this technique the transmitted light intensity is measured through a planar aligned LC cell to obtain the optical phase as a function of time. The schematic diagram of an experimental setup to measure rotational viscosity is shown in the Fig 2.10.

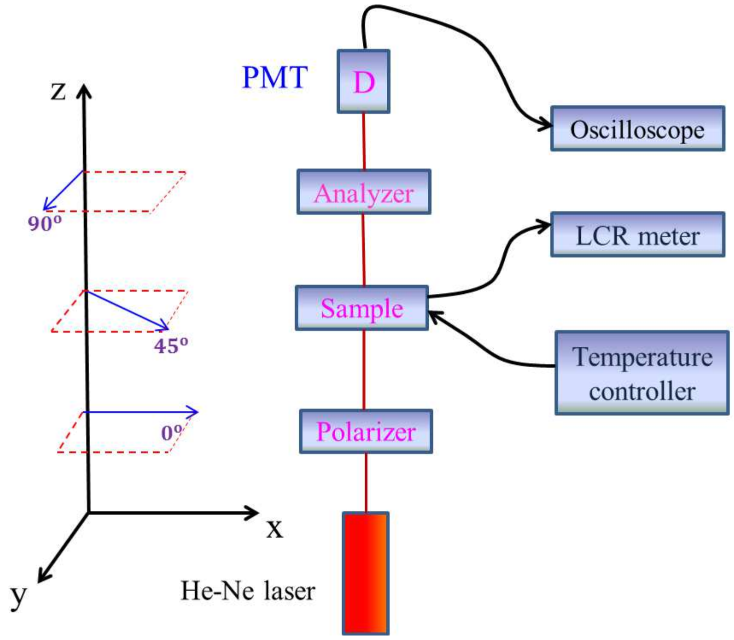

Figure 2.10: Experimental setup for measuring rotational viscosity.

The experimental procedure is followed by two steps (i) measurement of voltage dependent intensity at a fixed temperature and (ii) measurement of time dependent transmitted intensity after switching off the voltage. The voltage dependent transmitted intensity is measured to get the maxima and minima. A representative variation of the voltage dependent transmitted intensity of a standard liquid crystal at room temperature is shown in the Fig. 2.11(a). A small bias voltage (V_b) is applied and then it is switched off to measure the relaxation transmission intensity of the liquid crystal by using an oscilloscope.

The phase change $\delta(t)$ as a function of time (t) is measured from the time dependent

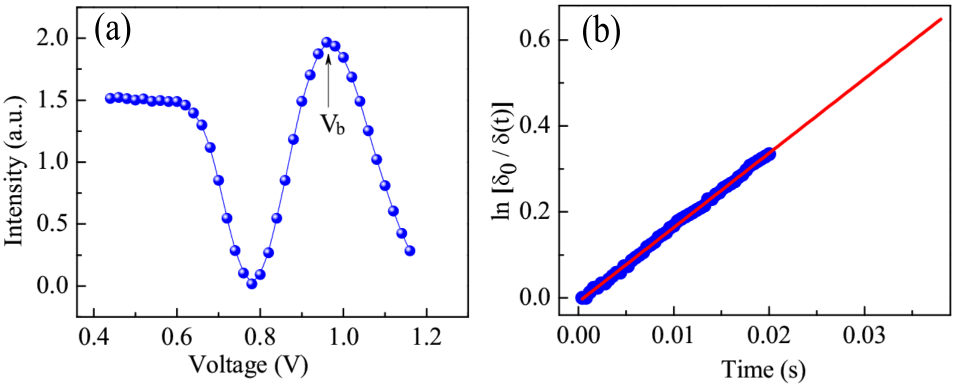

Figure 2.11: (a) The voltage dependent transmission intensity of a standard liquid crystal. (b) A representative of linear variation of ln[$\delta(0)/\delta(t)$] with time (t).

intensity, $I(t)$, using the following equation:

$$I(t) = I_0 sin^2\left[(\Delta_{tot} - \delta(t))/2\right] \tag{2.3}$$

where I_0 is the maximum intensity change.

The decay time (t) is given by the following equation [9, 10] :

$$\delta(t) = \delta(0)\, exp(\frac{-2t}{\tau_0}) \tag{2.4}$$

where $\delta(0)$ is the total phase change of the LC cell under a bias voltage V_b. The slope of the linear plot $ln[\delta(0)/\delta(t)]$ is $2/\tau_0$, and this gives the relaxation time (τ_0) (Fig. 2.11(b)). The rotational viscosity (γ_1) of the sample is given by:

$$\gamma_1 = \frac{\tau_0 K_{11} \pi^2}{d^2} \tag{2.5}$$

where d is the thickness of the cell.

References

[1] *Anton-paar instruction manual.*

[2] J. Lauger and P. Heyer. *Rheo-Microscopy: Simultaneous structural and rheological information.* Annual Transactions of the Nordic Rheology Society, vol. 20, pp. 179-181, 2012.

[3] A. R. Uribe, B. A. Tenorio, and M. E. R. Guzman, *A Small-Angle Light Scattering instrument to study soft condensed matter.* Rev. LatinAm. Metal. Mat, vol. 30, no. 1, pp. 190-200, 2010.

[4] J. Lauger, P. Heyer, and G. Pfeifer. *A new integrated Rheo-Small Angle Light Scattering (Rheo-SALS) device.* Annual Transactions of the Nordic Rheology Society, vol. 12, pp. 137-140, 2004.

[5] J. Lauger, P. Heyer, and G. Pfeifer. *Rheo Small Angle Light Scattering (Rheo-SALS) and Rheo-Microscopy as tools for investigations of structure-property relations in complex fluids.* Annual Transactions of the Nordic Rheology Society, vol. 14, pp. 193-196, 2006.

[6] K. Yang. *Measurements of empty cell gap for liquid-crystal displays using interferometric methods.* J. Appl. Phys., vol. 64, no. 9, pp. 4780-4781, 1988.

[7] G. Barbero and L.R. Evangelista. *An elementary course on the continuum theory for nematic liquid crystals.* World Scientific, Singapore, 2000.

[8] P. Sathyanarayana, B. K Sadashiva, and S. Dhara. *Splay-bend elasticity and rotational viscosity of liquid crystal mixtures of rod-like and bent-core molecules.* Soft Matter, vol. 7, no. 18, pp. 8556-8560, 2011.

[9] S. T. Wu and C. S. Wu. *Experimental confirmation of the Osipov-Terentjev theory on the viscosity of nematic liquid crystals.* Phys. Rev. A, vol. 42, no. 4, pp. 2219-2227 (1990) .

[10] S. T. Wu. *Phase retardation dependent optical response time of parallel-aligned liquid crystals.* J. Appl. Phys., vol. 60, no. 5, pp. 1836-1838, (1986).

3

Rheology of twist-grain-boundary-A liquid crystals

3.1 Introduction

Structural disorder or defect in general affects the mechanical properties of all materials. In solid materials the disorder or the defects are created or pinned down by impurities for desired mechanical properties. Many anisotropic fluids such as liquid crystals possess topological defects. The network of defects in such systems can respond to shear, and hence their contribution to the rheological properties is expected to be significant. The density of defects in liquid crystals can be enhanced by adding colloidal particles into the liquid crystals [1–3]. Basappa *et al.* showed in the lyotropic lamellar system that adding particles ($\sim 9\mu$m) enhances the elastic moduli and the elasticity arises mainly due to the defect network [1]. Ramos *et al.* studied the rheology of defect networks by dispersing colloidal particles ($1\,\mu$m) into the cholesteric liquid crystals and found a defect-mediated solid behavior of the cholesteric phase [2]. Bandyopadhyay *et al.* showed that the elasticity of LC-aerosil (7nm) composites of SmA liquid crystal (octyl cyanobiphenyl (8CB)) is enhanced compared to the pristine sample [3]. Recently the enhancement of elasticity due to the network of defect lines entangled with colloidal particles in liquid crystals has been reported by Wood *et al.* [4]. Generally, the viscoelastic properties in such composite systems are enhanced and their dynamics can be explained based on the soft-glassy-rheology or the theory of rubber elasticity. However, soft materials with long-range periodic structural disorder due to the defects (dislocations) and the grain boundary composed of an array of dislocations are rare and their viscoelastic properties are unexplored. One such very unusual soft material is type-II smectic-A, known as the twist grain boundary-A (TGB_A) liquid crystal. In this phase the defects are inherent to the structure and hence can be termed as intrinsic or structural defects.

The twist grain boundary phases (TGB_A) are frustrated phases, generally exist in between the cholesteric and the smectic phases. The detailed structure of this phase is discussed in chapter-1. The analogy between superconductors and smectic liquid crystals was first proposed by de Gennes [5], who predicted one intermediate phase with a lattice of dislocations in smectics. Renn and Lubensky showed that the intermediate phase of highly chiral type-II materials consist of a twisted arrangement of blocks of SmA liquid crystals, separated by twist grain boundaries, which are made of an array of screw dislocations [6, 7]. The contrary structure of smectic-like layering and cholesteric-like twist was experimentally discovered in highly chiral liquid crystals by Goodby *et al.* [8] and was characterized by several experiments [9, 10]. Soon after the discovery there were some reports on the observation of several variants of TGB_A, such as a TGB_C, TGB_{C^*} [10–12]. Apart from the TGB phases, there also exist a three dimensionally modulated chiral smectic-C phase, called $UTGB_{C^*}$ [13]. The detailed structure of this phase is discussed in chapter-1.

In the TGB_A phase, the interacting dislocations form the grain boundary and the interaction among the grain boundaries stabilizes the TGB_A structure. There are several experimental reports on the structure, electro-optic, and dielectric properties of various TGB liquid crystals [13, 14]. However, the viscoelastic properties of this phase remained unexplored. In this chapter we discuss the rheological properties of TGB_A, $UTGB_{C^*}$ and SmC^* phases. Usually TGB_A phase exists over a very narrow range of temperature, hence it is difficult to perform the experiments. It has been shown that the temperature range can be enhanced by adding both chiral and nonchiral compounds in certain proportions. In this experiment we prepared a binary mixture that exhibits a large temperature range of TGB_A phase.

3.2 Experimental

We prepared a binary mixture of two compounds namely, 4-(2$'$-methyl butyl phenyl 4$'$-n-octylbiphenyl-4-carboxylate (CE8) and 2-cyano-4-heptyl-phenyl-4$'$-pentyl-4-biphenyl carboxylate [7(CN)5]. CE8 is a chiral and 7(CN)5 is a nonchiral compound and both were synthesized by our collaborators in Poland. The detailed phase diagram of the binary mixtures was reported by Pramod *et al.*, as shown in Fig. 3.1. [12, 14].

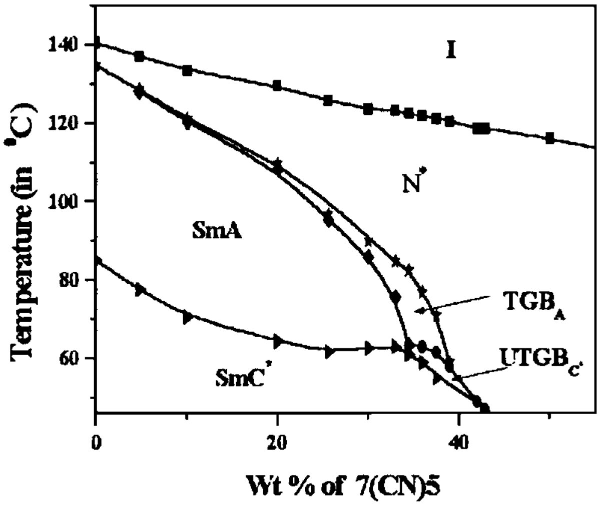

Figure 3.1: The phase diagram of the binary mixtures of CE8 and 7(CN)5. Adapted from ref. [12]

Based on the above phase diagram (Fig. 3.1), we prepared a binary mixture by taking 63.6 $wt\%$ of CE8 and 36.4 $wt\%$ of 7(CN)5 to get a large temperature range of the TGB_A phase. We heated the sample above the isotropic phase and mixed physically by using a thin glass rod. Polarized optical microscope (POM) shows following phase transitions on cooling: I 120.2°C BP 119°C N^* 80°C TGB_A 62.1°C $UTGB_{C^*}$ 59.8°C SmC^*. It may be noted that the temperature range of TGB_A is about 18°C and $UTGB_{C^*}$ is very short, about 2°C. The temperature range of TGB_A is much larger than that usually observed in a single liquid crystal compound. We performed all the rheological measurements by using a stress-controlled rheometer with the cone and plate measuring system of diameter 25 mm, cone angle 1°, and with a minimum gap of 50 μm (the gap between the plate and the truncated cone). After mounting the sample, we heated it to the isotropic phase and all the experiments were performed in cooling. The sample was then presheared for about 400 s^{-1} with a shear-rate of 10 s^{-1} before the measurements.

3.3 Results and discussion

3.3.1 Texture and physical observations

First we made some preliminary observations by filling the sample in a planar cell under optical polarizing microscope (OPM). We observed the typical textures of various phases, as presented in Fig. 3.2. The N^* phase exhibits the typical defect network of the “oily-streak” [Fig. 3.2(a)]. The TGB_A phase shows almost homogenous texture and that the slight nonuniformity in the color is due to the nonuniform alignment of the helix axis at different regions ([Fig. 3.2(b)]. We also observed a short temperature range of the $UTGB_{C^*}$ phase below the TGB_A phase with a characteristic square-grid pattern. Further, by lowering the temperature we observed SmC^*, where the square grid patterns are still present [Fig. 3.2(c)], and it can be removed by slightly shearing one of the plates.

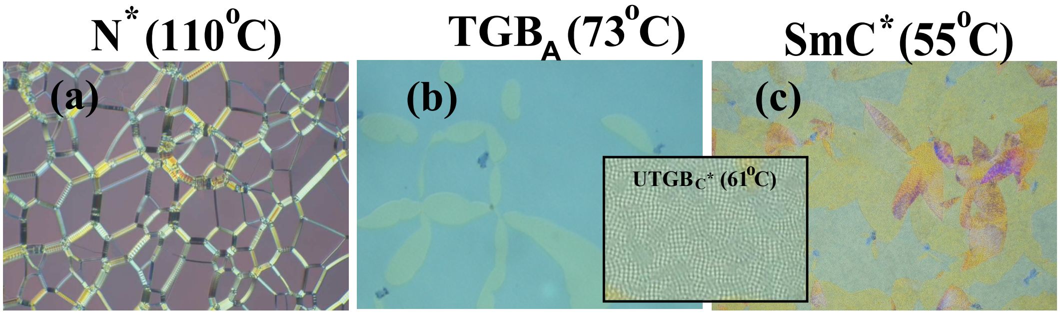

Figure 3.2: Textures observed under polarizing optical microscope (POM) at different temperatures (a) 110°C (N^*) (b) 73°C(TGB_A), and (c) 55°C (SmC^*). A square grid pattern appears in between TGB_A and SmC^* phase indicating the $UTGB_{C^*}$ phase, as shown in the box.

The physical appearance of the sample at various tempeartures is shown in the Fig.

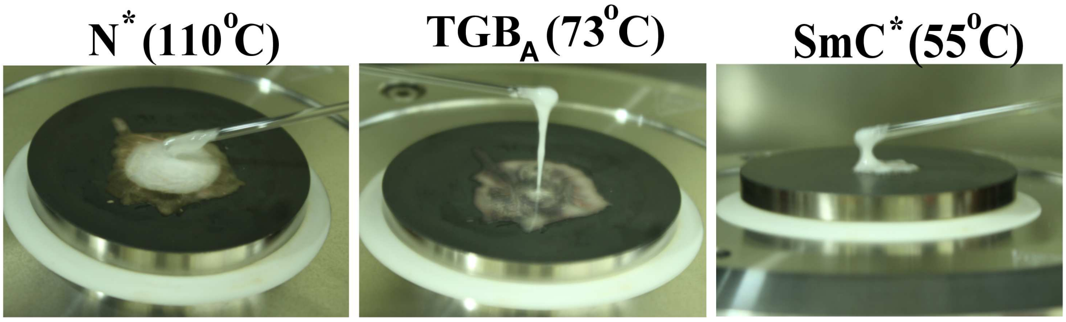

Figure 3.3: The physical appearance of the sample while trying to pull it up by a glass rod at different phases.

3.3. We performed this observation under mechanical disturbance such as pulling it up by a thin glass rod (after mounting the sample on the bottom plate of the rheometer). It appears that N^* phase tends to flow easily like a liquid. The TGB_A phase appears like a sticky fluid and SmC^* is kind of a semi-solid that does not flow easily.

3.3.2 Rotational measurements

First we performed the temperature dependent shear viscosity at a constant shear rate 100 s^{-1}, to see all the phase transitions.

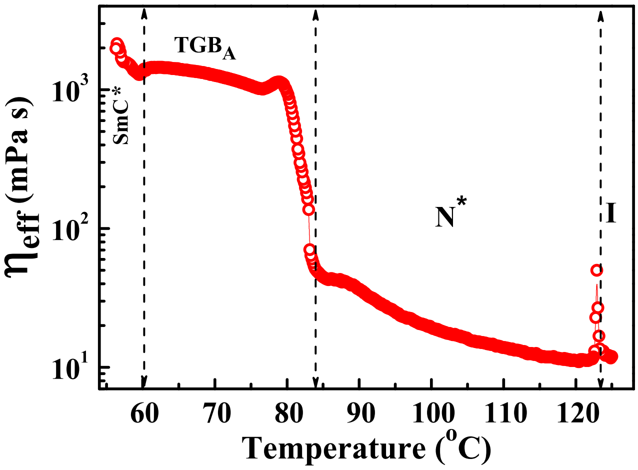

Figure 3.4: Variation of effective shear viscosity as a function of temperature at a constant shear rate 100 s^{-1}.

The temperature dependent shear viscosity is shown in Fig 3.4, where we observed three phase transitions: I 123°C N^* 83.5°C TGB_A 60.2°C SmC^* clearly. These transition temperatures are slightly different (within 2 - 3°C), compared to the transitions observed under POM. This is due to the temperature gradient of the rheometer plate or the difference in the temperature calibration. We observed there is a gradual increase in the viscosity in the cholesteric phase. Then there is a large increase in the viscosity at the N^* to TGB_A transition followed by SmC^* phase. The reason of large increase in viscosity in both TGB_A and SmC^* phase have been explained later.

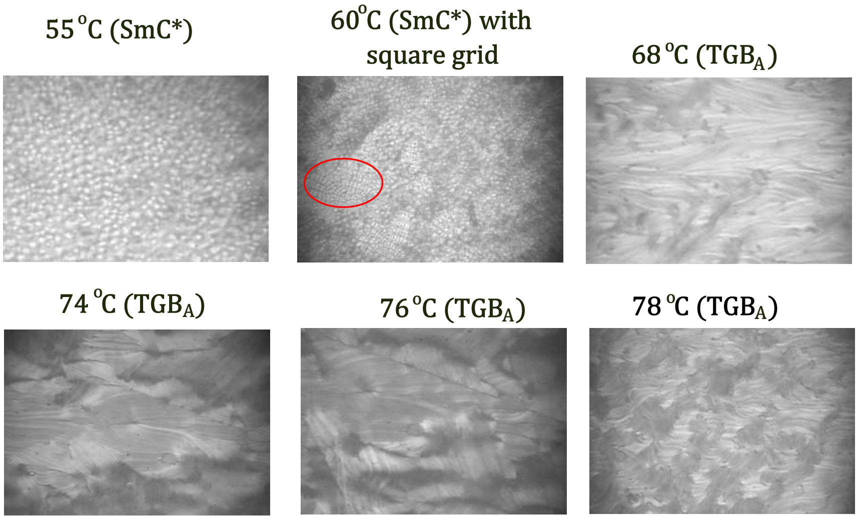

Figure 3.5: The simultaneous rheomicroscopy images are taken during the measurement of temperature dependant shear viscosity at a constant shear rate 100 s^{-1}. The red circle shows the square grid patterns in the $UTGB_{C^*}$ phase.

We performed the simultaneous rheomicroscopy observations during the measurement of temperature dependant shear viscosity at a constant shear rate $\dot{\gamma}$=100 s^{-1}. The images are shown in the Fig. 3.5. It shows a typical SmC^* texture (unaligned) at 55°C. Some patches of square grid patterns are observed at 60°C indicating $UTGB_{C^*}$ phase. Again increasing the temperatures, we observed the textures similar to the Grandjean orientation at planar anchoring conditions [15]. These are characteristics of TGB_A phase, shown in the Fig 3.5 (at 68°C, 74°C, 76°C and 78°C). The TGB_A phase shows different textures at different temperatures, which is probably due to the rapid increase in the pitch value.

We performed shear rate dependent shear stress measurements to obtain the apparent yield stress for relative comparison of the different phases of the sample [16–18]. Fig. 3.6 shows the shear rate dependent effective shear stress (σ_{eff}) at different temperatures.

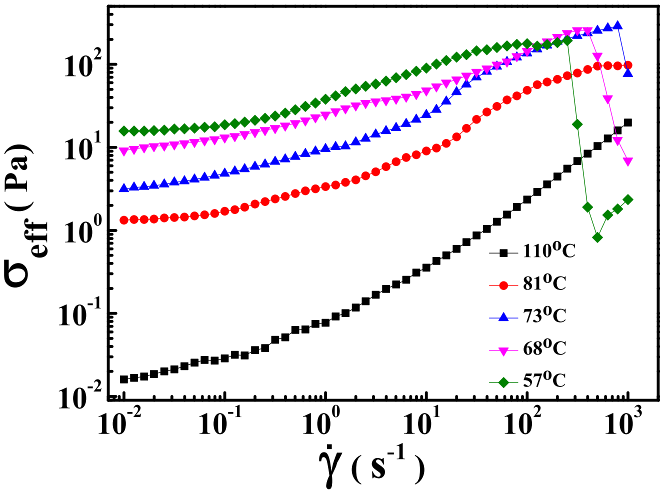

Figure 3.6: Shear rate dependent effective shear stress (σ_{eff}) at different temperatures N^*: [110^{o}C (squares)], near N^*-TGB_A transition: [81^{o}C (circles)], TGB_A: [73^{o}C (uptriangles)], TGB_A: [68^{o}C (downtriangles)], SmC^*: [57^{o}C (diamonds.]

peratures. At the low shear rate ($\dot{\gamma} < 0.1\ s^{-1}$), the stress tends to reach almost a constant value as $\dot{\gamma} \rightarrow 0$, showing an apparent yield stress (σ_y). At 110°C (N^*), σ_y is negligibly small ($\sigma_y \simeq 10^{-2}$ Pa) and it increases as the temperature is lowered in the TGB_A and SmC^* phases. For example, at 68°C (TGB_A), $\sigma_y \simeq 10$ Pa and it further increases to about 20 Pa as the temperature is decreased to SmC^* (57°C) phase. Very small σ_y in the N^* phase is due to the residual oily-streak defect network of the presheared sample. Here σ_y is three orders of magnitude larger in TGB_A than that of N^* phase. The apparent yield stress measurement have also been reported in many other smectic liquid crystals [19, 20]. However, the apparent yield stress of the TGB_A and the SmC^* phases of the present system is much larger than that known for low molecular weight smectic liquid crystals [19, 21]. The N^* phase shows shear thinning followed by a Newtonian behavior at high shear rates (>10 s^{-1}). In the intermediate shear rate range, i.e., $0.1 < \dot{\gamma} < 100\ s^{-1}$, it shows shear thinning behavior in all the phases. The shear rate dependent viscosity of nematic or cholesteric liquid crystals is usually characterized by the Ericksen number [22], which is given by the ratio of the flow-induced viscous stress ($\eta\dot{\gamma}$) to the Frank stress (K/h^2), where K is the average curvature elastic constant and h is the length scale of the flow geometry. Theoretically it has been shown that in the intermediate range of the Ericksen number (10 to 400), usually the shear viscosity shows a shear thinning behavior [23]. Assuming a typical average value of curvature elastic constant $K \sim 10^{-11}$ N and apparent viscosity of the N^* phase $\eta \simeq 10$ mPa s, the estimated Ericksen number is $\simeq$ 300, which is in the theoretically predicted range. At very high shear rate ($\dot{\gamma} > 100\ s^{-1}$), σ_{eff} in both the TGB_A and SmC^* phases fall suddenly to a much lower value. This sudden decrease could be due to the wall slip or the plastic deformation of the sample.

3.3.3 Oscillatory measurements

To determine the linear regime of viscoelasticity, we measured the strain amplitude dependence of storage ($G^{'}$) and loss ($G^{''}$) moduli at various temperatures. The measurement is performed every time on a fresh sample and the results are shown in Fig. 3.7.

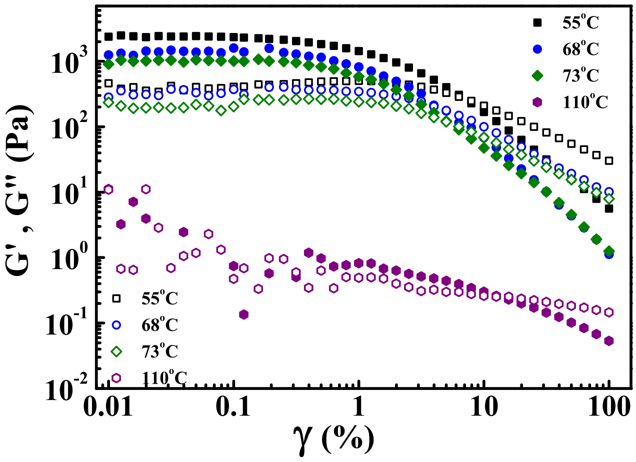

Figure 3.7: The strain amplitude dependence of the storage $G^{'}$ (solid symbols) and the loss $G^{''}$(open symbols) moduli at different temperatures. 110°C (hexagons) [N^*], 73°C (diamonds) [TGB_A], 68°C (circles) [TGB_A], and 59°C (squares) [SmC^*] at $\omega =$ 1 rad/s.]

The data in the N^* phase (110°C) at low strain amplitude are noisy due to the lower limit of the $G^{'}$ and $G^{''}$ values which our rheometer can reproducibly measure. In the TGB_A phase, (73°C and 68°C) in the linear viscoelastic region $G^{'} > G^{''}$ and $G^{'}$ of TGB_A is more than 1000 times larger than that of the N^* phase. Similarly, in the SmC^* phase (55°C), $G^{'} > G^{''}$ and $G^{'}$ is about 2.5 times larger than that of the TGB_A phase. The viscoelasticity of the N^* phase is mostly contributed by the three-dimensional network of residual oily-streak defects [2]. The SmA liquid crystals have a larger viscoelastic response than nematic or N^* merely because of the positional order. For example, in our previous studies, in cholesterol nonanoate (exhibits N^* to the SmA transition), we found $G^{'}_{SmA} \approx 80\ G^{'}_{N^*}$ [24]. In the present sample, we found $G^{'}_{TGB_A} \approx 1000\ G^{'}_{N^*}$. Hence, the enhanced elasticity of the TGB_A phase can be attributed to the structural defects present in the system. In this phase the enhancement in the viscoelasticity may also be due to the energy cost for the deformation of grain boundaries. In addition, the surface tension of the smectic layers which acts against the deformation plays a vital role for increasing the shear modulus. In the SmC^* phase, there is no grain boundary, however, the individual dislocations and their motions contribute to the viscoelastic properties. In fact, it has been suggested that the shear modulus is strongly influenced by the line tension of screw dislocations because it acts against the Peach-Koehler force which controls the motion of the dislocations [25]. When the force exerted on the dislocations dominates over the line tension, then the system overcomes its elastic deformation and undergoes plastic deformation. The drastic fall of σ_{eff} shown in Fig. 3.6 for both the TGB_A and SmC^* phases could be due to the plastic deformation. The role of defects and disorder on the viscoelasticity of randomly oriented type-I smectic liquid crystals has been discussed by many authors [1, 3, 25–31]. In those experiments, the defects were either stabilized by quenched disorder or by dispersing colloidal particles in the samples. The storage modulus of such systems show a power-law behavior [2, 3]

$$G'(\omega) = G_{\circ} + \beta\omega^{\alpha} \tag{3.1}$$

where $G_{\circ}$ is the plateau modulus arising from the zero frequency shear modulus. In the present sample, TGB_A is composed of rotating SmA blocks, which creates grain boundaries. These defects are inherent to the structure and cannot be removed by the effect of shear. Here we analyze the dynamic response of our sample based on the power-law model (Eq. 3.1).

Figure 3.8 shows some representative frequency dependence of storage and loss moduli in all the phases. In the N^* phase, $G^{'} > G^{''}$, and at the low frequency region (ω

≤ 2 rad/s) both are constant. They increase with frequency beyond this range. For example, beyond $\omega \geq 2$ rad/s they vary as $G^{'} \sim \omega^2$ and $G^{''} \sim \omega$. It may be mentioned that solid-like behavior in the low frequency region ($\omega = 1$ rad/s) was also observed in colloidal-particle-dispersed cholesteric liquid crystals. But at higher frequency the same sample showed fluid-like behavior ($G^{'} < G^{''}$) [2]. The fit parameters obtained from different phases are shown in Fig. 3.9(a). In the N^* phase (90° to 110°), α obtained from both the $G^{'}$ and $G^{''}$ data are almost close to 2 and 1, respectively. It is interesting to note that the exponent α obtained from both the fittings of $G^{'}$ and $G^{''}$ decreases rapidly (below 90°C) and is almost equal, i.e. $\alpha \simeq 0.5$. Ramos *et al.* [2]

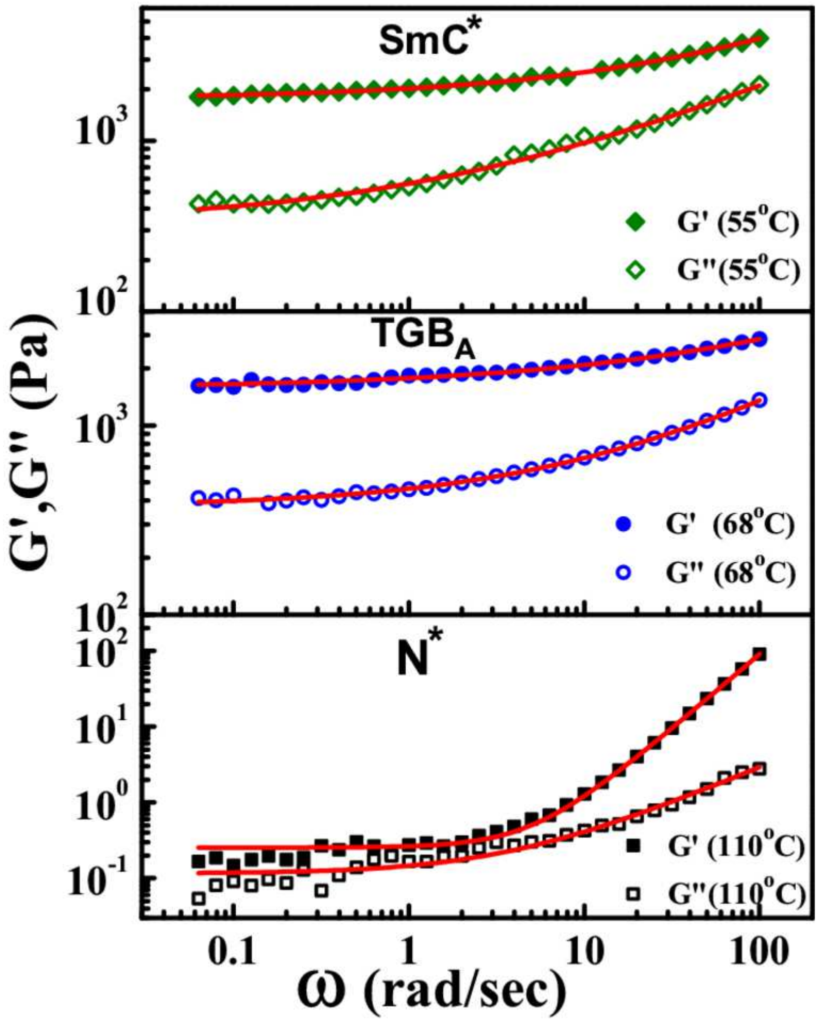

Figure 3.8: The frequency dependence of (a) storage $G^{'}$ (solid symbols) and (b) loss $G^{''}$ (open symbols) moduli at three representative temperatures in all the phases. The solid lines are best fits to Eq. (3.1).

showed that the storage modulus of liquid crystalline systems with a defect network has contributions both from the disoriented part of the sample, $G^{'}(\omega) \propto \omega^{1/2}$ and regions of the sample where the layers are parallel to the shear direction $G^{'}(\omega) \propto \omega^{2}$. Similarly, the loss modulus also has contribution from disoriented parts of the sample, $G^{''}(\omega) \propto \omega^{1/2}$ and a Maxwell fluid type contribution $G^{'}(\omega) \propto \omega$. Comparing to our results, it appears that the storage and loss moduli of TGB_A phase have a significant contribution from the disoriented layers of the sample only.

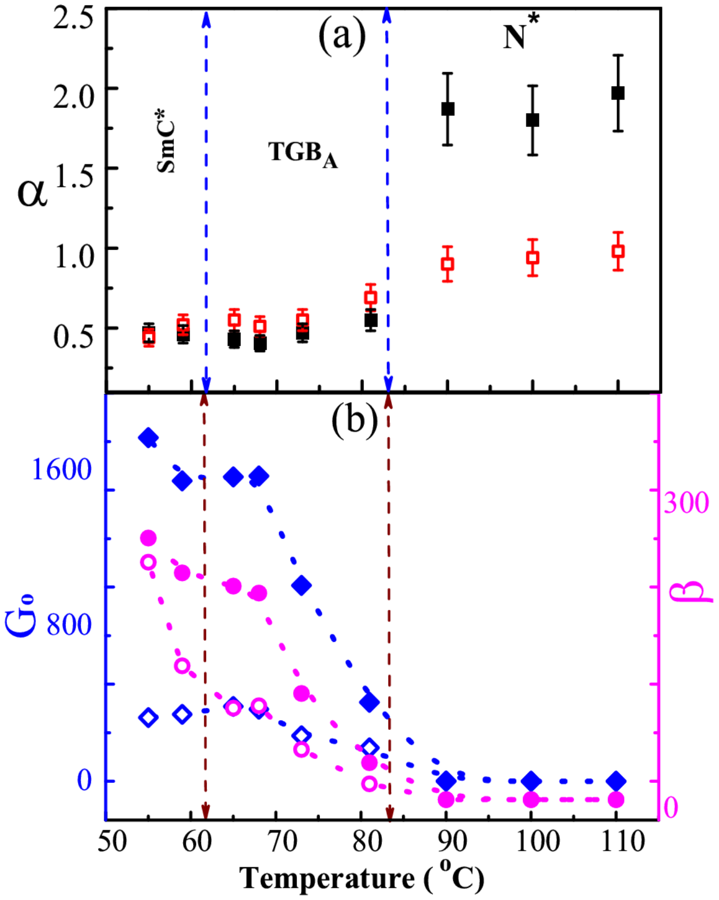

Figure 3.9: (a) The exponent α characterizing the power-law contribution to $G^{'}(\omega)$(solid squares) and $G^{''}(\omega)$ (open squares) as a function of temperature. (b) Temperature variation of fit parameters, $G_{\circ}$ and β obtained from the fitting of $G^{'}(\omega)$ and $G^{''}(\omega)$ data. Diamonds (solid and open) and circles (solid and open) are obtained from $G^{'}(\omega)$ and $G^{''}(\omega)$ data respectively.

The temperature dependence of $G_{\circ}$ and β obtained from the fitting of $G^{'}(\omega)$ and $G^{''}(\omega)$ is also shown in Fig. 3.9(b). For example, at 110°C, $G_{\circ}$ obtained from both the fits are 0.25 and 0.12 respectively. At the same temperature, β values are 0.01 and 0.03 respectively, and similar values were also reported in other cholesteric samples [2]. The plateau modulus ($G_\circ$) usually arises from the elasticity of static defects in lamellar systems [2, 3]. In the present system $G_\circ$ is much larger ($\simeq$ 10 times) than the low molecular weight thermotropic SmA liquid crystal, such as 8CB [3].

The variation of $G_\circ$ with reduced temperature $\chi \equiv (T_{N^*-TGB_A}\text{-}T\ )/T_{N^*-TGB_A}$ is shown in Fig. 3.10. In the TGB_A and SmC^* phases, $G_\circ$ is more than three orders of magnitude larger than the N^* phase [2]. In analogy with rubber elasticity, the contribution to the elastic response of static defect network varies as $G_\circ \approx \tau/d^2$, where τ is the line tension and d is a typical average spacing between defects [2]. In case of screw dislocations the defect line tension can be written as $\tau = Bb^4/128\pi^3 r_c^2$, where B is the layer compression modulus, $b = md_\circ$ is the Burger's vector of integer strength m and r_c is the defect core radius [32]. Measurements on many smectic systems show that $B \sim \chi^{0.4}$ [33] and $r_c^{-2} \sim \psi^2 \sim \chi^{0.5}$, where ψ is the smectic order parameter [34]. Hence the defect line tension (τ) can be defined as, $\tau \sim \chi^{0.9}$, which implies $G_\circ \sim \chi^\gamma$ with $\gamma \approx 0.9$. It suggests the defects significantly contribute to the shear response [34]. In analogy with this theoretical calculation we have fitted χ dependent $G_\circ$ values with respect to the equation $G_\circ \simeq \chi^\gamma$ (Fig. 3.10), which shows the fitting parameter $\gamma = 1$. It is comparable with the theoretical calculation, suggesting the screw dislocations notably contribute to the shear response . Assuming a moderate

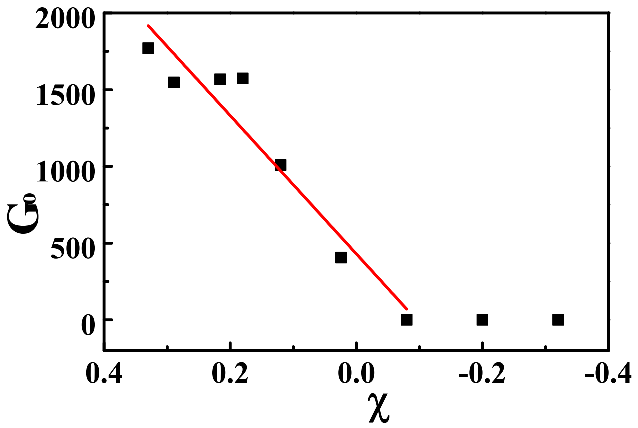

Figure 3.10: The variation of $G_\circ$ with reduced temperature χ. The solid line showing the best-fit result $G_\circ \simeq \chi^\gamma$, with $\gamma = 1$

value of Berger's vector of integer strength m=2 [35], B $\approx 2 \times 10^6$ Pa [3,33] and using the relation $G_\circ \approx \tau/d^2$, we got $d \approx 26$ nm in the TGB_A phase. This is comparable with the experimentally measured dislocation spacing in TGB_A phase [9]. In the lamellar phase, the parameter β, that determines the strength of bulk response is given by $\beta = (\pi/24\sqrt{2} \times \sqrt{(B\eta)})$, where η is the effective viscosity [2]. Taking $\beta \simeq 300$ (at 68°C), the calculated viscosity in the TGB_A phase is $\eta \simeq 10^3$ mPa s, which is close to the experimentally measured value (in Fig. 3.4). We noticed that the exponent α in the TGB_A phase is $\simeq 0.5$, and further it tends to decrease in the SmC^* phase (Fig. 3.9(a)). This is somewhat less than that of the lamellar block copolymer ($\alpha = 0.6$) [36]. Within the soft glass rheology model, the glass transition is characterized from the power-law exponent $G^{'} \sim \omega^{x-1}$. In this model, "x" is an effective noise temperature and in the range of $1 < x < 2$ and $G^{''}$ and $G^{'}$ have a constant ratio [37]. The system approaches the glass transition as $x \rightarrow 1$, i.e., $\alpha = (x-1) \rightarrow 0$. In the N^* phase, α obtained from the fitting of $G^{'}$ and $G^{''}$ is very different and it decreases with decreasing temperature and merges to ($\simeq 0.5$) upon entering the TGB_A and SmC^* phases. Though the TGB_A and SmC^* phases are thermodynamically stable and the experimental value of x is about 1.5, indicating that their rheological responses are similar to many soft glassy materials.

3.4 Conclusion

We studied the rheology of a binary mixture showing a large temperature range of the TGB_A phase. All the phases in the mixture, i.e., N^*, TGB_A, and SmC^* exhibit solid-like behavior. The elasticity of the TGB_A phase is discussed based on the theory of lamellar systems that accounts for the contribution of defects. The power-law dependence of the complex shear modulus and the analysis of the experimental results suggest that the enhanced elasticity of the TGB_A phase is due to the structural defects. The effective noise temperature approaches 1, suggesting TGB_A liquid crystals and its low temperature phases are a defect-mediated soft solid whose dynamics is similar to soft glassy materials.

References

[1] G. Basappa, Suneel, V. Kumaran, P. R. Nott, S. Ramaswamy, V. M. Naik, and D. Rout. *Structure and rheology of the defect-gel states of pure and particle-dispersed lyotropic lamellar phases.* Eur. Phys. J. B, vol. 12, pp. 269-276, 1999.

[2] L. Ramos, M. Zapotocky, T. C. Lubensky, and D. A. Weitz. *Rheology of defect networks in cholesteric liquid crystals.* Phys. Rev. E, vol. 66, p. 031711, 2002.

[3] R. Bandyopadhyay, D. Liang, R. H. Colby, J. L. Harden, and Robert L. Leheny. *Enhanced elasticity and soft glassy rheology of a smectic in a random porous environment.* Phys. Rev. Lett., vol. 94, p. 107801, 2005.

[4] T. A. Wood, J. S. Lintuvuori, A. B. Schofield, D. Marenduzzo, and W. C. K. Poon. *A self-quenched defect glass in a colloid-nematic liquid crystal composite.* Science, vol. 334, no. 6052, pp. 79-83, 2011.

[5] P. G. de Gennes. *The Physics of Liquid Crystals.* Oxford University Press, Oxford, 2nd ed., 1993.

[6] S. R. Renn and T. C. Lubensky. *Abrikosov dislocation lattice in a model of the cholesteric-to-smectic-A transition.* Phys. Rev. A, vol. 38, no. 4, pp. 2132-2147, 1988.

[7] P.M. Chaikin and T. C. Lubensky. *Principle of condensed matter physics.* Cambridge University Press, Cambridge, England, 1995.

[8] J. W. Goodby, M. A. Waugh, S. M. Stein, E. Chin, R. Pindak, and J. S. Patel. *Characterization of a new helical smectic liquid crystal.* Nature, vol. 337, pp. 449 - 452, 1989.

[9] L. Navailles, B. Pansu, L. Gorre-Talini, and H. T. Nguyen. *Structural study of a commensurate* TGB_A *Phase and of a presumed chiral line liquid phase*. Phys. Rev. Lett., vol. 81, no. 19, pp. 4168-4171, 1998.

[10] L. Navailles, R. Pindak, P. Barois, and H. T. Nguyen. *Structural study of the smectic-C twist grain boundary phase*. Phys. Rev. Lett., vol. 74, no. 26, pp. 5224-5227, 1995.

[11] N. Isaert, L. Navailles, P. Barois, and H. T. Nguyen. *Optical evidence of the layered array of grain boundaries in* TGB_A *and* TGB_C *mesophases*. J. Phys. II France, vol. 4, no. 9, pp. 1501-1518, 1994.

[12] P. A. Pramod, R. Pratibha, and N. V. Madhusudana. *A three-dimensionally modulated structure in a chiral smectic-C liquid crystal*, Current Science, vol. 73, no. 9, pp. 761-765, 1997.

[13] P. A. Pramod, R. Pratibha, S.R.Warrier, and N.V. Madhusudana. *Experimental studies on the undulated twist grain boundary-* C^* *liquid crystal*. Ferroelectrics, vol. 244, no. 1, pp. 31-38, 2000.

[14] S. Dhara, R. Pratibha, and N. V. Madhusudana. *Some experimental investigations on type II chiral liquid crystals*. Ferroelectrics, vol. 277, no. 1, pp. 13-23, 2002.

[15] I. Dierking. *Textures of liquid crystals*. Wiley-VCH verlag GmbH and Co. Weinheim, 2003.

[16] D. De Kee and R. P. Chhabra. *Elastic modulus and yield stress of suspensions*. Rheol. Acta, vol. 33, pp. 238-240, 1994.

[17] M. Singh, V. Agarwal, D. De Kee, G. McPherson, V. John, and A. Bose. *Shear-induced orientation of a rigid surfactant mesophase*. Langmuir, vol. 20, pp. 5693-5702, 2004.

[18] M. H. Zhang, C. F. Ferraris, H. Zhu, V. Picandet, M. A. Peltz, P. Stutzman, and D. De Kee. *Measurement of yield stress for concentrated suspensions using a plate device*. Materials and Structures, vol. 43, pp. 47-62, 2010.

[19] L. L. Chapoy and R. W. Duke. *Some anomalous rheological responses of thermotropic liquid crystals*. Rheol. Acta, vol. 18, pp. 537 - 544, 1979.

[20] S. Paasch, F. Schambil, and M. J. Schwuger. *Rheological properties of lamellar lyotropic liquid crystals*. Langmuir, vol. 5, pp. 1344-1346, 1989.

[21] S. Asnacios, C. Meyer, Y. A. Nastishin, M. Kleman, and J. Malthene. *Rheological properties of chiral liquid crystals possessing a cholesteric-smectic A transition*. Liquid Crystals, vol. 31, no. 4, pp. 593–599, 2004.

[22] Ronald G. Larson. *The Structure and Rheology of Complex Fluids*. Oxford University Press, New York , 1999.

[23] D. Grecov and A. D. Rey. *Steady state and transient rheological behavior of mesophase pitch, Part II: Theory*. J. Rheol., vol. 49, no. 1, pp. 175-195, 2005.

[24] M. Rajeswari, J. Ananthaiah, R. Dabrowski, V. S. S. Sastry, S. Dhara, and B. K. Sadashiva. *Rheological properties of a chiral liquid crystal exhibiting type-II character*. Mol. Cryst. Liq. Cryst, vol. 547, no. 1, pp. 39-45, 2011.

[25] S. Fujii, S. Komura, Y. Ishii, and C. Y. D. Lu. *Elasticity of smectic liquid crystals with focal conic domains*. J. Phys. Condens. Matter, vol. 23, no. 23, p. 235105, 2011.

[26] M. Zapotocky, L. Ramos, P. Poulin, T. C. Lubensky, and D. A. Weitz. *Particle-stabilized defect gel in cholesteric liquid crystals*. Science, vol. 283, no. 5399, pp. 209-212, 1999.

[27] M. Roth, M. D'Acunzi, D. Vollmer, and G. K. Auernhammer. *Viscoelastic rheology of colloid-liquid crystal composites*. J. Chem. Phys., vol. 132, p. 124702, 2010.

[28] C. Meyer, S. Asnacios, C. Bourgaux, and M. Kleman. *Rheology of lyotropic and thermotropic lamellar phases*. Rheol. Acta, vol. 39, pp. 223-233, 2000.

[29] K. Kawasaki and A. Onuki. *Dynamics and rheology of diblock copolymers quenched into microphase-separated states*. Phys. Rev. A, vol. 42, no. 6, pp. 3664(R)-3666, 1990.

[30] C. Meyer, S. Asnacios, and M. Kleman. *Universal properties of lamellar systems under weak shear*. Eur. Phys. J. E, vol. 6, pp. 245-253, 2001.

[31] L. Rogerio, P. A. Lima, and A. D. Rey. *Linear viscoelasticity of textured carbonaceous mesophases*. J. Braz. Chem. Soc., vol. 17, no. 6, pp. 1109-1116, 2006.

[32] M. Kleman. *Defects in liquid crystals*. Rep. Prog. Phys., vol. 52, no. 5, pp. 555-654, 1989.

[33] M. Benzekri, J. P. Marcerou, H. T. Nguyen, and J. C. Rouillon. *Critical behavior of the layer compressional elastic constant* B *at the smectic-*A *- nematic phase transition*. Phys. Rev. B, vol. 41, no. 13, pp. 9032-9037, 1990.

[34] R. L. Leheny, S. Park, R. J. Birgeneau, J. L. Gallani, C. W. Garland, and G. S. Iannacchione. *Smectic ordering in liquid-crystal-aerosil dispersions. I. X-ray scattering*. Phys. Rev. E, vol. 67, p. 011708, 2003.

[35] R. D. Kamien and T. C. Lubensky. *Minimal surfaces, screw Dislocations and twist grain boundaries*. Phys. Rev. Lett., vol. 82, pp. 2892-2895, 1999.

[36] R. G. Larson, K. I. Winey, S. S. Patel, H. Watanabe, and R. Bruinsma. *The rheology of layered liquids: lamellar block copolymers and smectic liquid crystals*. Rheol. Acta, vol. 32, no. 3, pp. 245-253, 1993.

[37] P. Sollich, F. Lequeux, P. Hebraud, and M. E. Cates. *Rheology of soft glassy materials*. Phys. Rev. Lett., vol. 78, no. 10, pp. 2020-2023, 1997.

4

Experimental studies on the rheology of cubic blue phases

4.1 Introduction

In the previous chapter we have studied the rheological properties of TGB_A liquid crystals. In this chapter we study the rheology of another frustrated phase of liquid crystals namely the blue phase. In this case the lattice of disclination defects stabilise its structure.

Blue phases (BPs) are distinct thermodynamic phases, exist within a narrow range of temperature ($\sim 1\ K$) in highly chiral liquid crystals. This phase was first observed by Friedrich Reinitzer in 1888 on the melting behaviour of cholesteryl benzoate and he noted that the substance turned to blue and formed a cloudy state upon cooling [1]. This specific state of the liquid crystalline phase remained unexplored for a long time. Later the discovery of polymer stabilised blue phase with wide temperature range has been created immense interest in the scientific community [2–10]. Based on the structure, blue phases are categorised as BP-I, BP-II and BP-III. The BP-III has an amorphous structure, so its symmetry is same as that of the isotropic phase. Hence it's often quite hard to identify under polarising microscope, because it looks like foggy. BP-II shows simple cubic structure where BP-I shows body-centered cubic structure. The detailed structure of two blue phases (BP-I and BP-II) have been discussed in chapter-1. BP-II and BP-I can be detected and identified under polarising microscope. BP-II is generally observed over a certain range of chirality regime, and it vanishes in the high chirality regime, whereas the stability of BP-I increases with increasing chirality.

Significant progress has been made in understanding the complex structure of blue phases. Still many fundamental aspects of these exotic phases are unexplored. For example, recently several predictions were made on the rheological properties and the dynamics of the disinclination networks of BP-I and BP-II [11–13]. However experimentally very little is known about the rheological properties of these phases [14–16]. In this chapter, we discuss the first detailed experimental studies on the rheology of cubic blue phases. Our results show that different rheological responses of BP-II and BP-I are connected to their structures and the dynamics of the defect networks.

4.2 Experimental

The blue phase liquid crystal, we used in this study is a mixture of four fluorinated compounds and a highly chiral dopant. These compounds were synthesized by our collaborators in Poland. They are chemically stable and exhibit high resistivity [17]. The detailed molecular structure and the wt% of the individual components in the mixture are given below in Fig 4.1. It exhibits following phase transitions: I 46.4°C BP-II 41.4°C BP-I 36.6°C N*. We performed rheological measurements by using stress-controlled rheometer with a cone-plate measuring system having a plate diameter of 25 mm and a cone angle of 1°. The temperature of the sample was controlled with an accuracy of 0.1°C. We used rheo-microscopy setup to observe the microstructures under shear. The details about this setup are explained in the chapter-1.

4.3 Results and discussion

First we observed the textures of various phases of our sample under polarised optical microscope in a planar cell. Fig. 4.2(a) and (b) show BP-II and BP-I phases respectively and Fig. 4.2(c) shows the cholesteric (N^*) phase having oily-streak defect

Chemical structure	Compounds	Concentration
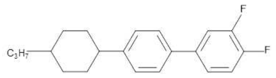	4'-(trans-4-Propylcyclohexyl)-3,4-difluorobiphenyl	19%
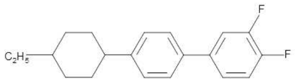	4'-(trans-4-ethylcyclohexyl)-3,4-difluorobiphenyl	19%
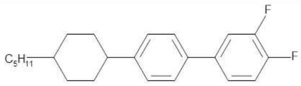	4'-(trans-4-pentylcyclohexyl)-3,4-difluorobiphenyl	38%
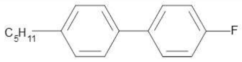	4’-pentyl-4-fluorobiphenyl	4%
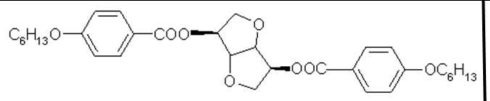	3,6-bis-(4-hexyloxybenzoyl) isomannide	20%

Figure 4.1: The chemical structure and the wt% of individual compounds in the mixture, that shows blue phases.

network. The bulk sample was mounted on the rheometer without any surface treatment of the measuring plates. We made all the measurements on cooling the sample from the isotropic phase. To identify the phase transition temperatures in the rheometer, we first measured the temperature dependent shear stress at a fixed shear rate (Fig. 4.3). The isotropic (I) to BP-II phase transition is marked by a rapid increase of the stress and the BP-I to cholesteric phase (N^*) transition is marked by a sudden fall of the same. We observed a small kink at the BP-II to BP-I phase transition. The temperature range of BP-II and BP-I is 5°C and 4.8°C, respectively. The stress in the N^* is almost comparable to that of the isotropic phase except a gradual increase due to the decrease of temperature. We observed that the shear stress of BP-I is larger

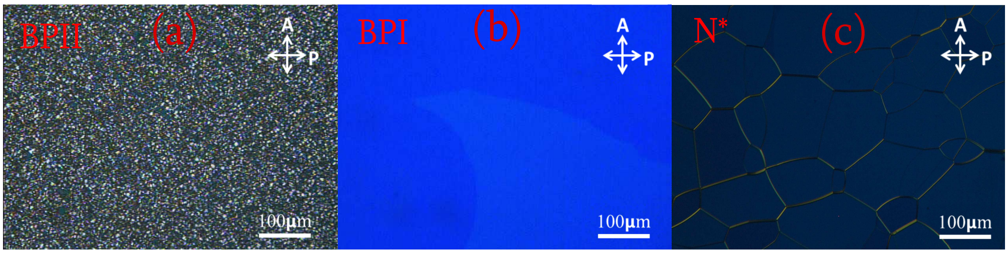

Figure 4.2: The textures of BP-II, BP-I and cholesteric (N^*) phase observed under optical polarising microscope.

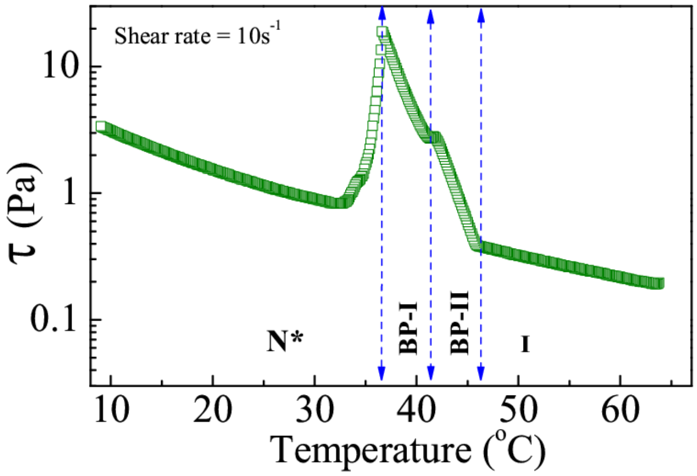

Figure 4.3: Temperature dependent shear stress at a constant shear rate (10 s^{-1}). Three different phase transitions are marked by dotted vertical lines.

than that of the BP-II and N^* phase.

Fig. 4.4 shows some representative rheomicroscopy images which were taken during the measurement of temperature dependent shear stress at a constant shear rate. In BP-II, we observed the Grandjean-cano lines which are oriented perpendicular to the shear direction (Fig. 4.4(a)). It suggests that the director is aligned parallel to the shear direction. The increase of shear stress compared to the isotropic phase is due to the motion of these Grandjean-cano lines. As the temperature is reduced, some filamentary structures appear in BP-I (Fig. 4.4(b)) and the stress is also increased compared to BP-II. These filamentary structures are continuously broken and rejoined during the steady shear. The cholesteric phase shows a typical texture (Fig. 4.4(c) and (d)) similar to that usually observed under planar degenerate surface anchoring conditions.

In Fig. 4.5 the shear rate dependent viscosity is shown. We observed that the N^* phase exhibits a typical shear thinning behavior. The viscosities of BP-II and BP-I phases are much larger than that of the N^* phase in the low shear rate regime (0.01 to 1 s^{-1}). For example, at $\dot{\gamma} = 0.01\ s^{-1}$, $\eta_{N^*} = 1.2$ Pa s, $\eta_{BP-II} = 17$ Pa s and $\eta_{BP-I} = 52$ Pa s. BP-I and BP-II show multiple shear thinning behavior and the slope of η changes at different $\dot{\gamma}$. The viscosity of BP-II at the highest shear rate is lower than that of

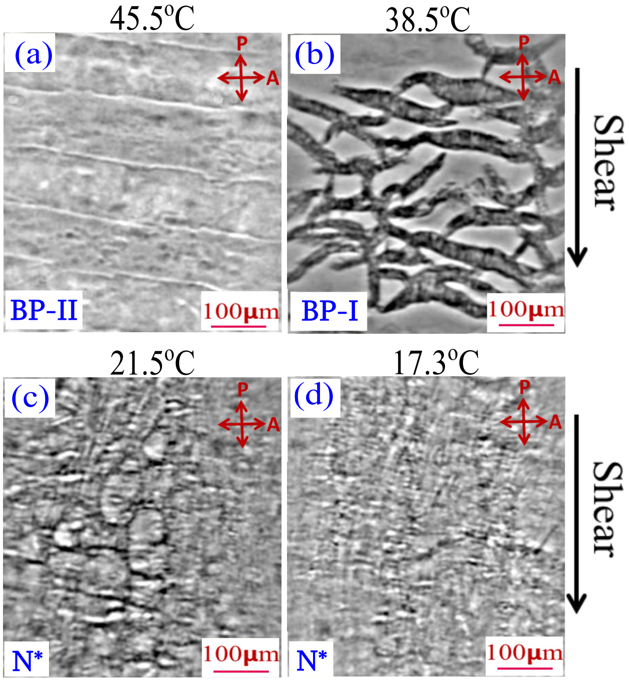

Figure 4.4: Optical rheomicroscopy images taken during the measurement of temperature dependent shear stress at a constant shear rate of 10 s^{-1} in three different phases. The direction of shear is shown by an arrow. P and A indicate polariser and analyser.

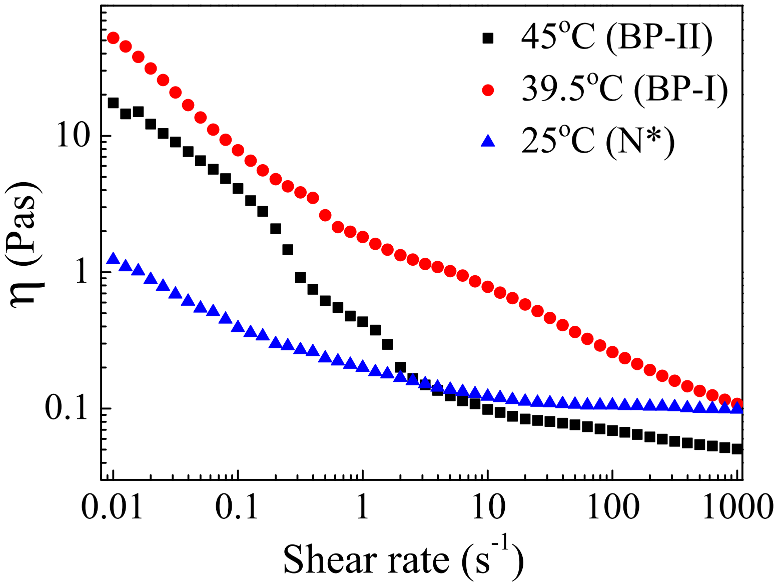

Figure 4.5: Shear rate dependent viscosity at three different temperatures representing BP-II, BP-I and N^* phases.

the N^* phase. Thus BP-II shows stronger shear thinning behavior than the other two phases. Further we have also estimated the approximate Ericksen number (E_r) of the three phases, where the elastic constant (K) of BP is in the order of 10^{-11} N. The range of Ericksen numbers of the N^* phase is $30 < Er < 9 \times 10^4$ where the shear rate ($\dot{\gamma}$) varies from 0.01 to 1000 s^{-1}. Similarly for the BP-II and BP-I, the ranges of Ericksen number are $50 < Er < 7 \times 10^4$ and $300 < Er < 1.2 \times 10^5$ respectively. The large Ericksen number in the BP-I signifies that the shear viscosity is larger than the Frank elastic energy which could be due to the filamentary microstructures observed in the Fig. 4.4(b).

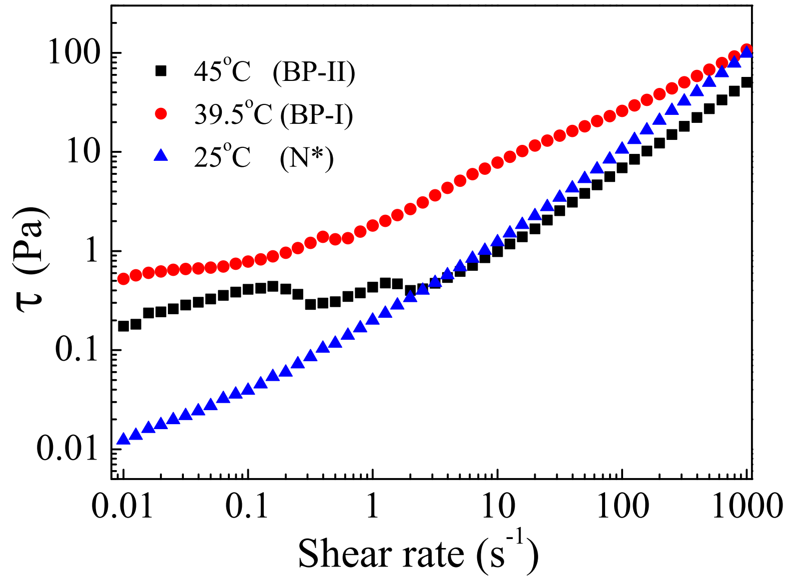

Figure 4.6: Shear rate dependent shear stress at three different temperatures representing BP-II, BP-I and N^* phases.

The variation of shear stresses with respect to shear rate of three phases is shown in Fig. 4.6. Shear stress of BP-II shows three distinct regimes namely BP-II(1): $\dot{\gamma}$ = 0.01–0.3 s^{-1}: BP-II(2): $\dot{\gamma}$ = 0.3–2 s^{-1} and BP-II(3): $\dot{\gamma}$ = 2–1000 s^{-1}. A power law fit $\tau = a\dot{\gamma}^{\alpha}$ (Fig. 4.7) describes the data to a very good approximation. The fit parameters are: $a = 0.87$ and $\alpha = 0.33$ in BP-II(1); $a = 0.42$ and $\alpha = 0.35$ in BP-II(2); $a = 0.12$ and $\alpha = 0.87$ in BP-II(3).

Some representative rheomicroscopy images in three different shear rate ranges are also shown in Fig. 4.8. We observed that in BP-II (0.01 – 0.3 s^{-1}), the Grandjean-cano

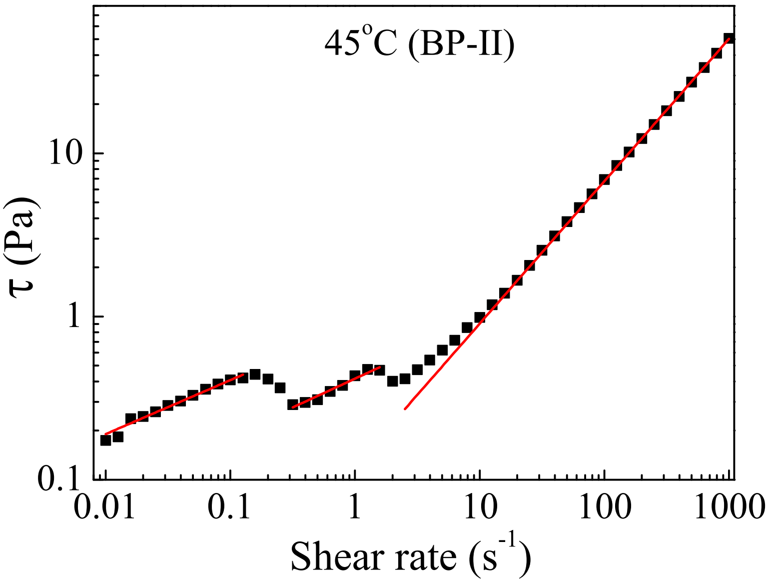

Figure 4.7: Shear rate dependent shear stress at 45°C (BP-II). Red lines are best fits to the power law: $\tau = a\dot{\gamma}^{\alpha}$.

lines flow parallel to the shear direction (downward green arrows in BP-II, Fig. 4.8). In BP-II (0.3 – 2 s^{-1}), the Grandjean-cano lines are broken and in BP-II (2 – 1000 s^{-1}), the texture appears like a flow aligned nematic phase. In BP-I, there are also several regimes observed but they are not distinctly separable as that of BP-II. Nevertheless it is clear that the multiple shear thinning is due to the breaking of texture at different shear rates (BP-I in Fig. 4.8). The cholesteric phase shows uniform shear thinning behavior and there is no significant change in the textures up to the shear rate of 10 s^{-1}. Beyond this shear rate the helix uncoils and leaves a flow induced nematic phase and hence the viscosity decreases. In the case of BP-II and BP-I, the flow induced nematic state appears at shear rate above 126 s^{-1} and 200 s^{-1} respectively. Recently, Henrich *et al.* studied the rheology of cubic blue phases by numerical simulation [12]. Depending on the shear rate and the Ericksen number, various flow regimes have been identified in both BP-I and BP-II and our results qualitatively agree with their predictions as shown in the Fig. 4.9. In particular we observed this phenomena at much higher shear rate (0.01 - 1000 s^{-1}), compared to the simulation. However it may be possible to observe the similar behavior in the simulation at much higher shear rate (similar to our experiment) by appropriate choice of the parameters.

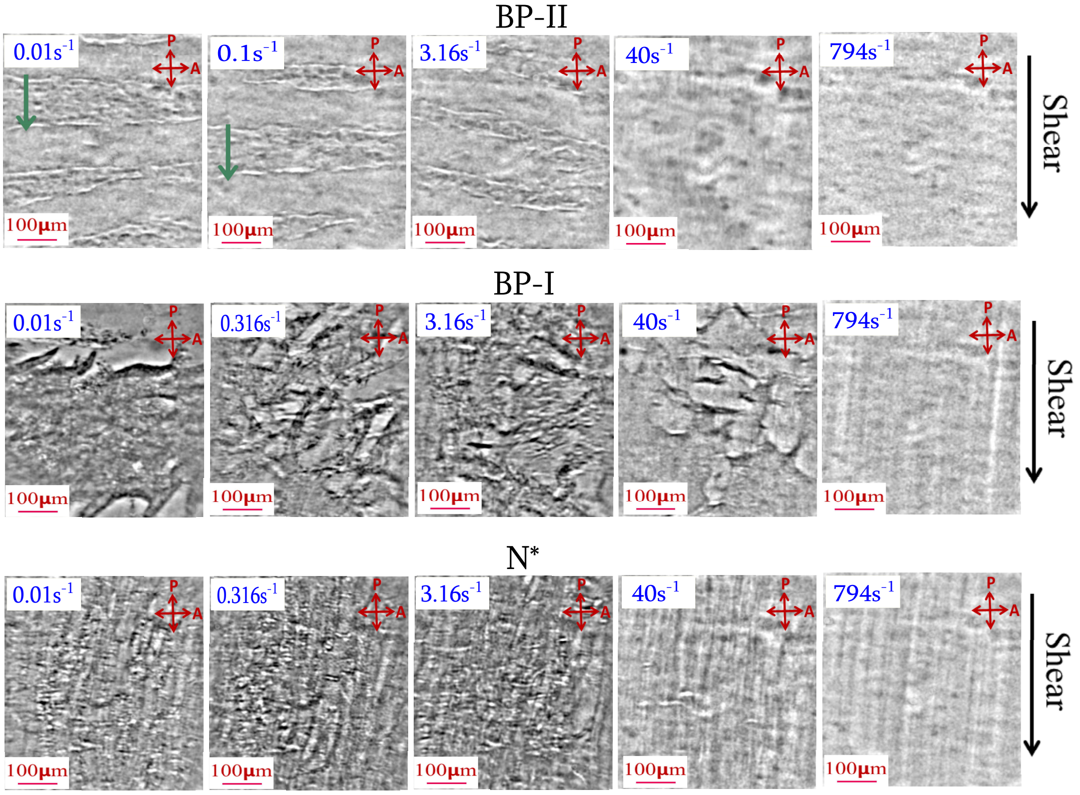

Figure 4.8: Rheomicroscopy images taken during the measurement of shear rate dependent viscosity in three phases. The direction of shear is shown by an arrow on the right side. The downward green arrows in BP-II show the motion of the Grandjean-cano lines.

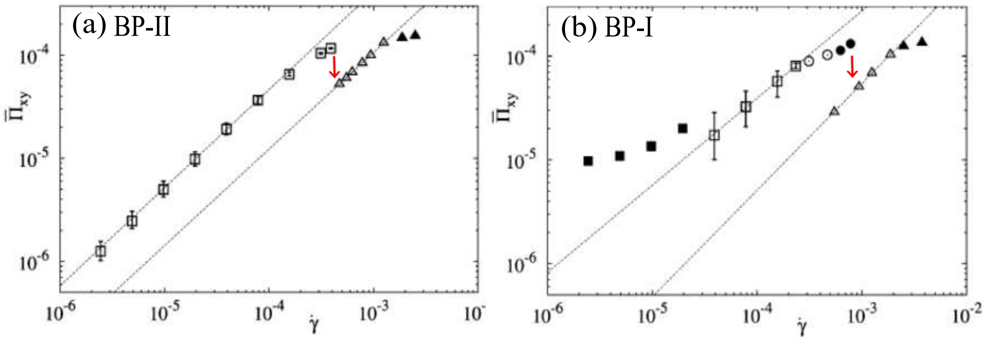

Figure 4.9: Flow curve of shear rate dependent shear stress showing various flow regimes of (a) BP-II and (b) BP-I. Above a critical shear rate the network breaks up into the Grandjean texture (open triangles) or a flow aligned nematic state at even higher shear rates (solid triangles). The red arrows indicate fall in the shear stress values. Adapted from the ref. [12]

We also performed small angle light scattering (SALS) experiments. The details of the experimental setup are explained in the chapter-2. The images of HV scattering at various shear rates are shown in Fig. 4.10. We observed that the SALS patterns of all the phases at the lowest shear rate (0.01 s^{-1}) are mostly circular with the largest diameter in the N* phase. It suggests that the orientational fluctuations are stronger in the N^* phase compared to the other two phases. Interestingly at higher shear rates (40 - 126 s^{-1}), BP-II shows obscure butterfly patterns. The butterfly patterns are prominently observed in contour plots (insets of Fig. 4.10, BP-II). These kinds of SALS patterns are typically observed in complex fluids including polymer solutions, polymer mixtures, micellar surfactants and lyotropic lamellar phases due to the density or concentration fluctuations that are moderately coupled to the flow [18,19]. However we did not observe any special feature in rheomicroscopy at the same shear rates. It suggests that the characteristic time of flow is faster than the breaking and reforming of the microstructures. At a shear rate 40 s^{-1}, BP-I shows multiple scattering patterns (Fig. 4.10, BP-I) which are very different from BP-II. This is due to the stronger orientational fluctuations caused by larger microstructures observed (Fig. 4.8, BP-I) in rheomicoscopy. At a shear rate of 40 s^{-1}, N^* shows an anisotropic scattering pattern that is elongated perpendicular to the shear direction. At a very high shear rate (e.g. 631 s^{-1}), the scattering patterns of both BP-II and N^* phases are highly elongated perpendicular to the shear direction. Since the images are in the q-space, the overall alignment of the director is along the shear direction. The scattering intensity at a higher shear rate (for example, at 631 s^{-1}) in BP-I is almost zero and this could be due to the very low birefringence and ceasing of orientational fluctuations due to the large elastic modulus.

Fig. 4.11 shows the strain dependent storage ($G^{'}$) and the loss ($G^{''}$) moduli of all the phases. We observed that in the N^* phase, in the low strain regime ($\gamma \leq 1\%$), $G^{'} \simeq G^{''}$. In the high strain regime ($\gamma > 1\%$), $G^{''}$ is larger than $G^{'}$ ($G^{''} > G^{'}$) and it shows a typical fluid-like behavior. $G^{'}$ of both the blue phases is higher than that of the N^* phase and $G^{'}$ of BP-I is around 5 times larger than that of BP-II. The linear viscoelastic (LVE) range of both the cubic phases is almost comparable (i.e., $\gamma_c = 4\%$). In BP-I, the strain induced fluidization (the crossover of $G^{'}$ and $G^{''}$) occurs at $\gamma = 16\%$ whereas in BP-II it occurs at a higher strain value ($\gamma = 20\%$) than that of BP-I.

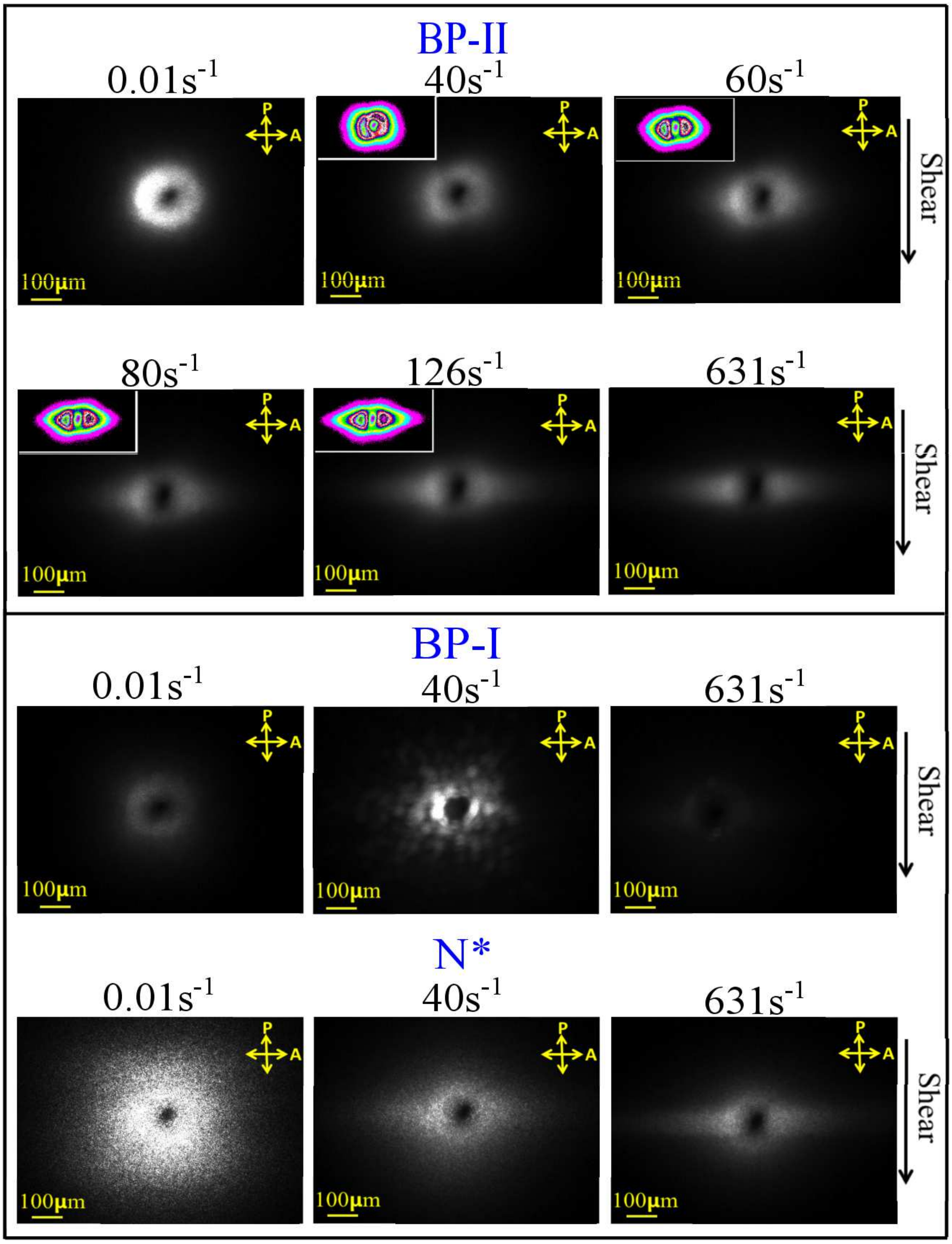

Figure 4.10: Small angle light scattering (SALS) images taken in the HV polarisation configuration at three different temperatures and various shear rates. The direction of shear is shown by an arrow. The insets are contour plots with false colours.

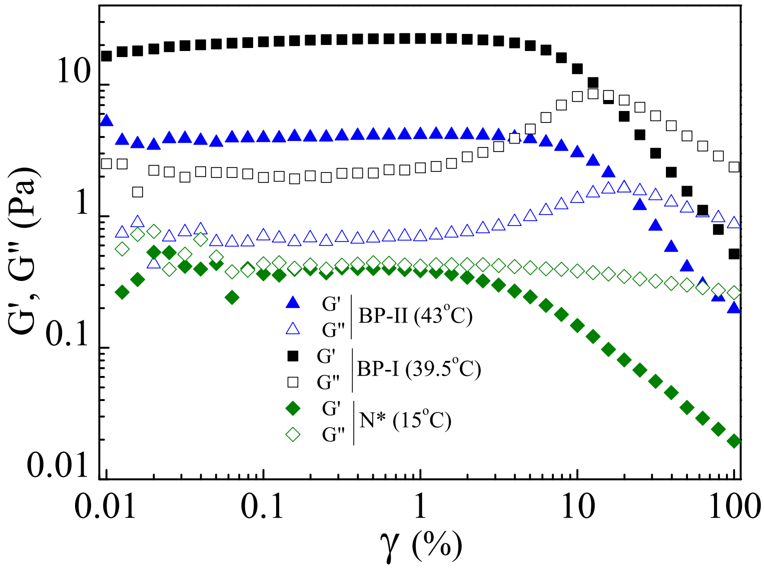

Figure 4.11: The strain dependence of the storage (G') and the loss (G'') moduli of the sample at three different temperatures where $\omega = 1$ rad s^{-1}.

This could be due to the fact that the defect lines in BP-II are intersecting and larger strain is needed to break the intersection and as a result its critical strain amplitude is higher than that of the BP-I.

To get more insight into the dynamics of the defect networks, we performed step-strain measurements. Figure 4.12 shows the stress response under applied step-strain. Here the strain value is changed from 0.3% (within LVE) to 30% (above LVE range). There are three regions in the time dependent shear stress. Initially (region-I) the strain is below the LVE range and constant for 600 s. Then the strain is increased above the LVE range (region-II) and constant for 600 s and again it is decreased to 0.3% (region-III). The N^* phase shows expected stress response under applied step-strain in all the regions. In region-II of BP-II there is a gradual decrease of stress with time and it could be due to the breaking of defect nodes under high strain followed by a continuous bulk flow. In the same region of BP-I the stress is constant where the system undergoes a flow aligned state. In this case there is no breaking of defect networks, as they do not intersect. In region-III both BP-I and BP-II show sinusoidal stress oscillations that decay with time. The amplitude of oscillation is more in BP-I than that of BP-II (Fig. 4.12, region-III). The periodic modulation in the BP-I, in

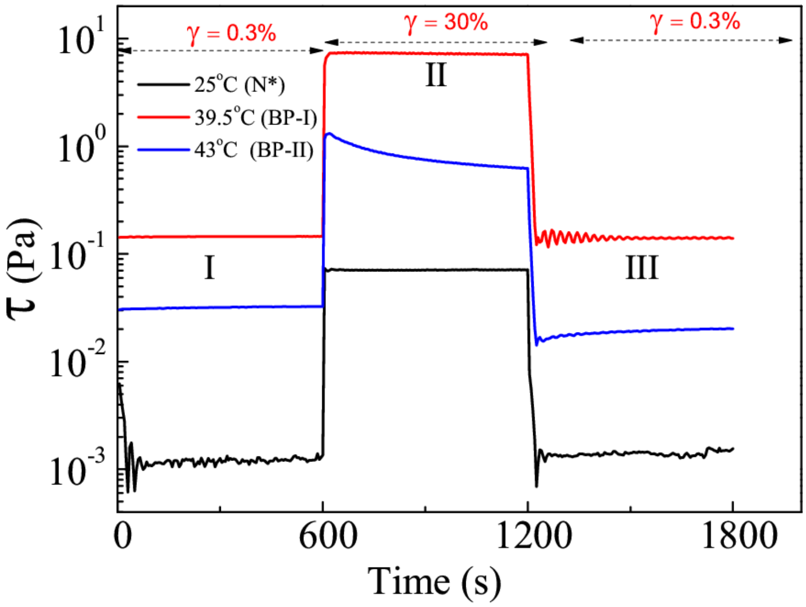

Figure 4.12: Time dependent shear stress at three different temperatures.

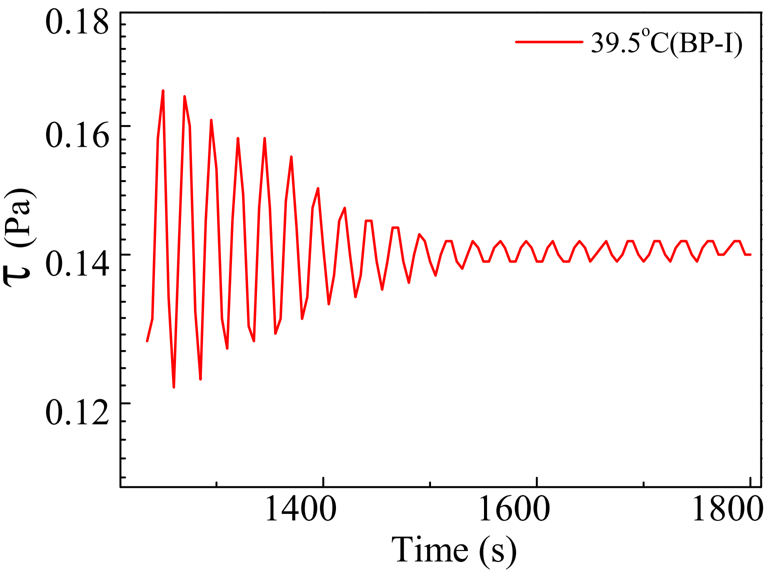

Figure 4.13: The periodic modulation in the BP-I, in region-III of Fig. 4.12.

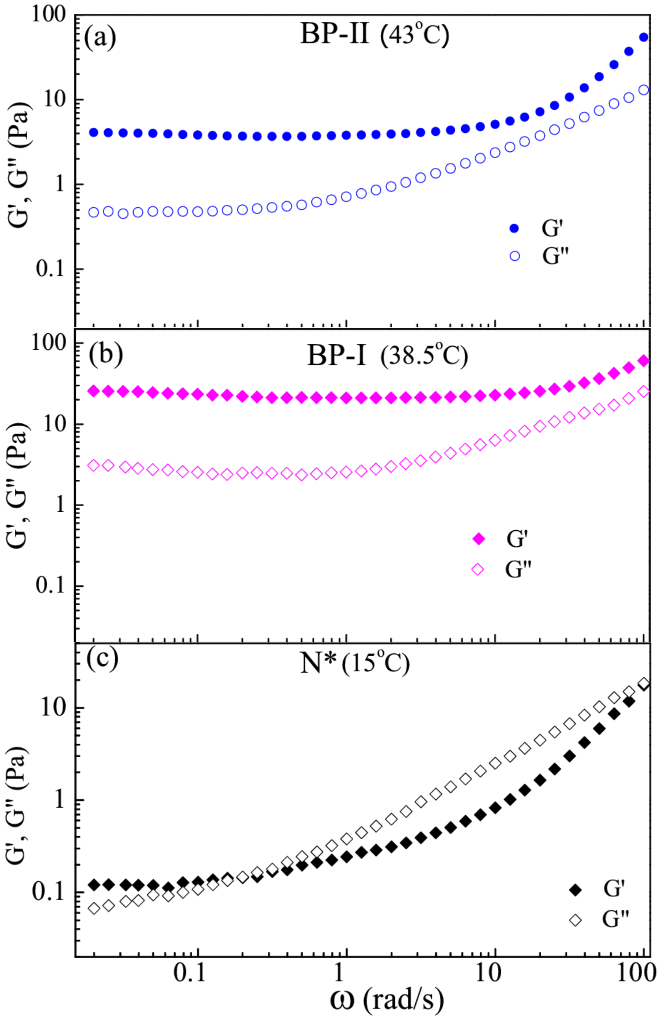

Figure 4.14: The frequency dependence of the storage (G') and the loss (G'') moduli of the sample at three different temperatures at a constant strain amplitude $\gamma = 1\%$.

region-III of Fig. 4.12, is shown separately in the Fig. 4.13. Under a large strain the defects of BP-I are displaced from the equilibrium positions consequently the network is distorted and they tend to reorganize upon removal of the strain and this could lead to a periodic stress oscillation that decays with time. The small oscillation in region-III in BP-II could be due to the reconnection of some defects. We conjecture that the step strain experiment displays the different dynamical responses of BP-I and BP-II under large strain which are due to the different network structure of the defects.

Finally we have measured the frequency response of G' and G'' of three phases (Fig.

4.14) at a constant strain amplitude $\gamma = 1\%$. The cholesteric phase exhibits a behavior very similar to that of a gel [20]. At low frequency ($\omega < 0.2$), $G^{'}$ reaches a plateau where $G_o = 0.1$ Pa, and the elastic modulus is higher than the loss modulus. At higher frequency ($\omega \geq 0.2$), a fluid like behavior is observed with $G^{''}$ being greater than $G^{'}$. There is a crossover at a critical frequency $\omega = 0.2$ rad s^{-1}, from a solid-like regime where $G^{'} > G^{''}$ and a fluid-like regime where $G^{''} > G^{'}$. In the case of BP-II and BP-I, $G^{'}$ is always greater than $G^{''}$ and a plateau signifies a solid-like behavior of the two phases.

4.4 Conclusion

We experimentally studied the rheological properties of cubic blue phases. Our experiment reveals several flow regimes with characteristic microstructures within each blue phase. At a high shear-rate regime all the phases exhibit a flow aligned nematic state. The measured apparent viscosity is larger in BP-I than in BP-II. In the step strain measurements BP-I exhibits decaying stress oscillation with time which is connected to the different dynamical response of the defect networks under large strain. The amplitude of the sinusoidal oscillations of BP-I in the step-strain experiment is larger than that of BP-II. These results are qualitatively in agreement with recent simulation. The larger critical strain for yield transition in BP-II is due to the breaking of defect nodes. Both BP-II and BP-I exhibit a solid-like behavior while the cholesteric phase shows a gel-like behavior and the elastic modulus of BP-I is larger than that of BP-II.

References

[1] F. Reinitzer. *Monatsh. Chem.*, vol. 9, no. 1, pp. 421–441, 1888.

[2] H. Kikuchi, M. Yokota, Y. Hisakado, H. Yang and T. Kajiyama. *Polymer-stabilized liquid crystal blue phases.* Nat. Mater., vol. 1, p. 64-68, 2002.

[3] H. J. Coles and M. N. Pivnenko. *Liquid crystal 'blue phases' with a wide temperature range.* Nature, vol. 436, no. 03932, pp. 997-1000, 1989.

[4] K. M. Chen, S. Gauza, H. Q. Xianyu and S. T. Wu. *Submillisecond gray-level response time of a polymer-stabilized blue-phase liquid crystal.* J. Display Technol., vol. 6, no. 2, pp. 49-51, 2010.

[5] D. P. Resler, D. S. Hobbs, R. C. Sharp, L. J. Friedman and T. A. Dorschner. *High-efficiency liquid-crystal optical phased-array beam steering.* Opt. Lett., vol. 21, no. 9, pp. 689-691, 1996.

[6] Y. H. Lin, H. S. Chen, H. C. Lin, Y. S. Tsou, H. K. Hsu and W. Y. Li. *Polarizer-free and fast response microlens arrays using polymer-stabilized blue phase liquid crystals.* Appl. Phys. Lett., vol. 96, no. 11, p. 113505, 2010.

[7] J. Yan, Y. Li and S. T. Wu. *High-efficiency and fast-response tunable phase grating using a blue phase liquid crystal.* Opt. Lett., vol. 36, no. 8, pp. 1404-1406, 2011.

[8] M. Mori, T. Hatada, K. Ishikawa, T. Saishouji, O. Wada, J. Nakamura and N. Terashima. *Mechanism of color breakup in field-sequential-color projectors.* J. Soc. Inf. Disp., vol. 7, no. 4, pp. 257-259, 1999.

[9] J. Yan and S. T. Wu. *Polymer-stabilized blue phase liquid crystals.* Opt. Mater. Express, vol. 1, no. 8, pp. 1527-1535, 2011.

[10] Y. Li, Y. Chen, J. Sun, S. T. Wu, S. H. Liu, P. J. Hsieh, K. L. Cheng and J. W. Shiu. *Dielectric dispersion on the Kerr constant of blue phase liquid crystals.* Appl. Phys. Lett., vol. 99, no. 18, p. 181126, 2011.

[11] O. Henrich, K. Stratford, D. Marenduzzo, P. V. Coveney and M. E. Cates. *Confined cubic bluephases under shear.* J. Phys. Condens. Matter, vol. 24, p. 284127, 2012.

[12] O. Henrich, K. Stratford, P. V. Coveney M. E. Cates and D. Marenduzzo. *Rheology of cubic blue phases.* Soft Matter, vol. 9, pp. 10243-10256, 2013.

[13] A. Dupuis, D. Marenduzzo, E. Orlandini and J. M. Yeomans. *Rheology of cholesteric Blue Phases.* Phy. Rev. Lett., vol. 95, no. 9, p. 097801, 2005.

[14] R. N. Kleiman, D. J. Bishop, R. Pindak and P. Taborek. *Shear modulus and specific heat of the liquid-crystal blue Phases.* Phy. Rev. Lett., vol. 53, no. 22, pp. 2137-2140, 1984.

[15] N. A. Clark, S. T. Vohra and M. A. Handschy. *Elastic resonance of a liquid-Crystal Blue Phase.* Phy. Rev. Lett., vol. 52, no. 1, pp. 57-60, 1984.

[16] M. Rajeswari, J. Ananthaiah, R. Dabrowski, V. S. S. Sastry, S. Dhara and B. K. Sadashiva. *Rheological properties of a chiral liquid crystal exhibiting type-II character.* Mol. Cryst. Liq. Cryst., vol. 547, no. 1, pp. 1729-1735, 2011.

[17] O. Chojnowska, R. Dabrowski, J. Yan, Y. Chen and S. T. Wu. *Electro-optical properties of photochemically stable polymer-stabilized blue-phase material.* J. Appl. Phys., vol. 116, no. 21, p. 213505, 2014.

[18] E. K. Wheeler, P. Izu and G. G. Fuller. *Structure and rheology of wormlike micelles.* Rheol. Acta, vol. 35, no. 2, pp. 139-149, 1996.

[19] B. Belzung, F. Lequeux, J. Vermant and J. Mewis. *Flow-Induced Anisotropy in Mixtures of Associative Polymers and Latex Particles.* J. Colloid Interface Sci., vol. 224, pp. 179-187, 2000.

[20] L. Ramos, M. Zapotocky, T. C. Lubensky and D. A.Weitz. *Rheology of defect networks in cholesteric liquid crystals*. Phys. Rev. E, vol. 66, p. 031711 , 2002.

5

Magnetodielectric and magnetoviscosity response of a ferromagnetic liquid crystal at low magnetic fields

5.1 Introduction

Ferrofluids are liquids prepared by suspending nanometer sized ferromagnetic particles in isotropic carrier fluids. The magnetic attraction of nanoparticles is weak enough that the entropic forces of the particles, steric and electrostatic repulsion due to the surfactant prevents magnetic clumping or agglomeration. The magnetic moments of the nanomagnets are aligned along the direction of the external magnetic field resulting in chain formation due to the dipole-dipole interaction. As a result, the viscosity of the ferrofluids increases significantly and these materials are useful for various magnetorheological applications [1–3].

Nematic liquid crystals exhibit anisotropic physical properties. The colloidal dispersion of nanoparticles (with low concentration) in liquid crystals does not affect the overall molecular orientation. Nevertheless, the small particles affect significantly the anisotropic physical properties that depend on the size, shape, concentration, and properties of the nanoparticles [4–15]. The colloidal dispersion of nanoparticles in liquid crystals combines the physical properties of nanoparticles and the orientational order of liquid crystals. Long ago, Brochard and de Gennes theoretically predicted various interesting properties of anisotropic ferrofluids, which can be prepared by dispersing different types of ferromagnetic nanoparticles in nematic liquid crystals (NLCs). They provided a continuum theory of magnetic suspensions in NLCs and so contrived the term as ferronematics [16]. In spite of several attempts in the past, only very recently the successful experimental realization of a ferromagnetic liquid crystalline material was reported by Mertelj *et al.* [17].

They prepared colloidal suspension of platelet type ferromagnetic nanoparticles in pentyl cyanobiphenyl (5CB) liquid crystal at room temperature. Subsequently, they studied on magneto-optic and converse magnetoelectric effects in these materials and described the system by a simple macroscopic theory [18]. There are a few studies on the physical measurements of liquid crystal nanocomposites based on ferromagnetic nanoparticles. Most of the experimental results showed that the nanocomposites are paramagnetic [15, 19]. This recent discovery of unambiguous ferromagnetic liquid crystals has created immense interest in the scientific community. A suspension of ferromagnetic nanoplatelets in a NLC can be macroscopically described by coupled $\overrightarrow{M}$ and $\hat{n}$, where $\overrightarrow{M}$ describes the density of magnetic moments. The coupling is a result of the interaction of the NLC with the surface of the nanoplatelets. $\overrightarrow{M}$ directly responds to magnetic and $\hat{n}$ to electric fields. However, due to their coupling, $\overrightarrow{M}$ also indirectly responds to electric field and inversely $\hat{n}$ to small magnetic fields. In this chapter, we study magnetodielectric and magnetoviscosity response of ferromagnetic LCs and in addition we also measured the splay elastic constant (K_{11}) and rotational viscosity (γ_1).

5.2 Experimental

We used 4-cyano-4$'$-octylbiphenyl (8CB) liquid crystal obtained from Sigma-Aldrich. It exhibits the following phase transitions: I 38.8°C N 32.5°C SmA 21.5°C Cr. We prepared isotropic suspension of scandium-doped barium hexaferrite single-crystal ($BaFe_{11.5}Sc_{0.5}O_{19}$) magnetic nanoplatelets in isopropanol. The nanoplatelets are chemically treated with a surfactant dodecylbenzenesulfonic acid, for homeotropic anchoring of the nematic director at its surface. The thickness of the platelets is about 5 nm, the distribution of the platelet diameter is approximately 70 nm, and the standard deviation is 38 nm [20]. The TEM image of the nanoplatelets is shown in Fig. 5.1(a). We prepared ferronematic samples by adding appropriate amount of suspension in 8CB liquid crystal. For example, 60 μl and 30 μl suspensions were added in each 100 μl of pure 8CB to get ferronematics with 0.6 wt% and 0.3 wt% of nanoplatelets respectively. The image shows that there is a large poly dispersity of the particles in the suspension. It was mixed in the isotropic phase (45°C) of the 8CB liquid crystal and stirred with a glass rod. In addition, we sonicated it for 30 minutes and kept in the oven for 12-14 hours (at 60°C) for the evaporation of isopropanol from the mixture. Then we quenched the sample into the nematic phase by immediately putting the sample with glass container in the water at room temperature (Fig. 5.2).

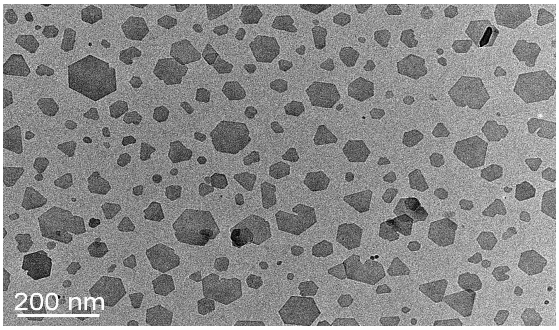

Figure 5.1: (a) TEM image of the magnetic nanoplatelets.

Figure 5.2: Preparation of ferromagnetic nematic suspension.

5.3 Results and discussion

5.3.1 Sample and texture observation

The physical appearance of the suspensions in the nematic phase with different weight percentage (0, 0.3 and 0.6 wt%) of nanoplatelets is shown in Fig. 5.3. The sample appears reddish with increasing concentration of the nanoplatelets.

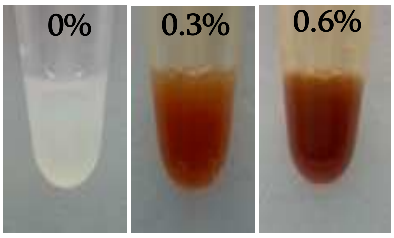

Figure 5.3: Magnetic nanoplatelets suspended in 8CB liquid crystal at three different concentrations: 0 wt.%, 0.3 wt.%, and 0.6 wt.% at 35°C.

We performed the preliminary texture observations of the ferromagnetic suspension in the nematic phase by filling the sample in a planar cell under optical polarising microscope (OPM) (Fig. 5.4(a) and 5.4(b)). It shows, the director is aligned uniformly along the rubbing direction with no evidence of large agglomeration of the platelets.

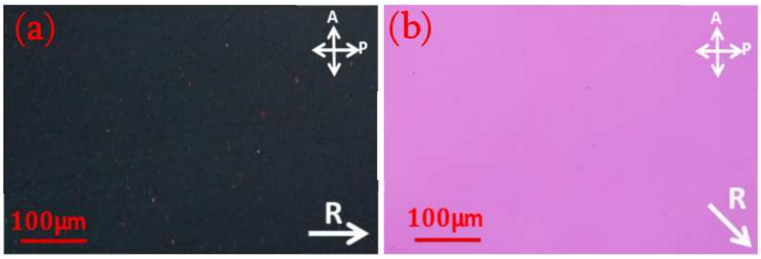

Figure 5.4: Photomicrographs of aligned cell of a ferromagnetic suspension (0.6 wt.% magnetic nanoplatelets) in the nematic phase under optical polarized microscope, polariser (P) and analyser (A) are crossed. (a) The rubbing direction (R) is parallel to P (b) the rubbing direction is at 45° with respect to P and A. Photomicrographs are taken in the absence of magnetic field.

All the observations are made under crossed polarisers. In Fig. 5.4(a) the rubbing direction (R) is parallel to the polariser and in Fig. 5.4(b) the rubbing direction is at

45° with respect to polariser (P) and analyser (A). Fig. 5.5(a) and 5.5(b) show the difference between, without and with the application of magnetic field respectively. Here the applied magnetic field is perpendicular to the nematic director. With the application of magnetic field, the magnetic domains are observed (Fig. 5.5(b)). The size of these domains increase up to few hundred micrometers.

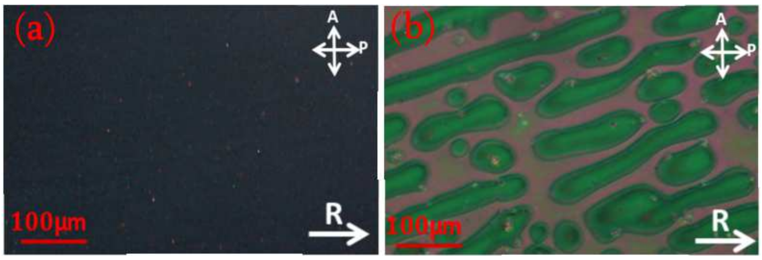

Figure 5.5: Photomicrographs of aligned cell of a ferromagnetic suspension (0.6 wt.% magnetic nanoplatelets) under optical polarized microscope (a) without magnetic field (b) with magnetic field. The green regions indicate the magnetic domains.

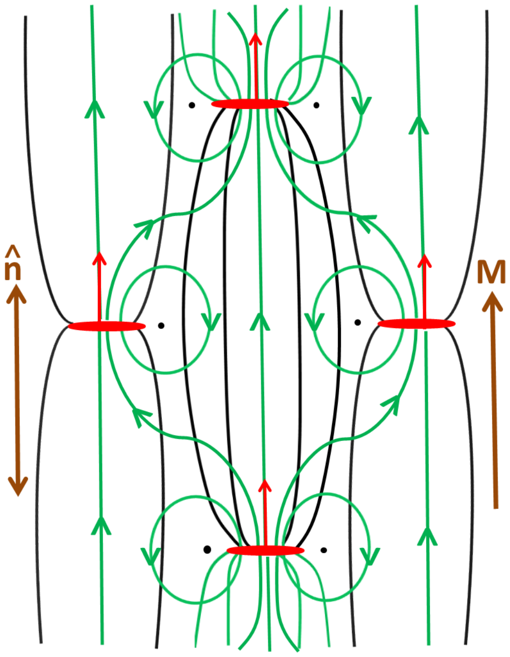

Figure 5.6: A schematic presentation of the director, $\hat{n}$ (black) and the magnetic field (green) around the platelets (red and vertical short-lines). Black dots represent cross-section of disinclination lines. Model adapted from Ref. [17]

A schematic representation of the magnetic nanoplatelets together with the LC director and cross-section of disclination lines is also shown in Fig. 5.6. The direction of magnetization is perpendicular to the plane of the nanoplatelets. The LC director is anchored perpendicular to the nanoplatelets surface and forms a stable suspension with a macroscopic magnetization along the director [17]. The stable suspension is possible due to the competition between the nematic mediated elastic force and the magnetic interaction between the nanoplatelets. The pairs of nanoplatelets in the nematic phase interact as quadrupoles. The quadrupolar interaction between the particles is maximum, when the line joining between the particles makes an angle 50° with respect to the nematic director. At this angle, the magnetic dipole interaction is very small, which leads to a parallel orientation of the particles. This prevents the agglomeration and gives a stable suspension.

5.3.2 Measurement of splay elastic constant (K_{11}) and rotational viscosity (γ_1)

First we discuss some physical properties measured in the absence of magnetic field. Figure 5.7 shows the temperature dependence of parallel ($\epsilon_{\|}$) and perpendicular ($\epsilon_{\perp}$)

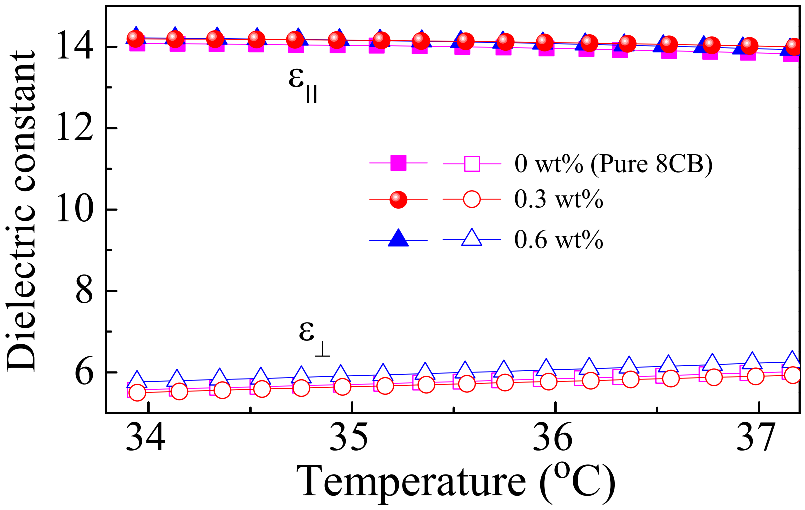

Figure 5.7: Temperature variation of parallel ($\epsilon_{\|}$) and ($\epsilon_{\perp}$) perpendicular components of dielectric constant.

components of dielectric constant. It is observed that the dielectric anisotropy $\Delta\epsilon$ ($= \epsilon_{\|}$ - $\epsilon_{\perp}$) remains unaffected by the incorporation of nanoparticles. For example, in all the samples including the pristine one, $\Delta\epsilon \simeq 8$.

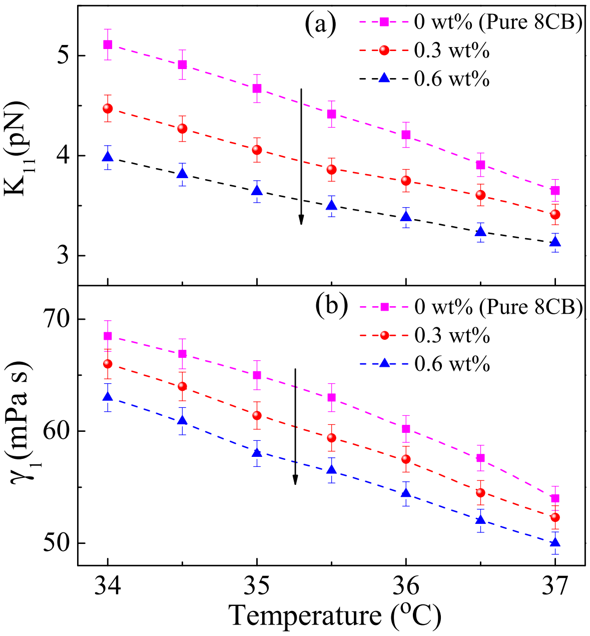

Figure 5.8: (a) Splay elastic constant (K_{11}), and (b) rotational viscosity (γ_1) in the nematic phase of the sample. Vertically downward arrows indicate the decrease of respective properties with increasing concentration of magnetic nanoparticles. Cell thickness 13.1 μm.

The temperature dependence of splay elastic constant (K_{11}) is shown in Fig. 5.8(a). We measured the splay elastic constant by using phase modulation technique (The details are discussed in chapter-2). It is measured directly from the Freedericksz threshold voltage [21], i.e., $V_{th} = \pi\sqrt{K_{11}/\epsilon_\circ\Delta\epsilon}$. It is observed that K_{11} decreases with increasing concentration of magnetic nanoplatelets. For example, at a particular temperature (35°C), K_{11} in the suspension (with 0.6 wt.% magnetic nanoplatelets) decreases by 22% compared to the pristine LC. We also measured the rotational viscosity (γ_1) from the measurement of relaxation time ($\tau_\circ$) in a planar cell using a phase-decay-time measurement technique. The details of this technique are discussed in chapter-2. The temperature variation of γ_1 is shown in Fig. 5.8(b). It is observed that γ_1 decreases with increasing concentration of magnetic nanoplatelets. For example, at 35°C, γ_1 (0.6 wt.% nanoplatelets) is reduced by 11% compared to the pure nematic LC. In the mean field theory [21,22], both $K_{11} \propto S^2$ and $\gamma_1 \propto S^2$. The decrease of S in the suspensions (0.6 wt.% magnetic nanoplatelets), according to dielectric anisotropy measurement is less than 4%. Hence, the decrease of K_{11} and γ_1 cannot be due to the decrease of S alone as both decrease more than that expected from the decrease of S.

5.3.3 Magnetodielectric measurements

To study the magnetodielectric effect, we filled the sample in a planar cell and the magnetic field is applied perpendicular to the director ($\hat{n}$), i.e., $\overrightarrow{B} \perp \hat{n}$. Fig. 5.9(a) shows the variation of effective dielectric constant (ϵ_{eff}) with magnetic field in pure 8CB in the nematic phase. It is observed that ϵ_{eff} increases rapidly beyond the Freedericksz threshold magnetic field ($\simeq$ 128 mT) (Fig. 5.9(a)) and tends to saturate at higher field as expected. The magnetic field dependence of ϵ_{eff} in the suspensions is significantly different. We filled the sample in the planar cells (thickness 60 μm) in the absence of external magnetic field, so initially they were magnetically polydomain state. During the first measurement (Fig. 5.9(b)), we observed that ϵ_{eff} increases slightly with magnetic field up to 4mT, and beyond this field it increases steeply. Finally, it saturates above a magnetic field of 10 mT. The saturation in ϵ_{eff} is a signature of a magnetically monodomain state. In the decreasing field, it shows hysteresis in the dielectric constant. It is due to the transformation from a polydomain to a monodomain state. However, due to the domain wall pinning at the surface imperfections, this transformation is not complete; as a result, we also observed the hysteresis in the successive measurements.

We performed the second measurement (Fig. 5.10), 20 min after the first one. During this time, the value of ϵ_{eff} (at 1 mT) is reduced from 10 (at 0.6 wt.% in Fig. 5.9(b)) to 8 (Fig. 5.10), which shows that the additional magnetic relaxation of the sample occurred (e.g., slow motion of domain walls). In the second measurement, ϵ_{eff} steeply increases with the external field as expected in a monodomain sample (Fig. 5.10). In the decreasing field, the curve is almost identical to the first measurement. The time lapse between two successive measuring points in both measurements was 30 s. The first measurement shows the growth of magnetic domains, which is governed by the motion of domain walls and during this measurement the sample is almost transformed from polydomain to a monodomain state. In pure 8CB, $\hat{n}$ is directly

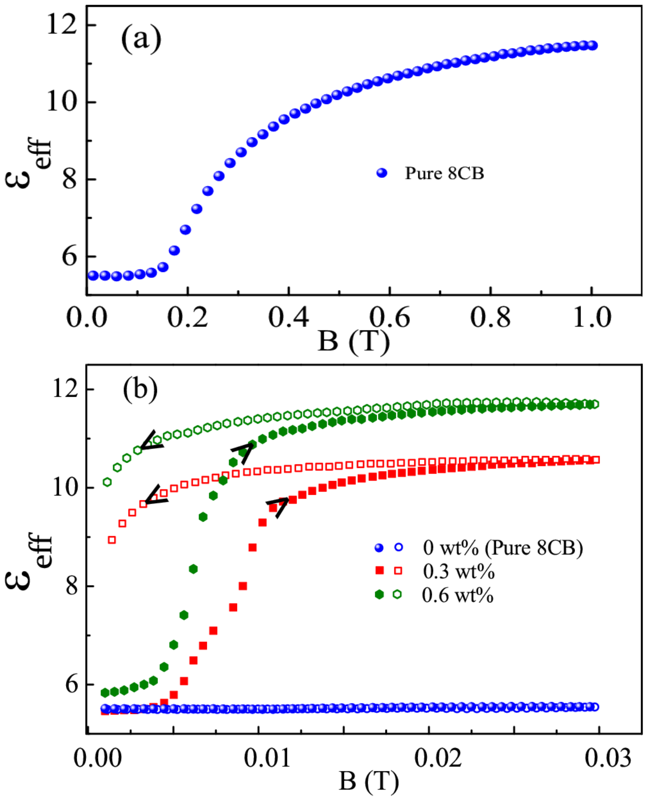

Figure 5.9: (a) Variation of effective dielectric constant (ϵ_{eff}) with magnetic field (B) of pure 8CB at 36°C. (b) Variation of ϵ_{eff} with magnetic field of a few samples with different concentrations: 0 wt.% (blue spheres), 0.3 wt.% (red squares), and 0.6 wt.% (green hexagons). Upward and downward arrows indicate the data collected during increasing and decreasing of the magnetic field. Cell thickness is d=58 μm. Applied voltage V=0.6 V and frequency f=3.111 kHz.

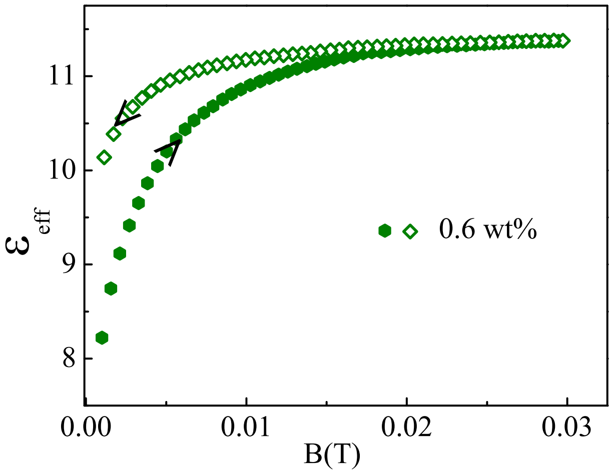

Figure 5.10: Variation of effective dielectric constant (ϵ_{eff}) with magnetic field (B) in the second measurement.

coupled to $\overrightarrow{B}$, whereas in the suspensions the coupling between $\hat{n}$ and $\overrightarrow{B}$ is indirect. The external magnetic field $\overrightarrow{B}$ directly induces reorientation of magnetization $\overrightarrow{M}$ and since $\overrightarrow{M}$ is coupled to the orientation of $\hat{n}$; $\overrightarrow{B}$ indirectly causes a reorientation of $\hat{n}$. The latter results in the increase of ϵ_{eff}. Here the reorientation of $\hat{n}$ is smaller than the reorientation of $\overrightarrow{M}$ and so the saturated value of ϵ_{eff} in the suspensions is smaller (Fig. 5.9(b)) than in the pure 8CB (where orientation of $\hat{n}$ is directly coupled with the external field) (Fig. 5.9(a)) [18] . Here we observed that the saturated value of ϵ_{eff} in the suspensions with higher concentration of platelets is larger (Fig. 5.9(b)). This is expected, since the saturated value depends on the coupling between $\overrightarrow{M}$ and $\hat{n}$, which is larger for higher density of the nanoplatelets.

5.3.4 Magnetoviscosity measurements

Magnetoviscosity measurements were made by using the magnetorheology setup. The details about this setup are discussed in chapter-2. The direction of the magnetic field is perpendicular to the plane of the plates. The variation of shear viscosity with magnetic field is shown in the Fig. 5.11. In pure 8CB, the shear viscosity (η_{eff}) at zero magnetic field is 25 mPa s and it is comparable to the Miesowicz viscosity η_2 of the nematic phase of the pure 8CB [23]. It suggests that the untreated plates of the rheometer induce almost planar alignment of the director along the shear direction (Fig. 5.11(a)). As the magnetic field is increased, the viscosity increases beyond 120 mT and reaches to about 40 mPa s at around 1 T. The measured viscosity in the decreasing field is lower than that measured during increasing magnetic field. This is because in the freshly loaded samples, usually there are many defects (disclination lines) and the sample is less homogeneous. In the ferromagnetic LC, the viscosity exhibits three distinct regimes. In the very low field region (below 10 mT), η_{eff} ($\simeq \eta_2$) is almost constant and increases rapidly in the intermediate field range (10 mT to 20 mT). At relatively higher field, η_{eff} saturates and exhibits hysteresis, while the field is reduced to zero (Fig. 5.11(b)).

In the suspension with 0.3 wt.% magnetic nanoparticles, at zero magnetic field, η_{eff} = 25 mPa s and it increases up to 62 mPa s in the saturation region and finally reduced

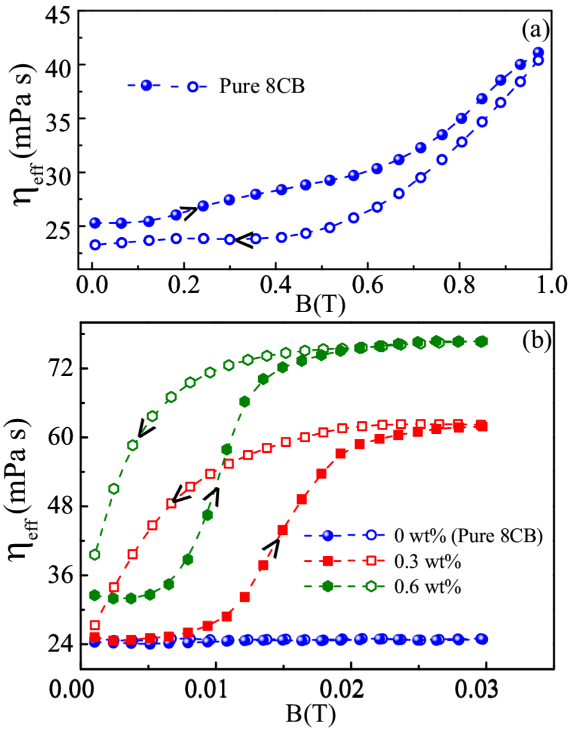

Figure 5.11: (a) Variation of shear viscosity (η_{eff}) with magnetic field of pure 8CB LC and (b) suspensions with different concentrations: 0 wt.% (blue spheres), 0.3 wt.% (red squares), and 0.6 wt.% (green hexagons) at shear-rate of 10 s^{-1}. Upward and downward arrows indicate the data collected during increasing and decreasing of the magnetic field. The measurements in the suspensions are restricted up to the field of 30 mT.

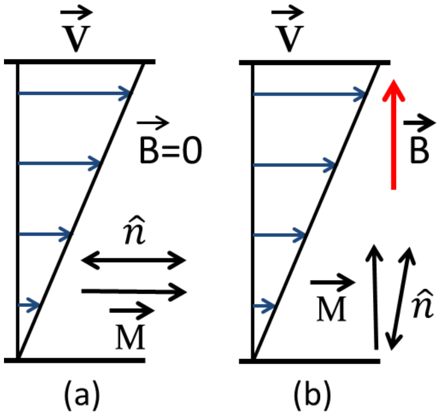

Figure 5.12: Orientation of director ($\hat{n}$) and magnetization ($\vec{M}$) at (a) zero and (b) finite field. The horizontal lines represent the direction and magnitude of shear velocity ($\vec{V}$).

to 27 mPa s at zero field. The viscosity at the zero field is equal to that of the pure 8CB sample and hence comparable to Miesowicz viscosity η_2. The effective viscosity in the saturated region is almost comparable to the Miesowicz viscosity η_1 of the pure 8CB at the same temperature [23]. This suggests that the director is almost parallel to the magnetic field (perpendicular to the shear direction) as schematically shown in Fig. 5.12(b). This technique helps us to measure two Miesowicz viscosities using a very small magnetic field. In the suspension with 0.6 wt.% magnetic nanoplatelets, the overall behavior is almost similar except that the values are larger and this is expected as the viscosity is linearly proportional to the phase volume of the nanoparticles.

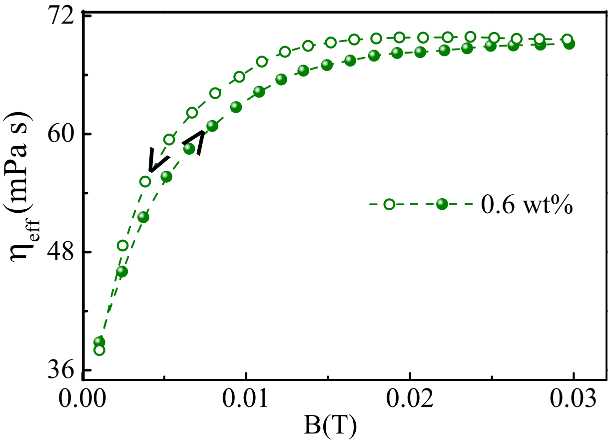

Figure 5.13: Variation of shear viscosity (η_{eff}) with magnetic field of 0.6 wt.% suspension in the second measurement.

We performed the second measurement (Fig. 5.13), 20 min after the first one. The field dependence of viscosity at the second measurement (Fig. 5.13) is significantly different from the first measurement (Fig. 5.11(b), at 0.6 wt.%) and somewhat similar to that is observed in the magnetodielectric measurements. We attributed this behavior to the growth of magnetic domains, resulting in the magnetically monodomain sample as mentioned previously. The second measurement shows the behavior of a monodomain sample. In the second measurement at the smallest field (1 mT), the viscosity is larger than that of the first measurement (Fig. 5.11(b), at 0.6 wt.%), and further it steeply increases and saturates above $\simeq$ 15 mT (Fig. 5.13). In the magnetodielectric measurements, there is a competing orienting mechanism. The cell surfaces induce parallel orientation of the director, and the magnetic field induces perpendicular orientation of the same. On the other hand, in the rheological experiment, parallel orientation is induced by flow and this competes with the magnetic alignment (Figs. 5.12(a) and 5.12(b)).

5.4 Conclusion

We found that the splay elastic constant and rotational viscosity are reduced in the ferronematic LC. The low field magnetodielectric and magnetoviscosity responses remarkably differ in the suspension from the pure LC due to the orientational coupling between the director field and the magnetization. The low magnetic field effects in these ferronematic materials make them useful for multipurpose applications because these are useful for both display and non-display applications such as a smart fluid. The small amount of magnetic nanoparticles (e.g. 0.3 wt.%) do not change the Miesowicz viscosities but facilitate the measurement at a significantly low magnetic field.

References

[1] S. Odenbach and S. Thurm. *Magnetoviscous effects in ferrofluids.* Springer, Berlin, 2002.

[2] B. M. Berkovsky, V. F. Medvedev, and M. S. Krakov. *Magnetic Fluids:Engineering Applications.* Oxford University Press, Oxford, 1993.

[3] B. Berkovski and V. Bashtovoy. *Magnetic fluids and applications handbook.* Edited, Begell House, Wallingford, 1996.

[4] M. Rahman and W. Lee. *Scientific duo of carbon nanotubes and nematic liquid crystals.* J. Phys. D: Appl. Phys., vol. 42, no. 6, p. 063001, 2009.

[5] R. Basu and G. S. Iannacchione. *Orientational coupling enhancement in a carbon nanotube dispersed liquid crystal.* Phys. Rev. E, vol 81, no. 5, p. 051705, 2010.

[6] R. Basu and G. S. Iannacchione. *Evidence for directed self-assembly of quantum dots in a nematic liquid crystal.* Phys. Rev. E, vol. 80, no. 1, p. 010701(R), 2009.

[7] R. Manda, V. Dasari, P. Sathyanarayana, M. V. Rasna, P. Paik, and S. Dhara. *Possible enhancement of physical properties of nematic liquid crystals by doping of conducting polymer nanofibres.* Appl. Phys. Lett., vol. 103, p. 141910, 2013.

[8] M. V. Rasna, K. P. Zuhail, R. Manda, P. Paik, W. Haase, and S. Dhara. *Discontinuous anchoring transition and photothermal switching in composites of liquid crystals and conducting polymer nanofibers.* Phys. Rev. E, vol. 89, p. 052503, 2014.

[9] J. F. Blach, S. Saitzek, C. Legrand, L. Dupont, J. F. Henninot, and M. Warenghem. *$BaTiO_3$ ferroelectric nanoparticles dispersed in 5CB nematic liq-*

uid crystal: Synthesis and electro-optical characterization. J. Appl. Phys., vol. 107, p. 074102, 2010.

[10] M. Kaczmarek, O. Buchnev, and I. Nandhakumar. *Ferroelectric nanoparticles in low refractive index liquid crystals for strong electro-optic response.* Appl. Phys. Lett., vol. 92, p. 103307, 2008.

[11] Y. Reznikov, O. Buchnev, O. Tereshchenko, V. Reshetnyak, A. Glushchenko, and J. West. *Ferroelectric nematic suspension.* Appl. Phys. Lett., vol. 82, no. 12, pp. 1917-1919, 2003.

[12] L. Wang, W. He, X. Xiao, M. Wang, M. Wang, P. Yang, Z. Zhou, H. Yang, H. Yu, and Y. Lu. *Low voltage and hysteresis-free blue phase liquid crystal dispersed by ferroelectric nanoparticles.* J. Mater. Chem., vol. 22, no. 37, pp. 19629-19633, 2012.

[13] A. Glushchenko, C. I. Cheon, J. West, F. Li, E. Buyuktanir, Y. Reznikov, and A. Buchnev. *Ferroelectric particles in liquid crystals: recent frontiers.* Mol. Cryst. Liq. Cryst., vol. 453, no. 1, pp. 227-237, 2006.

[14] W. Jian, L. Yu, C. Yonglie, L. Zhaoxi, X. Ying, L. Ziyang, S. Longpei, and Z. Jianying. *Magnetic-field-induced Freedericksz transition of a nematic liquid crystal doped with diazophenyl.* J. Mater. Sci. Mater. Electron., vol. 12, no. 10, pp. 597-599, 2001.

[15] P. Kopcansky, I. Potocova, M. Koneracka, M. Timko, A. G. M. Jansen, J. Jadzyn, and G. Czechowski. *The anchoring of nematic molecules on magnetic particles in some types of ferronematics.* J. Magn. Magn. Mater., vol. 289, pp. 101-104, 2005.

[16] F. Brochard and P. G. de Gennes. *Theory of magnetic suspension in liquid crystals.* J. Phys. France (Paris), vol. 31, no. 7, pp. 691 - 708, 1970.

[17] A. Mertelj, D. Lisjak, M. Drofenik, and M. Copic. *Ferromagnetism in suspensions of magnetic platelets in liquid crystal.* Nature, vol. 504, no. 7479, pp. 237-241, 2013.

[18] A. Mertelj, N. Osterman, D. Lisjak, and M. Copic. *Magneto-optic and converse magnetoelectric effects in a ferromagnetic liquid crystal.* Soft matter, vol. 10, no. 45, pp. 9065-9072, 2014.

[19] N. Podoliak, O. Buchnev, O. Buluy, G. D'Alessandro, M. Kaczmarek, Y. Reznikov, and T. J. Sluckin. *Macroscopic optical effects in low concentration ferronematics.* Soft Matter, vol. 7, pp. 4742-4749, 2011.

[20] D. Lisjak and M. Drofenik. *Chemical substitution-an alternative strategy for controlling the particle size of Barium ferrite.* Cryst. Growth Des., vol. 12, no. 11, pp. 5174-5179, 2012.

[21] P. G. de Gennes. *The Physics of Liquid Crystals.* Clarendon Press, Oxford, 1974.

[22] W. H. de Jeu. *Physical properties of liquid crystalline materials.* Gordon and Breach Science Publishers, New York, 1980.

[23] A. G. Chmielewski. *Viscosity coefficients of some nematic liquid crystals.* Mol. Cryst. Liq. Cryst., vol. 132, no. 3-4, pp. 339-352, 1986.

6

Rheological studies on liquid-crystal-colloids prepared by dispersing microparticles with homeotropic surface anchoring

6.1 Introduction

In the previous chapter we have studied the magnetodielectric and magnetoviscosity properties of ferromagnetic nanoplatelets suspended in nematic liquid crystals. In this chapter we discuss the defect induced microstructures by spherical microspheres and their effect on the rheological properties.

The colloidal dispersion in isotropic liquids like water, oil etc have been studied since decades due to their wide range of applications. However, the study of dispersion of nano and micro particles in anisotropic liquids like lyotropic and thermotropic liquid crystals (LCs) have created an immense interest in last two decades [1–6]. These are known as LC-colloids. The details about the LC-colloids and the induced topological defects are discussed in chapter-1. There have been many interesting experimental studies reported on liquid-crystal-colloids. In most studies the attention has been paid on the topological defects induced by a variety of particles or the laser assisted self-assembly, manipulation of defects by optical tweezers [2–4,7,8]. However, a few studies have been made on the bulk and rheological properties of liquid-crystal-colloids. For example, Oswald *et al.* studied the rheology of a lyotropic lamellar phase, where they showed under shear-flow how the dislocation loops cross and connect the layers and disturb the flow [9]. Meeker *et al.* have found an unusual soft-solid state in 5CB (pentyl cyanobiphenyl) liquid-crystal-colloids prepared by dispersing PMMA (polymethylmethacrylate) nanoparticles (250 nm) [10]. Petrov *et al.* showed that solid cellular structures are formed in these systems [11]. Anderson *et al.* have studied the details of the morphology of the cellular microstructures [12]. Subsequently they studied the mechanical properties of the nematic matrix with the cellular morphology [13]. The origin of cellular structure was studied and discussed by Vollmer *et al.* [14, 15]. Raghunathan *et al.* studied the elastic properties (splay and bend) of lyotropic liquid-crystal-colloids and found no substantial change in the elastic constant in the low particle concentrations ($< 2\%$) [16]. Poulin *et al.* have studied the phase separation and morphology of lyotropic colloidal systems made of small particles (60 to 120 nm latex polyballs) [17]. Zapotocky *et al.* investigated the effect of bigger silica particles (about 1 μm) in cholesteric LCs. From the rheological studies they showed the effect of network of disclinations connecting the bigger clusters of particles [18]. Wood *et al.* dispersed nearly a micron sized particles in 5CB and showed that the elasticity of the LC-colloids increases beyond a certain concentration. They showed it was due to the formation of percolating network structure of disclination lines. These lines are entangled with the particles giving a self-quenched defect glass state of line defects [19]. Bandyopadhyay *et al.* studied the rheology of LC-aerosil (7 nm) composites of SmA liquid crystal (8CB) and reported a soft glassy behavior of the composites with increasing particle density [20]. In all the above experiments, topological defects induced by the particles play a crucial role and these defects were induced mostly due to the spontaneous anchoring of the molecules on the particle's surface.

In this chapter we study the rheological properties of LC-colloids prepared by dispersing silica microparticles in 8CB LC. The particles are treated for homeotropic alignment of the LC molecules at the surface that usually induce hyperbolic hedgehog, Saturn ring or escaped defects (bubble-gum defects) depending on the surface anchoring and confinement. We performed rheomicroscopy studies that reveal shear dependent microstructural change of the nematic-colloid that gives shear thickening. Our study suggests that with increasing volume fraction, the SmA-colloids tend to emerge from soft-glass to shear induced ordered state of colloids.

6.2 Experimental

In the experiment we used monodisperse silica microspheres (average diameter 5 μm), coated with octadecyldimethyl[3-(trimethoxysilyl)propyl]ammonium chloride (DMOAP) to obtain perpendicular (homeotropic) alignment of LC molecules on the surface. Relatively larger size of the particle was chosen (than previously reported) for the purpose of simultaneous optical rheomicroscopy studies. The microspheres with different volume fractions (ϕ) namely 1 to 20% were dispersed in the nematic phase of 8CB liquid crystal by using a vortex mixture and ultrasonication. We used rheomicroscopy setup for all the rheological measurements. The details about this setup are discussed in chapter-2. A polarizer and an analyzer were kept crossed and placed in the microscope tube in appropriate places. The gap maintained between two parallel glass plates was 0.075 mm. We used 8CB LC which exhibits the following phase sequence: I 39.7°C N 32.4°C SmA. All the experiments were performed in cooling the sample from the nematic to SmA phase.

6.3 Results and discussion

First we observed the samples under polarizing optical microscope keeping it between two untreated glass plates. There was no appreciable change in the nematic-isotropic phase transition temperatures. It is also confirmed by differential scanning calorimetry (DSC) studies. Figure 6.1 shows the DSC measurements showing the temperature dependent heat flow on heating and cooling the sample at different volume fractions. We observed that there is no distinguishable change in the phase transition temperatures with increasing volume fractions.

Figure 6.2(a) shows the image of composite with volume fraction of particle 10% at room temperature (SmA phase) on the bottom plate of the rheometer. Figure 6.2(b) shows the image when it is heated above the nematic-SmA phase transition. We also

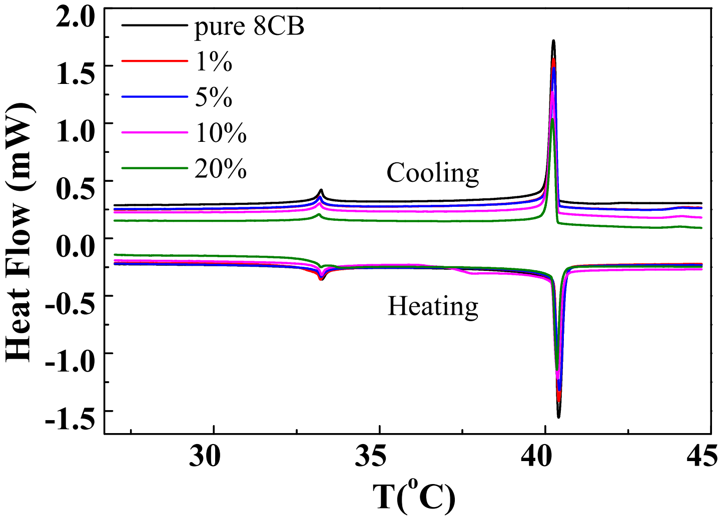

Figure 6.1: Temperature dependent heat flow on heating and cooling of the sample at different volume fractions.

observed that the sample in the nematic phase tend to flow while SmA behaves like a semi-solid.

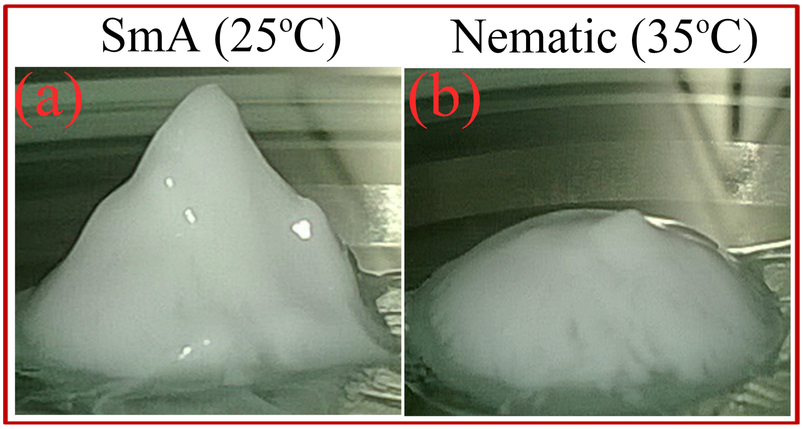

Figure 6.2: Physical appearance of the sample with $\phi = 10\%$ volume fraction of particles during mounting. (a) SmA phase (25°C) and (b) Nematic (35°C).

6.3.1 Nematic colloids

Figure 6.3 shows the texture observed under rheomicroscope after mounting (without shear). Most of the particles are agglomerated in smaller domains and only a few of them are dispersed individually. The isolated particles in Fig. 6.3 show four visible colored lobes of director distortion suggesting they have quadrupolar director configuration [19].

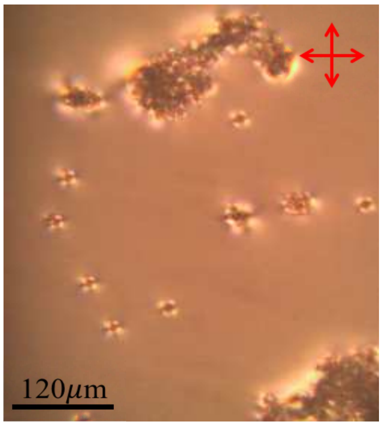

Figure 6.3: Rheomicroscopy image taken under crossed polarizers without shear for $\phi = 1\%$ in the nematic phase (35°C). Four bright lobes showing the director distortion due to the Saturn ring defects associated with the particles.

The sample was presheared at a low shear rate ($\dot{\gamma}$=10 s^{-1}) for 5 minutes before starting the measurements. Figure 6.4(a) shows the shear rate dependent shear stress at different concentrations of particles in the nematic phase (35°C). The apparent yield stress (σ_y) is increasing with increasing volume fraction of particles. Above shear rate 10 s^{-1}, the stress is proportional to the shear rate and this behavior is typical for nematics at high shear rate.

Figure 6.4(b) shows the variation of apparent yield stress (σ_y) as a function of volume fraction (ϕ). Up to $\phi = 5\%$, it shows a small but linear increase and beyond this σ_y changes slope and increases rapidly. For example, σ_y at $\phi = 20\%$ is approximately 200 times larger than that of the pure 8CB (Fig. 6.4(b)). The linear increase of stress is expected in dilute colloidal systems (Einstein's relation). The rapid increase in the σ_y suggests that there are some collective response of the particles.

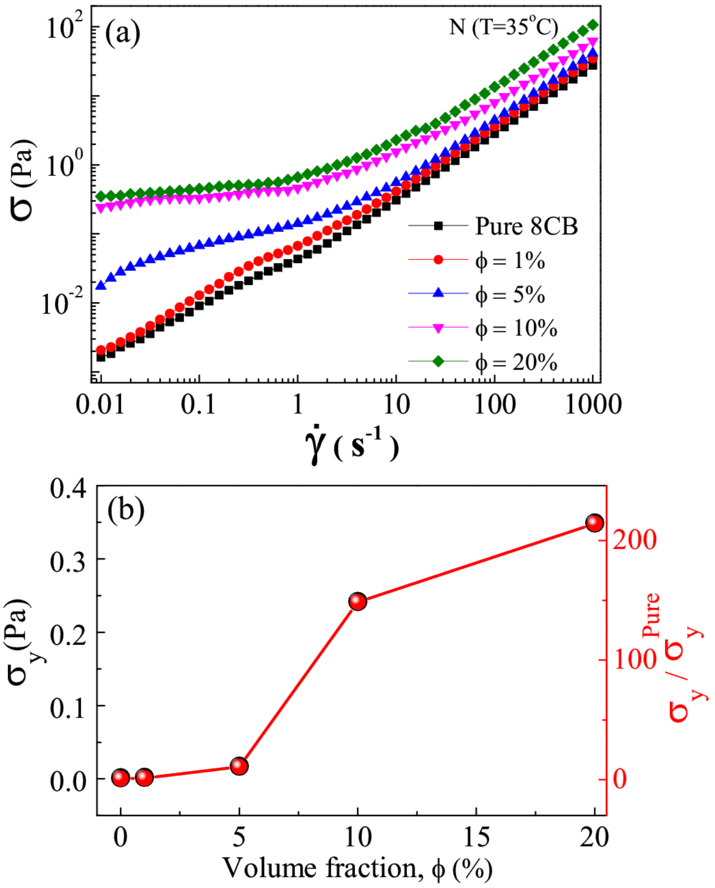

Figure 6.4: (a) Shear rate dependent shear stress (σ) and (b) yield stress (σ_y) at various volume fractions at a fixed temperature (T=35°C).

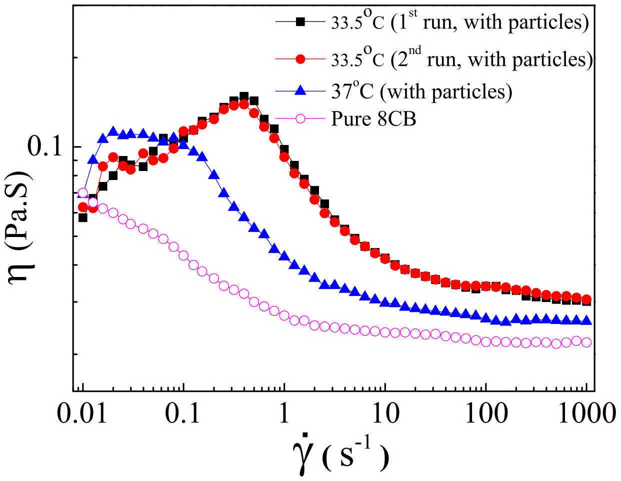

Figure 6.5: Variation of apparent viscosity η at a few temperatures at concentration $\phi = 1\%$.

To get more insight into the dilute systems, we looked at the textures in the rheomicroscope and measured the shear rate dependent viscosity at various temperatures. The sample was presheared at a high shear rate ($\dot{\gamma} = 500\ s^{-1}$) for 5 minutes to disperse the particles. Figure 6.5 shows the variation of apparent viscosity at $\phi = 1\%$ in the nematic phase at various temperatures. A clear shear thickening behavior is observed in the nematic phase (with particles) at all temperatures in the low shear rate range. This behavior is significantly different than the shear thinning behavior of nematic without particles (open circles in Fig. 6.5).

Figure 6.6 shows some representative images taken at different shear rates at temperature 33.5°C for ϕ=1%. With increasing shear rate, different microstructures of the particles are observed. In the low shear rate range (0.01 - 0.4 s^{-1}), the colloidal chains are bridged to form a network structure. The increase of the yield stress (Fig. 6.4(b)) with volume fraction of particles is due these network structure. In the shear thickening region the network is stretched, accompanied by deformation of the bridging chains. Increasing the shear rate increases the stress on the network structures and once the critical force is exceeded (about $\dot{\gamma}$=0.6 s^{-1}) they begin to break into smaller chains showing a shear thinning behavior. The shear thinning continues as long as the breaking process continues. At higher shear rate ($\dot{\gamma} = 39.8\ s^{-1}$) the chains start to break and forms relatively shorter chains. This shear thickening mechanism is somewhat similar to those reported in micelle forming associating polymers in water [21].

At much higher shear rate $\dot{\gamma} = 100\ s^{-1}$ many chains tend to align normal to the shear direction. At the same time many long disinclination lines are appeared (Fig. 6.6 $\dot{\gamma} =$ 100-150 s^{-1}). These line defects could be similar to those observed in micro-channels by Sengupta *et al.* [22]. With increasing shear the nematic director is orientated more uniformly and the nearly perpendicular orientation of the chains is consistent with the quadrupolar defect structure. In particular, in aligned cells, the quadrupolar chains tend to align perpendicular to the nematic director. At very high shear rate (above $\dot{\gamma} =$ 200 s^{-1}) the short chains further break into individual particles which are connected by the disclination lines. This can be understood based on the competing effect of shear energy and elastic interaction energy of the particles. The approximate shear energy of a particle can be written as $E = 6\pi\eta\dot{\gamma}ha^2$, where η is the apparent viscosity,

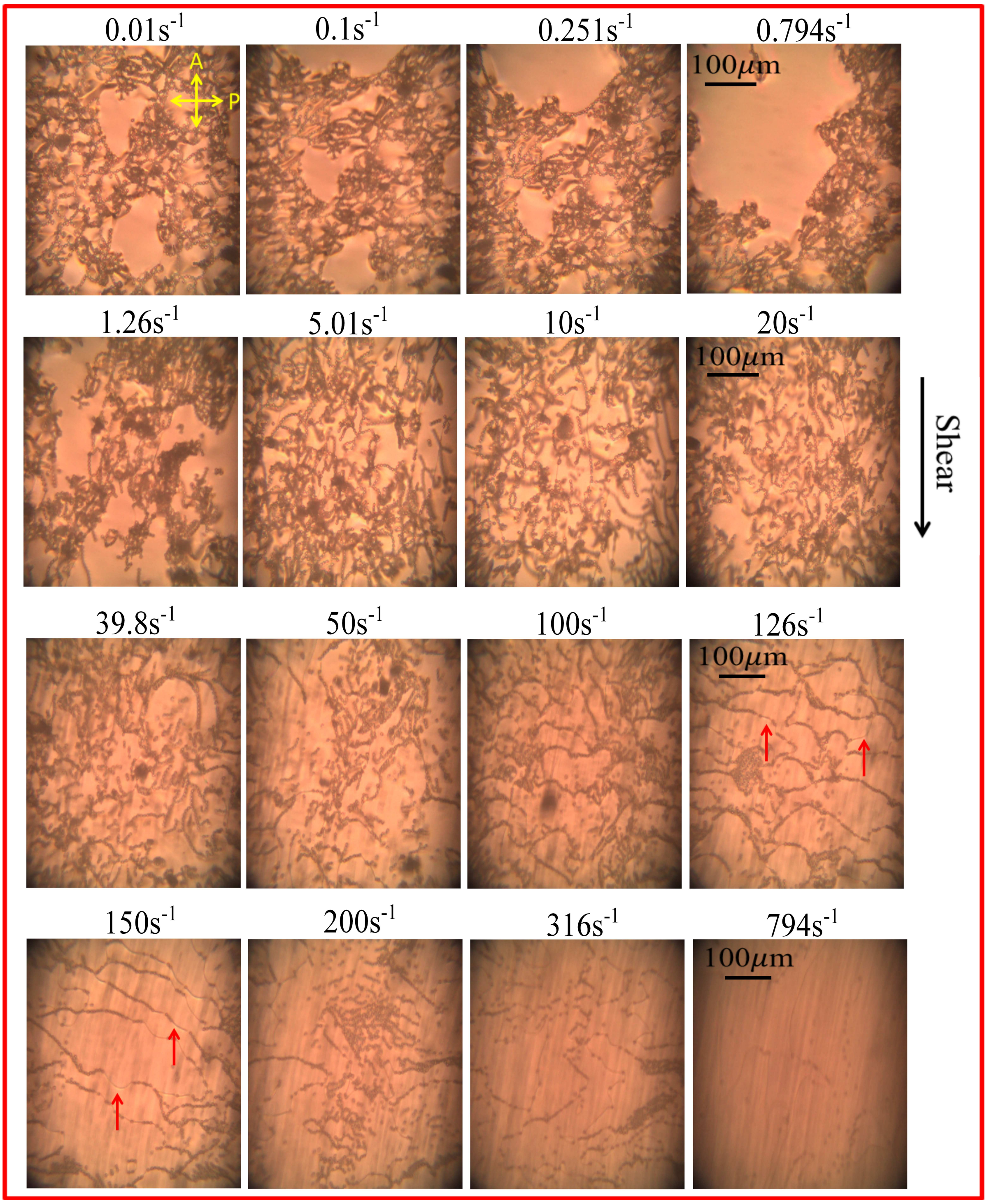

Figure 6.6: Representative rheomicroscopy images taken during the measurement of shear rate dependent shear viscosity in the nematic phase at 33.5°C for ϕ=1%. Red arrows indicate the disclination lines.

'h' is the gap between the plates and 'a' is the radius of the particles. The estimated shear energy at $\dot{\gamma}$ =20 s^{-1} is about 10 $^{6}k_BT$. Typical elastic interaction energy per particle is about a few thousand k_BT [4]. However this energy is expected to be a few orders of magnitude larger in the network (because a large number of particles are involved) and comparable to the shear energy. When the shear energy exceeds the elastic interaction energy, the breaking of chains into individual particles is expected.

6.3.2 SmA Colloids

Induced defects and colloidal interaction in SmA liquid crystals is not well understood so far. There are a few studies on the transformation of the topological defects across the nematic-SmA phase transition [7, 8, 23] in uniformly aligned cells. The induced disorder by the foreign particles in the SmA phase is expected to affect the mechanical properties. Hence we carried out rheological measurements in the SmA phase.

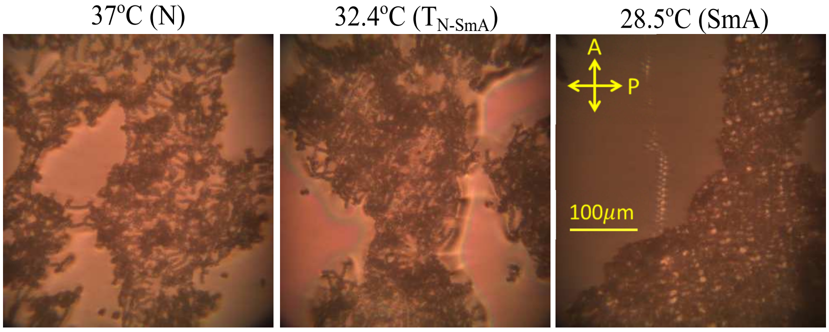

Figure 6.7: (a) Some representative rheomicroscopy images taken across the N-SmA phase transition (shear rate $\dot{\gamma}$ = 1 s^{-1}).

Figure 6.7 shows some representative rheomicroscopy images taken across the N-SmA phase transition. We observed that as the SmA phase is approached, the networks tend to get compressed and in the SmA phase the particles are collapsed creating focal conic texture. The regions without particles are well aligned (no focal conic texture). Unlike the nematic phase, no colloidal chains are observed in the SmA phase. Isolated colloidal particles with quadrupolar defect across the N-SmA phase transition has been studied by us in planar aligned cell [23]. The Saturn ring disappears at the transition and there is a boundary condition violation at the interface and clear layer structure around the particles cannot be directly deduced from the optical micrographs [23].

Figure 6.8 shows the variation of shear stress in the SmA phase (28°C) at various volume fractions. The apparent yield stress (σ_y) increases with increasing volume fraction of particles. For example, σ_y for pure SmA is about 0.33 Pa and it increases to 51 Pa at ϕ =20% hence this is about 150 times larger (Fig. 6.9).

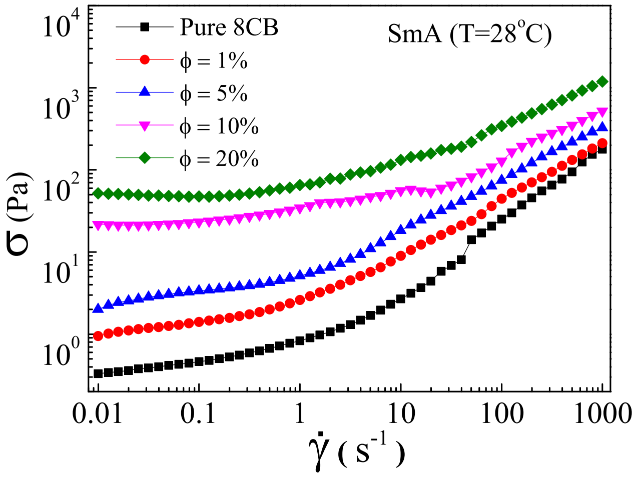

Figure 6.8: Shear rate dependent shear stress in the SmA phase (28°C) at various volume fractions (ϕ) of particles.

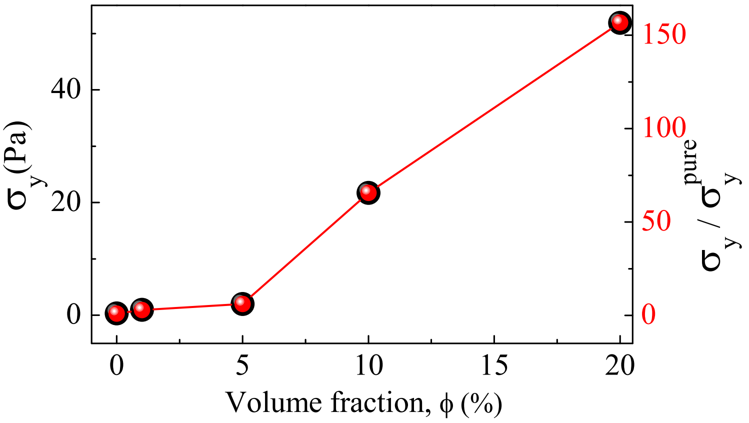

Figure 6.9: The apparent yield stress (σ_y) with ϕ obtained from Fig. 6.8.

Figure 6.10 shows the variation of storage (G') and loss (G'') moduli, as a function of applied strain γ at different volume fractions. Two important observations are made; (1) both the elastic moduli (G' and G'') increase and (2) the critical strain amplitude γ_c (crossover of G' and G'') decreases with increasing ϕ.

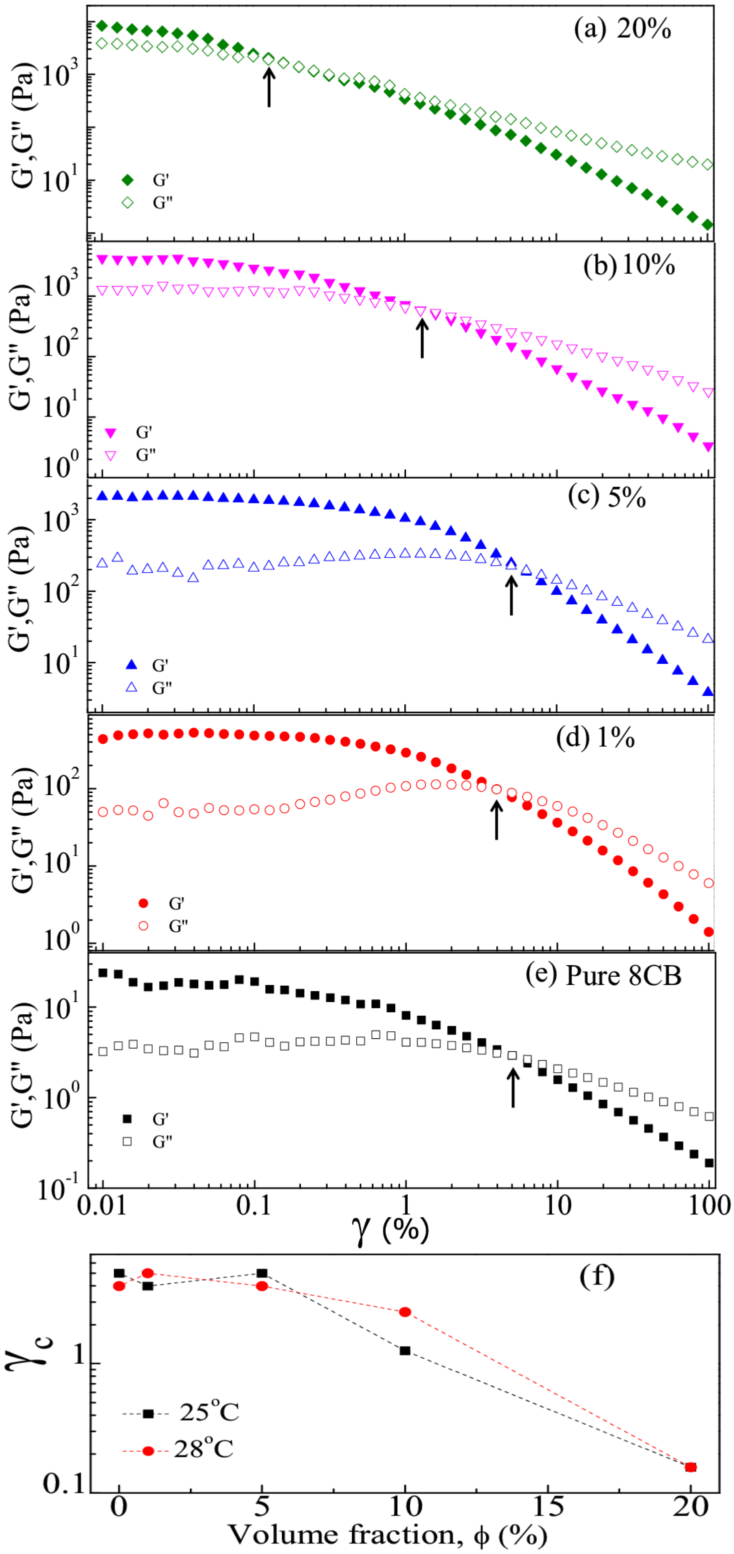

Figure 6.10: (a) to (e) Strain dependence of the storage G' and loss G'' moduli with increasing volume fraction of particle at constant angular frequency $\omega = 1$ rad/s at T=25°C. The arrows indicate the crossover. (f) The variation of critical strain amplitude, γ_c (the cross over of G' and G'') at different volume fractions.

For example, $G^{'}$ is 300 times larger in LC-composite with $\phi = 20\%$ compared to the pure 8CB. The variation of γ_c (strain induced yielding) with ϕ at two different temperatures is shown in Fig. 6.10(f). It is observed that γ_c is decreasing with increasing ϕ. For example, the value of γ_c for 0 to 10% is one order of magnitude larger than that of ϕ =20%. This behaviour can be explained based on the jammed domains of particles as seen in the rheomicroscopy (Fig. 6.7, SmA phase). With increasing ϕ, the number density and size of these jammed domains increase. As they are fragile, under low strain amplitude they can break and flow as a result the critical strain amplitude (γ_c) is expected to decrease [24].

It is known that the colloidal suspension can undergo glass transition with increasing particle concentration and can crystallize under favourable condition [24, 25]. To see this aspect we studied the frequency dependence of the storage ($G^{'}$) and loss ($G^{''}$) moduli. Figure 6.11 shows the angular frequency dependence of $G^{'}$ and $G^{''}$ at different volume fractions. The SmA phase (without colloids) shows typical frequency dependence i.e., both moduli are increasing with frequency. It is noted that for ϕ =1, 5 and 10%, $G^{''}(\omega)$ exhibits a shallow minimum. This is due to the increase in $G^{''}(\omega)$ at both lower and at higher frequencies. The low frequency rise is due to a very slow structural rearrangement of the particles suggesting there exists a relaxation process. The high frequency rise signifies the domination of viscous relaxation of fluid phase [26, 27]. This is also a typical characteristic of many colloidal soft glasses. Hence we analyze the results based on the soft glassy rheology model. In this model the real part of the storage modulus is given by [28, 29]:

$$G'(\omega) = G_\circ + \beta\omega^\alpha \tag{6.1}$$

where $G_\circ$, is the plateau modulus that arises due to the static defects in SmA and the frequency dependent term results from the bulk response of the materials. β arises from the disorientated (misaligned) parts of the sample [20, 28, 30].

The fit parameters are plotted with volume fraction in Fig. 6.12. It is observed that α decreases with increasing volume fraction and tends to zero ($\alpha \rightarrow 0$) upto ϕ = 10% (Fig. 6.12(a)). Similar behavior was also observed in many colloidal soft glass materials [20, 25]. The variation of the ratio $G^{''}/G^{'}$ with ϕ is also shown in

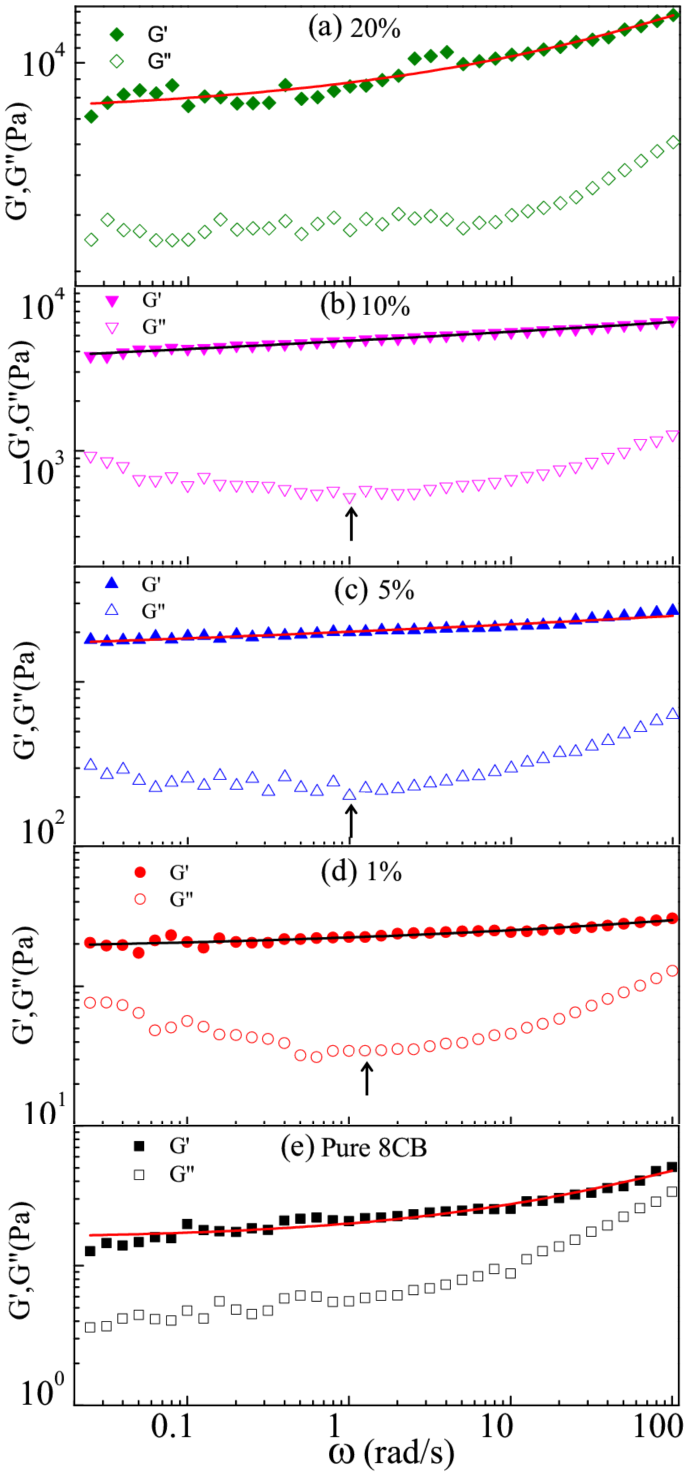

Figure 6.11: Angular frequency dependence of storage (G') and loss (G'') moduli at different volume fractions at constant strain amplitude 0.03% at T=25°C. Continuous lines are the best fit to equation (6.1). Vertical arrows indicate the minimum in G''.

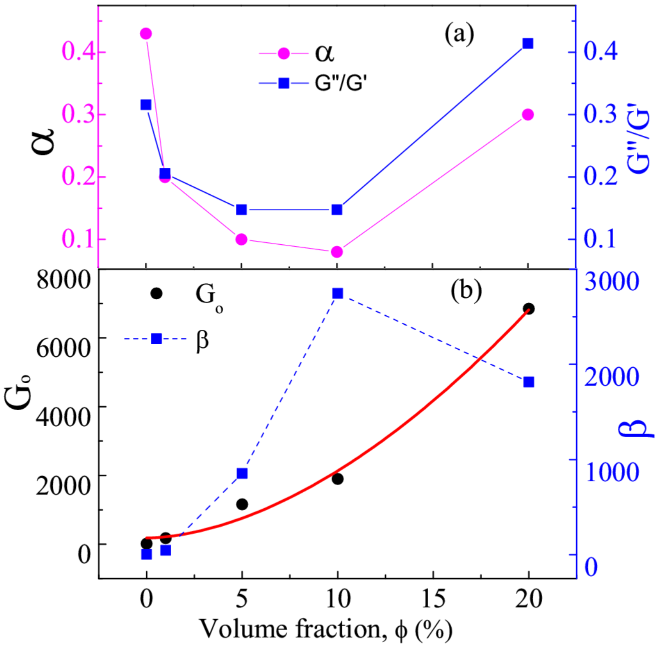

Figure 6.12: Variation of α characterizing the power-law contribution to $G^{'}(\omega)$ and the ratio of $G^{''}/G^{'}$ as a function of volume fraction of particles (ϕ). (b) Variation of fit parameters, $G_{\circ}$ and β obtained from the fitting of $G^{'}$ (ω) data with respect to ϕ . The red line is the best fit result $G_{\circ} \sim \phi^{1.8\pm0.2}$.

Fig. 6.12(a). We observed that $G^{''}/G^{'} \sim \alpha$ as expected in the soft glassy rheology model [20, 29, 31]. Fig. 6.12(b) shows the variation of $G_{\circ}$ and β with volume fraction. The increase of β with ϕ indicates that the contribution from the disoriented parts of the sample increases due to the inclusion of the particles. The increase of $G_{\circ}$ indicates that the smectic defects dominate this soft glassy rheology. Theoretically in analogy with rubber elasticity the elastic response of static defect-networks should vary as $G_{\circ} \sim \rho^{2}$, where ρ is the density of the particles [20, 28]. In our experiment we find that $G_{\circ} \sim \phi^{1.8\pm0.2}$ (Fig. 6.12(b)). Similar exponent was also reported in case of aerosil dispersed SmA liquid crystals (8CB) [20]. At higher concentrations (ϕ =20%), both α and the ratio $G^{''}/G^{'}$ tend to increase with ϕ. We conjecture that at this high volume fraction of particles under oscillation some short-range order among the particles is developed.

6.4 Conclusion

We studied the rheological properties of nematic and SmA LC-colloids prepared by dispersing spherical microparticles with homeotropic boundary condition in 8CB liquid crystals. The microparticles in the nematic phase create chains mediated by the induced defects with quadrupolar director configuration and form networks with increasing volume fraction. We observed a shear thickening behavior in the low shear rate range. The rheomicroscopy studies in the nematic phase reveal the shear-rate dependent distinct dynamics of the networks. The dynamic response of the SmA colloids shows a soft glassy rheology with increasing volume fraction up to a certain range. Finally, our study reveals that the rheological properties of nematic and SmA colloids are significantly contributed by the particle induced defects and their self-assembly.

References

[1] H. Stark. *Physics of colloidal dispersions in nematic liquid crystals*. Phys. Rep., vol. 351, no. 6, pp. 387-474, 2001.

[2] P. Poulin, H. Stark, T. C. Lubensky, and D. A. Weitz. *Novel colloidal interactions in anisotropic fluids*. Science, vol. 275, no. 5307, pp. 1770 - 1773, 1997.

[3] I. I. Smalyukh, O. D. Lavrentovich, A. N. Kuzmin, A. V. Kachynski, and P. N. Prasad. *Elasticity-mediated self-organization and colloidal interactions of solid spheres with tangential anchoring in a nematic liquid crystal*. Phys. Rev. Lett., vol. 95, p. 157801, 2005.

[4] I. Musevic, M. Skarabot, U. Tkalec, M. Ravnik, and S. Zumer. *Two-dimensional nematic colloidal crystals self-assembled by topological defects*. Science, vol. 313, no. 5789, pp. 954-958, 2006.

[5] F. Serra. *Curvature and defects in nematic liquid crystals*. Liq. Cryst., vol. 43, no. 13-15, pp. 1920-1936, 2016.

[6] I. R. Nemitz, K. M. Eleney, C. M. Crudden, R. P. Lemieux, R. G. Petschek and C. Rosenblatt. *Chiral periodic mesoporous organosilica in a smectic-A liquid crystal: source of the electrooptic response*. Liq. Cryst., vol. 43, no. 4, pp. 497-504, 2016.

[7] K. P. Zuhail, P. Sathyanarayana, D. Sec, S. Copar, M.Skarabot, I. Musevic, and S. Dhara. *Topological defect transformation and structural transition of two-dimensional colloidal crystals across the nematic to smectic-A phase transition*. Phys. Rev. E(R), vol. 91, no. 3, p. 030501, 2015.

[8] K. P. Zuhail and Surajit Dhara. *Temperature dependence of equilibrium separation and lattice parameters of nematic boojum-colloids*. Appl. Phys. Lett., vol. 106, p.

211901 (2015).

[9] P Oswald and M Allain. *Rheology an structural defects in a lyotropic lamellar phase.* J. Colloid Interface Sci., vol. 126, no. 1, pp. 45-53, 1988.

[10] S. P. meeker, W. C. K. Poon, J. Crain, and E. M. Terentjev. *Colloid–liquid-crystal composites: An unusual soft solid.* Phys. Rev. E(R), vol. 61, no. 6, pp. R6083-R6086, 2000.

[11] P. G. Petrov and E. M. Terentjev. *Formation of Cellular Solid in Liquid Crystal Colloids.* Langmuir, vol. 17, no. 10, pp. 2942-2949, 2001.

[12] V.J. Anderson, E.M. Terentjev, S.P. Meeker, J. Crain, and W.C.K. Poon. *Cellular solid behaviour of liquid crystal colloids 1. Phase separation and morphology.* Eur. Phys. J. E, vol. 4, pp. 11-20, 2001.

[13] V.J. Anderson and E.M. Terentjev. *Cellular solid behaviour of liquid crystal colloids 2. Mechanical properties.* Eur. Phys. J. E, vol. 4, no.1, pp. 21-28, 2001.

[14] D. Vollmer, G. Hinze, W.C.K. Poon, J. Cleaver, and M. E. Cates. *The origin of network formation in colloid–liquid crystal composites.* J. Phys.: Condens. Matter, vol. 16, pp. L227–L233, 2004.

[15] D. Vollmer, G. Hinze, B. Ullrich, W.C.K. Poon, M. E. Cates, and A. B. Schofield. *Formation of self-supporting reversible cellular networks in suspensions of colloids and liquid crystals.* Langmuir, vol. 21, pp. 4921-4930, 2005.

[16] V. A. Raghunathan, P. Richetti, and D. Roux. *Dispersion of latex particles in a nematic solution.* Langmuir, vol. 12, pp. 3789–3792, 1996.

[17] P. Poulin, V. A. Raghunathan, P. Richetti, and D. Roux. *On the dispersion of latex particles in a nematic solution. I. Experimental evidence and a simple model.* J. Phys. II France, vol. 4, pp. 1557-1569, 1994.

[18] M. Zapotocky, L. Ramos, P. Poulin, T. C. Lubensky, and D. A. Weitz. *Particle-stabilized defect gel in cholesteric liquid crystals.* Science, vol. 283, no. 5399, pp. 209-212, 1999.

[19] T. A. Wood, J. S. Lintuvuori, A. B. Schofield, D. Marenduzzo, and W. C. K. Poon. *A self-quenched defect glass in a colloid-nematic liquid crystal composite.* Science, vol. 334, no. 6052, pp. 79-83, 2011.

[20] R. Bandyopadhyay, D. Liang, R. H. Colby, J. L. Harden, and R.L. Leheny. *Enhanced Elasticity and Soft Glassy Rheology of a Smectic in a Random Porous Environment.* Phys Rev. Lett., vol. 94, p. 107801, 2005.

[21] A. Yekta, B. Xu, J. Duhamel, H. Adiwidjaja, and M. A. Winnik. *Fluorescence Studies of associating polymers in water: determination of the chain end aggregation number and a model for the association process.* Macromolecules, vol. 28, p. 956, 1995.

[22] A. Sengupta, U. Tkalec and C. Bahr. *Nematic textures in microfluidic environment.* Soft Matter, vol. 7, no. 14, pp. 6542-6549, 2011.

[23] K. P. Zuhail and S. Dhara. *Effect of temperature and electric field on 2D nematic colloidal crystals stabilised by vortex-like topological defects.* Soft Matter, vol. 12, pp. 6812-6816, 2016.

[24] N. Koumakis, A.B. Schofield, and G. Petekidis. *Effects of shear induced crystallization on the rheology and ageing of hard sphere glasses.* Soft Matter, vol.4, pp. 2008-2018, 2008.

[25] D. T. N. Chen, Q. Wen, P. A. Janmey, J. C. Crocker, and A. G. Yodh. *Rheology of Soft Materials.* Annu. Rev. Condens. Matter Phys., vol. 1, pp. 301-322, 2010.

[26] T. G. Mason and D. A. Weitz. *Linear viscoelasticity of colloidal hard sphere suspensions near the glass transition.* Phys. Rev. Lett., vol. 75, pp. 2770-2773, 1995.

[27] T. G. Mason, J. Bibette, and D. A. Weitz. *Elasticity of Compressed Emulsions.* Phys. Rev. Lett., vol. 75, pp. 2051-2054, 1995.

[28] L. Ramos, M. Zapotocky, T. C. Lubnesky, and D. A. Weitz. *Rheology of defect networks in cholesteric liquid crystals.* Phys. Rev. E, vol. 66, p. 031711, 2002.

[29] P.Sollich, F. Lequeux, P. Hébraud, and M. E. Cates. *Rheology of Soft Glassy Materials*. Phys. Rev. Lett., vol. 78, no. 10, pp. 2020-2023, 1997.

[30] R. Sahoo, J. A. Ananthaiah, R. Dabrowski, and S. Dhara. *Rheology of twist-grain-boundary-A liquid crystals*. Phys. Rev. E, vol. 90, p. 012506, 2014.

[31] G. G. Nair, S. Krishna Prasad, R. Bhargavi, V. Jayalakshmi, G. Shankar, and C.V. Yelamaggad. *Soft glass rheology in liquid crystalline gels formed by a monodisperse dipeptide*. J. Phys. Chem. B, vol. 114, no. 2, pp. 697-704, 2010.

Publications

Publications related to thesis

1. Rheological studies on liquid-crystal colloids prepared by dispersing spherical microparticles with homeotropic surface anchoring.
   Rasmita Sahoo and Surajit Dhara.
   Liquid Crystals, DOI: 10.1080/02678292.2017.1309469.

2. Experimental studies on the rheology of cubic blue phases.
   Rasmita Sahoo, O. Chojnowska, R. Dabrowski and Surajit Dhara.
   Soft Matter 12, 1324 (2016).

3. Magnetodielectric and magnetoviscosity response of a ferromagnetic liquid crystal at low magnetic fields.
   Rasmita Sahoo, M. V. Rasna, D. Lisjak, A. Mertelj and Surajit Dhara.
   Applied Physics Letters 106, 161905 (2015).

4. Rheology of twist-grain-boundary-A liquid crystals.
   Rasmita Sahoo, J. Ananthaiah, R. Dabrowski and Surajit Dhara.
   Physical Review E 90, 012506 (2014).

Other Publications

1. Unusual temperature dependence of elastic constants of an ambient-temperature discotic nematic liquid crystal.

D. Venkata Sai, G. Mirri, P. H. J. Kouwer, **R. Sahoo**, I. Musevic and S. Dhara. *Soft Matter* 12, 2960 (2016).

2. Effect of temperature on steady shear magnetorheology of CoNi microcluster-based MR fluids.
   I. Arief, **Rasmita Sahoo** and P.K. Mukhopadhyay.
   Journal of Magnetism and Magnetic Materials 412, 194 (2016).

3. Size dependence of magnetorheological properties of cobalt ferrite ferrofluid.
   B. Radhika, **Rasmita Sahoo** and S. Srinath.
   AIP Conference Proceedings 1665, 050167 (2015).

4. Synthesis and characterization of novel ABA-type azobenzene-containing tri-block copolymers from telechelic polystyrene.
   T. Rajasekhar, M. Trinadh, **Rasmita Sahoo**, S. Dhara and A. V. S. Sainath.
   Designed Monomers and Polymers 18, 145 (2015).

5. Rheology of nematic liquid crystals with highly polar molecules.
   J. Ananthaiah, **Rasmita Sahoo**, M. V. Rasna and S. Dhara.
   Physical Review E 89, 022510 (2014).

Conference attended

1. Attended 4th international soft matter conference (ISMC-2016) and presented a **poster** entitled “Rheological studies on Nematic and Smectic-A liquid crystal colloids” held in Grenoble, France.

2. Attended 23rd National conference on Liquid Crystals (NCLC-2016) and presented an **oral talk** entitled “Defect-induced microstructures by spherical microparticles and their effect on the rheological properties of 8CB liquid crystal” held in Dhanbad, India.

3. Attended International Complex Fluids conference (CompFlu-2016 (December)) and presented a **poster** entitled “Rheomicroscopy studies on liquid crystal colloids” held at Hyderabad, India.

4. Attended International Complex Fluids conference (CompFlu-2016 (January)) and presented an **oral talk** entitled “Rheology of TGB_A liquid crystal” held at IISER Pune, India.

5. Presented a poster entitled “Magnetodielectric and magnetoviscosity response of a ferromagnetic liquid crystal at low magnetic fields” at Frontier in Physics (FIP-2016) and got **Best Poster Award**.

6. Attended 3^{rd} Soft Matter Young Investigators Meet (SMYIM-2015) and presented a **poster** entitled “Magnetodielectric and magnetoviscosity response of a ferromagnetic liquid crystal at low magnetic fields” held in Pondichery, India.

7. Attended 20th National conference on Liquid Crystals (NCLC-2013) and presented a poster entitled “Structural defect mediated viscoelasticity of liquid crystalline state analogues of Abrikosov phase” held in Manipal, India and got **Best Poster Award**.

8. Attended Frontiers in Physics (FIP), conducted by School of Physics, University of Hyderabad, India and presented poster entitled “Rheology of twist grain boundary-A liquid crystal” at Frontier in Physics (FIP-2014) and got **Best Poster Award** Award.

9. Attended workshop on *Soft Matter Self-Assembly and Dynamics*, University of Hyderabad, India, 2014.

10. Workshop on *Machine Drawing and Machining* , University of Hyderabad, India, 2012.